



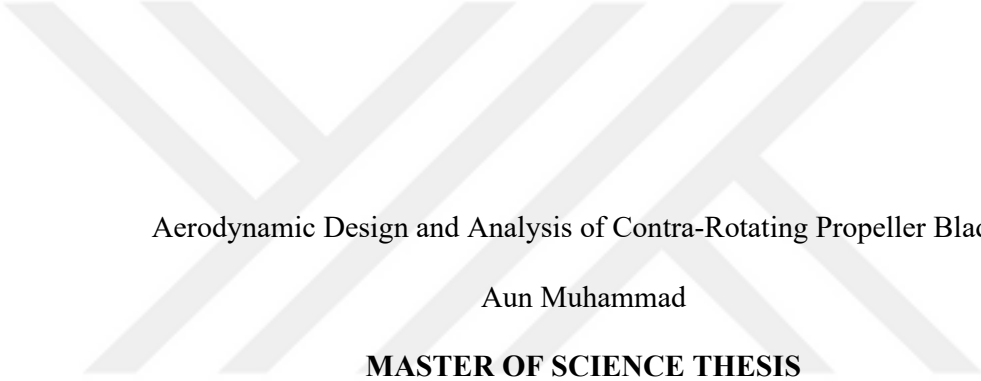
Ters Döner Pervanelerin Aerodinamik Tasarımı ve Analizi

Aun Muhammad

YÜKSEK LİSANS TEZİ

Havacılık Bilimi ve Teknolojileri Anabilim Dalı

Kasım 2020



Aerodynamic Design and Analysis of Contra-Rotating Propeller Blades

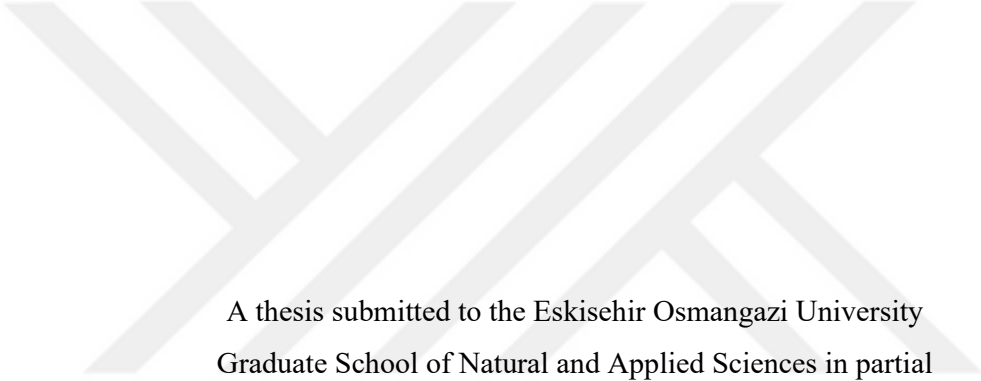
Aun Muhammad

MASTER OF SCIENCE THESIS

Department of Aviation Science and Technology

November 2020

Aerodynamic Design and Analysis of Contra-Rotating Propeller Blades



A thesis submitted to the Eskisehir Osmangazi University
Graduate School of Natural and Applied Sciences in partial
fulfillment of the requirements for the degree of Master of Science
in the Department of Aviation Science and Technology
by
Aun Muhammad

Supervisor: Prof. Dr. Zekeriya Altaç

November 2020

ETHICAL STATEMENT

I hereby declare that this thesis study titled “Aerodynamic Design and Analysis of Contra-Rotating Propellers” has been prepared in accordance with the thesis writing rules of Eskisehir Osmangazi University Graduate School of Natural and Applied Sciences under the academic consultancy of Prof. Dr. Zekeriya Altaç. I hereby declare that the work presented in this thesis is original. I also declare that I have respected scientific ethical principles and rules in all stages of my thesis study, all information and data presented in this thesis have been obtained within the scope of scientific and academic ethical principles and rules, all materials used in this thesis which are not original to this work have been presented in accordance with scientific ethical principles and rules. .../.../20... .

Aun Muhammad

Signature

ÖZET

Havacılığın çevresel etkisi günümüzde sürekli araştırma konusu olmaktadır. Gürültü emisyonu ve yakıt tüketimi, pervane arařtırmalarına ilginin yenilenmesine neden olan itici faktörlerden bazılarıdır. 1940'ların ve 1950'lerin eski teknolojileri yeterli pervane performansı sağlasa da, düşük yakıt tüketimi ve katı gürültü emisyon düzenlemeleri, pervane arařtırmalarını yeni ufuklara doğru yönlendiriyor. Ters Dönen pervaneler, her iki pervane de torku birbirinden ayırdığı için uçakta tork şeklinde bir avantaj sunmaktadır. Arka pervane, ön pervaneden atılan rüzgarın dönme kinetik enerjisini kullanır ve böylece itme veriminde bir artış gözlemlenir. Ön ve arka pervane arasındaki karmaşık etkileşimler gürültüye neden olur ve ters dönen pervanelerin ticari uygulamasını engellemektedir.

Bu tezde, düşük hızda çalışan ters dönen pervanelerin tasarım konuları ve aerodinamik etkileşimlerinin kapsamlı bir şekilde anlaşılmasına vurgu yapılmıştır. Çift pervane performansını hesaplama yöntemleri araştırılır ve standart çift dönen pervanenin itme ve tork dağılımlarını hesaplamak için kanat profillerinin kesit verileri kullanılır. Ters dönen pervanenin karmaşık akış alanının anlaşılması için, Sliding Mesh metodu kullanarak ayrıntılı bir CFD Analizi için uygulanmıştır ve sonuçlar literatürde bulunan Rüzgar Tüneli Test Verileri ve hesaplanmış kesit verileriyle karşılaştırılmıştır. Her iki pervanede aerodinamik yüklerin periyodik salınımları şeklinde ön ve arka rotor arasında aerodinamik etkileşimler gözlemlenmiştir. Benimsenen CFD metodolojisi, ters dönen pervanelerin analizi için verimli ve doğru bir araç ve daha ileri çalışmalar için güvenilir bir kriter olarak görülmüştür.

Anahtar Kelimeler: Ters Dönen Pervaneler, Pervane İzi, Periyodik Aerodinamik Yükler, İtme ve Tork Dağılımları

SUMMARY

The environmental impact of aviation is a subject of constant research nowadays. Noise emission and fuel consumption are some of the driving factors that have led to renewed interest in the research of propellers. Although the old technologies of the 1940's and 1950's give adequate propeller performance, low fuel consumption and strict noise emission regulations are driving propeller research into newer horizons. Contra-Rotating propellers offer an advantage in the form of torque on aircraft as both propellers cancel the torque from each other out. The aft propeller utilizes the rotational kinetic energy of the wake being shed from the front propeller and thus an increase in propulsive efficiency is observed. The complex interactions between the front and aft propeller give rise to noise which has hindered the commercial application of contra-rotating propellers.

In this thesis an emphasis is placed on a thorough understanding of the design considerations and aerodynamic interactions of contra-rotating propellers operating at low speed. Methods of calculating dual-propeller performance are investigated and section data of airfoils is used to calculate the thrust and torque distributions of a standard dual rotating propeller. For an understanding of the complex flow field of contra-rotating propeller, the Sliding Mesh approach has been implemented for a detailed CFD Analysis and the results are compared with Wind Tunnel Test Data available in literature as well as calculated section data. Aerodynamic interactions between the front and aft rotor in the form of periodic oscillations of the aerodynamic loads on both propellers has been observed. The CFD methodology adopted has been deemed to be an efficient and accurate tool for the analysis of contra-rotating propellers and a reliable benchmark for further study.

Keywords: Contra-Rotating Propellers, Propeller Wake, Periodic Aerodynamic Loads, Thrust and Torque Distributions

ACKNOWLEDGEMENT

I would like to thank God for everything that I was provided with, and everything that I was deprived of, for He is the Best of Providers.

To my parents, I would like to express my extensive gratitude for everything they have done for me. Words fall short in this regard.

To my supervisor, Prof. Dr. Zekeriya Altaç, I would like to thank him for his guidance, patience and support during the completion of this thesis. It was an honor working with him.

LIST OF CONTENTS

	<u>Page</u>
ÖZET	vi
SUMMARY	vii
ACKNOWLEDGEMENT	viii
LIST OF CONTENTS	ix
LIST OF FIGURES	xi
LIST OF TABLES	xiii
LIST OF ABBREVIATIONS AND SYMBOLS	xiv
1. INTRODUCTION	1
2. LITERATURE REVIEW	7
3. PROPELLER AERODYNAMICS	13
3.1. Momentum Theory	13
3.1.1. Introduction	13
3.1.2. Mathematical formulation	13
3.1.3. Ideal efficiency	15
3.2. Blade Element Theory	16
3.2.1. Introduction	16
3.2.2. Mathematical formulation	16
3.2.3. Efficiency of a blade element	20
3.2.4. Disadvantages of the simple (BEMT)	20
3.3. Goldstein Theory	20
3.4. Theodorsen's Theory	22
4. PROPELLER STRIP THEORY	24
4.1. Single Rotation Propellers	24
4.1.1. Introduction	24
4.1.2. Mathematical formulation	25
4.2. Dual-Rotation Propellers	29
4.2.1. Introduction	29
4.2.2. Mathematical formulation	30
4.3. Calculus of Variations Approach to Maximum Efficiency	33
5. STANDARD DUAL-ROTATING PROPELLER	36
5.1. Introduction	36
5.2. Propeller Geometry	37

LIST OF CONTENTS (continued)

	<u>Page</u>
5.3. Geometric Modelling	38
5.4. Propeller Wind Tunnel Tests: Tunnel Description, Conditions and Results	40
6. PROPELLER PERFORMANCE CALCULATIONS.....	42
6.1. Introduction.....	42
6.2. Assumptions.....	42
6.3. Expressions for Differential Thrust and Torque	42
6.4. Application of Method	43
6.4.1. Sheet 1 calculation	44
6.4.2. Sheet 2 calculation	45
6.4.3. Sheet 3 calculation	46
7. MESHING AND CFD ANALYSIS	47
7.1. Introduction.....	47
7.2. Domain Description	47
7.3. Grid Generation.....	48
7.4. Boundary Conditions and Methodology	51
7.4.1. Boundary conditions	51
7.4.2. Methodology of 3D computation	52
7.4.3. Determination of boundary conditions.....	53
7.5. The SIMPLE Algorithm.....	54
7.5.1. Introduction.....	54
7.5.2. Mathematical formulation	55
7.6. Numerical Setting	57
7.7. Run-Time and Limitations	58
8. RESULTS AND DISCUSSION.....	59
9. CONCLUSION AND SUGGESTIONS	66
REFERENCES.....	67
APPENDIX-A.....	69

LIST OF FIGURES

<u>Figure</u>	<u>Page</u>
1.1. Standard 5868-9 4-Bladed Propeller as visualized from the slipstream.....	3
2.1. FLIGHT Magazine cutaway of the Fairy Gannet (Anonim, 2008).....	7
3.1. General Conception of Flow Around a Propeller Blade	13
3.2. Blade Element of infinitesimal length on a Propeller Blade	16
3.3. Velocities of the Blade Element and Aerodynamic Forces.....	17
4.1. Propeller Velocity and Force Diagram - Single Rotation Propellers (Borst, 1973).....	25
4.2. Propeller Velocity and Force Diagram - Dual-Rotation Propellers (Borst, 1973).....	31
5.1. Six-blade single-rotating propeller with wing in place (Biermann & Gray, 1941).....	36
5.2. Isometric View of Eight Blade Dual-Rotating Propeller Geometric Model.	38
5.3. Side View comprising of station wise 'boxes' created for Hexahedral Meshing.....	39
5.4. Section View of propeller blades inside the 'box geometry'.	39
5.5. Efficiency Curves for 8-blade dual rotation (Biermann & Gray, 1941).....	40
5.6. Thrust Coefficient Curves for 8-blade dual rotation (Biermann & Gray, 1941).....	41
5.7. Power Coefficient Curves for 8-blade dual rotation (Biermann & Gray, 1941).....	41
6.1. Lift Curves of the Clark-Y Sections with infinite aspect ratio (Crigler & Talkin, 1942).	44
6.2. F-Curves for a Four-Blade Propeller (Crigler & Talkin, 1942)	45
6.3. Lift Drag Curves of the Clark-Y Sections with infinite aspect ratio (Crigler & Talkin, 1942)	46
6.4. Individual differential-torque curves for eight-blade dual-rotating propeller at $x = 0.7$, $\theta_1 = 50^\circ$, $\theta_2 = 48.7^\circ$	46
7.1. Rotary and Stationary Domains for CFD Analysis.	48
7.2. Blocking strategy for Hexa Meshing in ICEM CFD.....	49
7.3. Isometric View of Mesh on Blade and Streamline Body Surfaces.	50
7.4. Sectional View of Mesh showing entire domain.....	51
7.5. Boundary Conditions.....	52
7.6. Angle of rotation of the Contra-Rotating propeller blades, ψ°	53
7.7. Plot of Scaled Residuals, $\psi = 720^\circ$	57
7.8. Plot of Lift Coefficient Monitor at Front Rotor at $\psi = 720^\circ$	58
7.9. Plot of Lift Coefficient Monitor at Aft Rotor at $\psi = 720^\circ$	58
8.1. Periodic Variation of Front Propeller Thrust	59
8.2. Periodic Variation of Aft Propeller Thrust.....	59
8.3. Differential Thrust Distribution at $J = 2.57$, $\beta_1 = 50^\circ$, $\beta_2 = 48.7^\circ$	60
8.4. Differential Torque Distribution at $J = 2.57$, $\beta_1 = 50^\circ$, $\beta_2 = 48.7^\circ$	60
8.5. Vortex Core Region using the Lambda-2 Criterion, $\psi = 720^\circ$	62
8.6. Two-dimensional turbulent boundary layer velocity profile showing various layers (ANSYS, 2006).....	63
8.7. Contours of y^+ on blade surfaces (a) Front Propeller (b) Aft Propeller.....	63
8.8. Pressure Contours on Pressure Side (a) Front Propeller (b) Aft Propeller.....	64

LIST OF FIGURES (continued)

<u>Figure</u>	<u>Page</u>
8.9. Pressure Contours on Suction Side (a) Front Propeller (b) Aft Propeller.	64
8.10. Mach Number Contours in Stationary Frame at various blade sections at $\psi = 720^\circ$ (a) $x = 0.26$ (b) $x = 0.3$ (c) $x = 0.45$ (d) $x = 0.6$ (e) $x = 0.7$ (f) $x = 0.8$ (g) $x = 0.9$ (h) $x = 0.95$	65



LIST OF TABLES

<u>Table</u>	<u>Page</u>
1.1. Operating Conditions and Propeller Types (Borst, 1973).....	6
5.1. Blade Angle Distribution for Hamilton Standard 3155-5 and 3156-6 Blades (Biermann & Gray, 1941)	37
5.2. Chord Distribution for Hamilton Standard 3155-5 and 3156-6 Blades (Biermann & Gray, 1941)	37
5.3. Section Thickness Distribution for Hamilton Standard 3155-5 and 3156-6 Blades (Biermann & Gray, 1941)	38
7.1. CFD Cases run for determination of Boundary Conditions.	54
8.1. Comparison of Experimental, Calculated and CFD Results at $J = 2.57$, $\psi = 720^\circ$	61

LIST OF ABBREVIATIONS AND SYMBOLS

<u>Symbol</u>	<u>Description</u>
a	increment in velocity
A	rotating disc area
A	$A'\omega$
A'	average value of rotational inflow factor of front propeller
b	blade width
b	increment in velocity of slipstream
B	number of blades per propeller
c	chord of propeller blade element
C_D	section drag coefficient
C_L	section lift coefficient
C_x	section axial-force coefficient
C_y	section tangential-force coefficient
C_p	power coefficient
C_Q	torque coefficient
C_T	thrust coefficient
D	drag at blade element
D	diameter of propeller
F	correction factor for finite number of blades
G	computational quantity
H	pressure head
J	advance diameter ratio
k	mass coefficient for dual-rotating propellers
K	Goldstein circulation function
L	lift at blade element
n	rotational speed (revolutions/unit time)
P	power of propeller
Q	torque of propeller
r	radius to blade element
R	radius to blade tip

LIST OF ABBREVIATIONS AND SYMBOLS (continued)

<u>Symbol</u>	<u>Description</u>
T	thrust of propeller
u	average induced axial velocity of one propeller due to other
v	average induced tangential velocity of one propeller due to other
V	advance velocity of propeller
V_r	element velocity with respect to air
w	self-induced velocity at propeller
w	velocity of the screw surface
\bar{w}	displacement velocity ratio
W	resultant wind velocity at propeller
x	proportional radius at blade element
X	axial force at blade element
Y	tangential force at blade element

<u>Abbreviation</u>	<u>Description</u>
2D	Two-Dimensional
3D	Three-Dimensional
AoA	Angle of Attack
AR	Aspect Ratio
BEMT	Blade Element Momentum Theory
CCW	Counter Clock Wise
CFD	Computational Fluid Dynamics
CMM	Coordinate Measuring Machine
CROR	Contra-Rotating Open Rotor
CW	Clock Wise
MDO	Multi-Disciplinary Optimization
RANS	Reynolds Averaged Navier-Stokes
SIMPLE	Semi-Implicit Method for Pressure-Linked Equations
SRV	Swirl Recovery Vane
TWR	Total Width Ratio
WR	Width Ratio

LIST OF ABBREVIATIONS AND SYMBOLS (continued)

<u>Greek Letter</u>	<u>Description</u>
α	angle of attack
β	propeller blade angle
γ	drag-lift angle
ε	induced increase in angle of inflow
$\kappa(x)$	circulation function for single rotating propellers
$\kappa(x, \Theta)$	circulation function for dual rotating propellers
η	propulsive efficiency
θ	propeller blade angle at radius r
ρ	density of air
σ	solidity per propeller
π	the number pi
ϕ	angle of resultant wind with plane of rotation
ϕ_0	advance angle of blade element
ϕ'_0	effective advance angle of blade element due to induced velocity of other propeller
ϕ_w	helix angle of the vortex
Ω	angular velocity of propeller ($2\pi n$)
ω	ratio of angular velocities of front to rear propeller
<u>Subscript</u>	<u>Description</u>
1	front propeller
2	aft propeller

1. INTRODUCTION

A propeller is a device which generates thrust at the expense of power generated by a motor in order to propel a craft through a fluid medium.

Airscrew is the generally accepted term in aviation as the propeller twists its way through air while pushing back the fluid medium and developing a reaction force which propels the craft forward. The pushed back air called the slipstream, represents a loss. It has kinetic energy due to the twisting action of the propeller blades. Other losses are also present in the case of propellers such as the air friction acting on the blade surfaces. The thrust and power developed by a set of propeller blades is therefore always less than the power delivered by the engine to the propeller.

For a propeller designer, the most important aim is to design a system with a high ratio of thrust power to engine power, or in other words a high propulsive efficiency η . The primary function of a propeller is the conversion of shaft torque to shaft thrust. If the propeller is operating at a free stream velocity V , and is producing a thrust T , the propulsive efficiency (ratio between power output and power input) becomes:

$$\eta = \frac{TV}{550(hp)} = \frac{TV}{P} \quad (1.1)$$

The efficiency of a propeller at any given condition depends on the losses due to friction and losses due to acceleration of the fluid. *Induced loss* is defined as the loss in efficiency which occurs due to the production of thrust or acceleration of the fluid.

The *induced efficiency*, a measure of the induced loss is a measure of the efficiency when the profile drag of the blade sections is zero. Assuming no slip at the propeller surface, if the propeller were moving through the air, the induced efficiency would be 100%. However, since the propeller must accelerate air to produce thrust, the induced efficiency is always less than 100%. Induced efficiency accounts for all the losses due to acceleration of the fluid, including the axial, tangential and radial losses.

The *profile efficiency* of a propeller is a measurement of the losses due to friction. It depends on the drag of the 2D airfoil sections used for the blades, the operating lift, Reynolds Number, Mach Number and their distribution along the radius. Section drag of the blade will reduce the thrust and increase the power required and thus represents a direct loss. Profile efficiency is a measure of the losses due to drag of the blade section.

Some of the terminology associated with propellers is briefly explained as follows:

- Diameter, D: Diameter of the circle swept by blade tips.
- Boss: Central portion where Hub is mounted.
- Hub: Metal fitting incorporated in or with the propeller or engine shaft.
- Root: Portion of blade near the hub.
- Aspect Ratio, AR: Tip Radius divided by the maximum blade width.
- Width Ratio, WR: Blade Width at radius $0.75R$ divided by the diameter, D.
- Total Width Ratio, TWR: WR of one blade multiplied by total number of blades.
- Thickness Ratio of Section: Ratio of the thickness of section to the Blade Width.
- Thickness Ratio of Whole Propeller: Thickness Ratio of section at $0.75R$.
- Blade Angle, β : Acute Angle between the chord of a propeller section and plane perpendicular to the axis of rotation of the propeller.
- Effective Pitch: Advance per revolution. A propeller of fixed geometrical form may have a variety of forward speeds at the same revolution speed so that pitch in the usual sense is not fixed. The advance per revolution is of fundamental importance and is called 'Effective Pitch'.
- Geometrical Pitch: For an element, it is defined as the distance the element would advance in one revolution if it were moving in a helix having an angle equal to the blade angle, β .
- Nominal or Standard Geometrical Pitch: For a whole propeller, it is the pitch of the section at $2/3$ rds. of radius. If all the elements of a propeller have the same geometrical pitch, the propeller is said to have a uniform geometrical pitch.
- Rake/Tilt: For a propeller, it is defined as the mean angle which the lines joining the centers of area of the sections makes with a plane perpendicular to the axis of rotation.

- Tractor Propeller: Works in front of the engine/body.
- Pusher Propeller: Placed behind the body/back of the engine.
- Right-Handed Propeller: Viewed from the rear/slipstream rotates in a CW direction.
- Left-Handed Propeller: Viewed from the rear rotates in a CCW direction as shown in Figure 1.1.

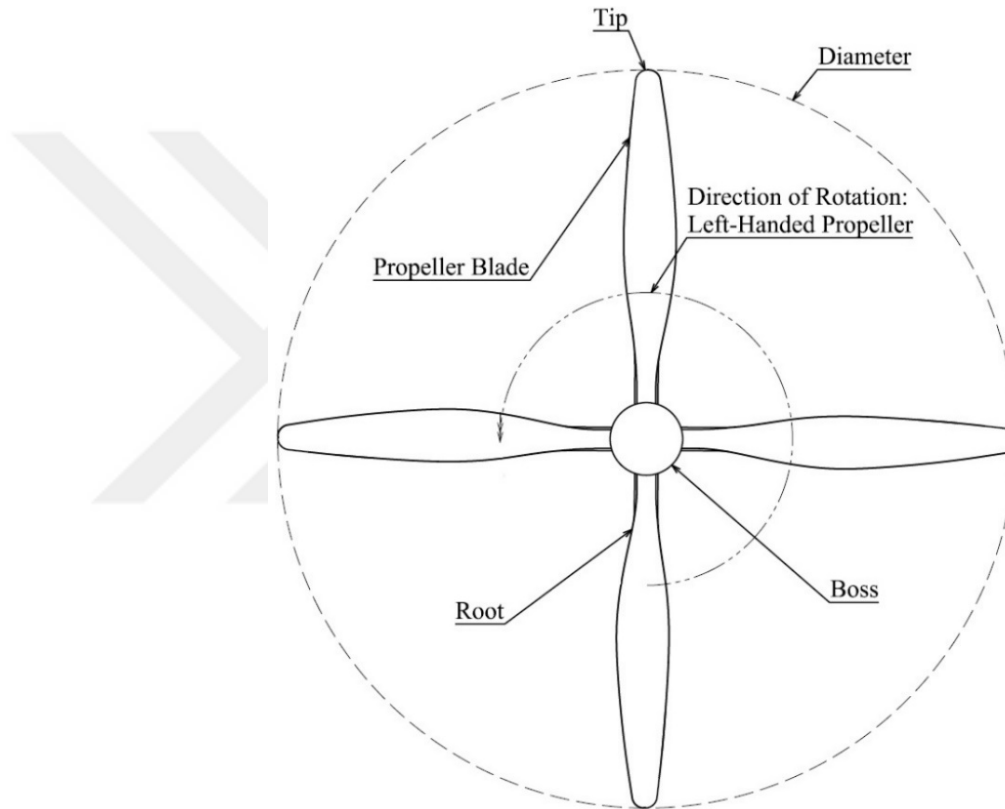


Figure 1.1. Standard 5868-9 4-Bladed Propeller as visualized from the slipstream.

The many variables involved which influence the final design of a propeller blade are airplane performance requirements, airplane geometric considerations, engine characteristics and propeller design factors. While establishing design criteria for propellers, one must consider the airplane design criteria such as the mission profile, aircraft performance characteristics, operational environment and maneuverability, geometric parameters and cost. In preparing the propeller design criteria, it is necessary to select suitable engines for final evaluation as the power available, rotational speed characteristics, specific fuel consumption and weight have a considerable influence on the propeller design.

To satisfy the requirements of a given propeller installation, the following parameters must be analyzed at all flight conditions. These parameters include:

- Propeller Diameter, D
- Blade Number, B
- Single or Dual Rotation
- Blade Activity Factor and Width Distribution
- Thickness Ratio Distribution
- Design Lift Distribution
- Blade Angle Distribution
- Blade Section Type

The propeller diameter, D , is the most important parameter when considering propeller design parameters. It is not only required to determine the blade loading, but also influences other factors. For peak efficiency, the velocity of the wake must be small. For obtaining higher levels of thrust at peak efficiency, the mass flow rate of air through the blades must be high.

Since the mass of air handled by the propeller increases with an increase in forward speed, the velocity increment needed for the same level of thrust decreases and the ideal efficiency will increase with increased speed. At low speeds a large mass flow rate is required to achieve a higher induced efficiency. The propeller diameter required for a given efficiency is therefore dependent on the operating requirements, speed and altitude. As the speed increases, the requirement for a low disc loading decrease.

For a given operating condition, the total solidity required is a function of the disc loading and therefore is also dependent on the propeller diameter.

Blade Number and Blade Solidity (Blade Activity Factor) are interrelated and a combination is established so that the blade will operate at a lift coefficient close to that for peak L/D ratio and thus peak profile efficiency. The peak lift/drag ratio that can be achieved is dependent on the sectional airfoil characteristics such as section type, thickness ratio and blade camber (Design C_L).

The choice of number of blades vs blade solidity is dependent on both structural and induced efficiency considerations after the blade solidity has been established. Propellers with a large number of blades will have a high induced efficiency because it is a function of the velocity and its uniformity in the final wake. For low disc loadings, propellers with three or four blades operate close to the value of maximum induced efficiency.

In cases of high disc loadings and critical low speed conditions such as take-off or early climb, six- and eight-blade propellers are required. These propellers have high rotational induced losses to counter which half of the blades are operating should rotate in the opposite direction of rotation. The aft propeller recovers the rotational energy losses of the front propeller in this way. Dual rotation propellers are especially useful in scenarios of high rotational losses.

The design lift coefficient or camber of an airfoil is an important parameter in the practical design of a propeller. For low-speed operation, a high design C_L in the range of 0.5 to 0.7 is generally considered best, as the L/D ratio peaks at these levels of camber.

For optimum load distributions, blade camber and blade angle distributions are generally determined together so that the optimum load distributions are obtained. It may be possible to obtain optimum load distribution at more than one station on the blade.

Section type depends on the propeller application. Generally, the section choice depends on the spread of the operating lift coefficient, the thickness ratio and the peak section Mach number. NACA 65 sections have a better range of peak L/D than others. Whereas, NACA 16 sections tend to operate at higher section Mach numbers without encountering the drag rise due to compressibility in comparison with the 6 series sections.

Operating Conditions are important factors to consider during the selection of propeller blades. For low-speed conditions, it is desirable to attain a high value of lift coefficient while for high-speed applications, a consideration of compressibility effects is necessary. The propeller types to achieve various design objectives explained in Table 1.1.

Table 1.1. Operating Conditions and Propeller Types (Borst, 1973).

Operating Condition	Propeller Type
Subsonic	Single Rotation
Subsonic	Dual Rotation
Transonic	Single Rotation
Transonic	Dual Rotation
Supersonic	Single Rotation
Supersonic	Dual Rotation
Ducted	Single and Dual Rotation

For a subsonic propeller all sections operate below their section critical Mach numbers. Disc loading, power input and sectional properties such as thickness ratio and camber determine the blade number and blade width. Solidity determines the maximum blade width and it must be less than 1.0 at any blade section.

A second row of blades is required if the total solidity exceeds 1.0 for operation over the complete range of blade angles. Torque reaction on the airplane is zero in case of properly designed dual rotation propellers since they have an axial outflow velocity only.

2. LITERATURE REVIEW

The idea of dual-rotation or contra-rotating propellers originated during the time of World War II for high-speed flight. Pankhurst et al. (1948) conducted extensive testing to determine the performance and installation effects of dual rotation propellers on aircraft. Some of the aircraft that have been installed with dual-rotating propellers are: Fairy Gannet (Figure 2.1) and Douglas XB-42 Mixmaster.

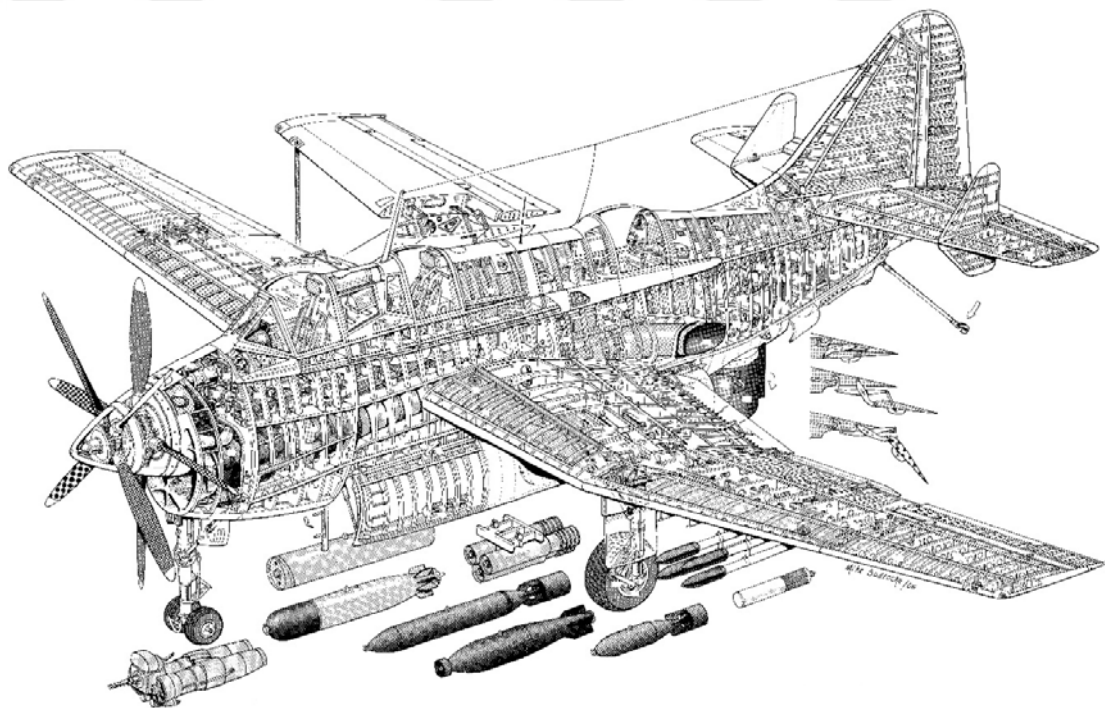


Figure 2.1. FLIGHT Magazine cutaway of the Fairy Gannet (Anonim, 2008).

Contra-Rotating propellers offer an advantage in the form of torque on aircraft as both propellers cancel the torque from each other out. Contra-rotating propellers are around 6-16% more efficient than normal propellers however they produce a lot of noise with an increase of up to 30 dB in the axial direction and around 10 dB in the tangential direction (Vanderover & Visser, 2000). This disadvantage limits commercial application.

The environmental impact of aviation is a subject of constant research nowadays. Noise emission and fuel consumption are some of the driving factors that have led to renewed interest in the research of propellers. Although the old technologies of the 1940's and 1950's give adequate propeller performance, low fuel consumption and strict noise emission regulations are driving propeller research into newer horizons.

During the 1930's and 1940's they remained a subject of active research, however, after World War II, the development of jet engines presented itself as a shift of priorities so to say for propeller research and work was abandoned until it was taken up by NASA in the 1980's for the development of the prop-fan or more commonly known as the Contra-Rotating Open Rotor (CROR).

Siddappaji & Turner (2015) have developed a new methodology based on the Blade Element Moment Theory (BEM) for contra-rotating propeller. Front Propeller wake and tip loss factor (Prandtl) have been taken into account. Brent's method has been used to solve for the non-linear relationship between the inflow angles and induction factors. The achieved blade geometry (airfoil, chord and twist distributions) is later optimized using a Genetic Algorithm with a single objective function for a given value of thrust. This low fidelity design methodology has provided a quick, robust and computationally inexpensive solution to the contra-rotating propeller design problem.

Asnaghi et al. (2019) have investigated the effect of roughness application on the tip vortex properties of marine propellers and consequent mitigation of tip vortex cavitation. A rough wall function has been applied in the roughened areas of the propeller and the SST- $k\omega$ closure equations have been used for turbulence modeling. 32 cells per vortex diameter have been used for an appropriate grid resolution of the roughened regions of the blade. The roughness is shown to have an impact on the propeller performance and an optimization of the roughened area is performed using a tradeoff between roughness area and performance degradation. It has been shown that cavitation mitigation may be performed on the propeller blade without a major setback to performance.

Stokkermans et al. (2019) have carried out an investigation on the analysis and design of wing-tip mounted propellers using the very interesting concept of distributed propulsion.

Wing-tip flow field results from a 3D RANS CFD simulation are averaged radially and are used in the optimization and performance evaluation of a wing-tip mounted propeller. The gains achieved in the propulsive efficiency are significant. Interestingly, the section efficiency of the inboard sections of the blade has been shown to increase and the thrust distribution of the propeller blades has taken a shift inboard.

Inukai (2011) has investigated the design of Marine Propellers with tip-raked fins. Potential Theory calculations were made to determine the hydrodynamic characteristics of tip-raked fin propellers. Three rake distributions were selected as candidate configurations for determination of pressure distribution: forward, backward and without rake. The backward tip rake configuration was shown to have a decrease in the negative pressure on the suction side of the blade whereas the forward rake configuration led to a greater negative pressure as compared to the base propeller. The results of the Potential Theory calculations were compared with Open Water Tests and found to be in good agreement with a stated increase of 1.5 percent in the efficiency of the tip rake compared to the conventional design.

Oliveira et al. (2012) have analyzed the accuracy of the Vortex Theory to propeller performance prediction of high rotation propellers operating at a low Reynolds Number operating between 60,000 and 160,000 and high rotation 10,000 RPM. Coordinate Measuring Machine (CMM) data for a 13-inch propeller was obtained, the aerodynamic characteristics were determined in XFOIL and MATLAB was used in the implementation of the Vortex Theory. Wind Tunnel Tests were conducted after application of corrections and the results were compared. It was shown that there is an error of 8.8 percent in the prediction of maximum efficiency using the Vortex Theory. The results in the low advance ratio regime however show good agreement.

Sinnige et al. (2018) have researched the aerodynamic and aero-acoustic performance of a propeller with Swirl Recovery Vanes (SRV's). SRV's are known to increase the propulsive efficiency of the propeller system by utilization of the rotational kinetic energy of the incoming wake from the front propeller. An experimental investigation was also conducted in a low-speed wind tunnel. RANS equations were solved in the numerically in commercial CFD Code ANSYS Fluent. The $k-\omega$ SST model was used for closure of the equations and y^+ remained of the order of 11-30. Velocity field measurements

were also made using the PIV method to compare with CFD results obtained and qualitative agreement was achieved. Noise penalty was investigated by measuring the tonal and broadband noise emissions for the propeller system with SRV's and it was observed that the addition of SRV's imposes a tonal noise penalty whilst enhancing the propulsive efficiency of the front propeller. It was also concluded that an SRV designed with an optimized variable pitch would help maintain the efficiency of the propeller over a wider range of blade loadings.

Wang et al. (2014) have investigated the design and analysis of swirl recovery vanes for a scaled down Fokker 29 propeller. Three candidate configurations of SRV were designed employing circular airfoils with variable pitch and chord distributions and it was observed that the SRV with the highest solidity provided the greatest increase in the thrust however lower efficiency which requires further study into the optimal vane design due to the complex aerodynamic interactions between the front and the aft rotors.

Luan et al. (2019) have investigated the effect of rotor-rotor spacing on the effect of noise produced by a Contra-Rotating fan. It was observed that by an increase in the distance between the two rotors, a reduction in the noise levels is achieved while the unsteady effects remain constant. Unsteady RANS simulations were conducted in ANSYS CFX and the equations were closed using the $k-\omega$ SST model. On the blade surface, sound pressure pulsation signals were extracted. These results were later used as a sound source for the solution of the acoustic wave equation in the frequency domain. An increase in the axial spacing between both rotors led to a drop of 17.2 dB in the sound pressure level.

Marinus (2012) investigated the benefits of blade shapes that have resulted from the multi-disciplinary optimization of high-speed propellers. The parameters that were used to benchmark the selected four candidate blade configurations were the aerodynamic and aero-acoustic performance. The blades were subjected to similar flow fields and hence the thrust they produced varied or they were set to produce the same thrust which resulted in dissimilar flow fields around them. The MDO of single aircraft propellers has resulted in larger chords in the outboard sections of the blades giving rise to a lumped mass with no significant aero-elastic disadvantages. It was observed that the humps on these blades result in a lower aerodynamic load on the humped part while the tip remains highly loaded. The propulsive

efficiency is reduced due to the humped configuration however a decrease in the sound pressure level is observed.

Villar et al. (2019) have undertaken an airfoil optimization study on two configurations of Contra-Rotating Open Rotors made of a different set of airfoils. Multi-Objective airfoil optimization has been done and both the blade profiles have been optimized keeping the aerodynamic performance in mind. The point of interest in both the optimizations has remained the maximum thrust condition and efficiency following aircraft climb. Evolutionary Algorithms have been used in conjunction with 3D RANS simulations for this study. The configuration with the NACA-16 family of airfoils has outperformed the parameterized airfoil as the latter's optimization remained unconverged.

Hall et al. (1990) have researched the aerodynamics ducted prop-fans. For the numerical analysis time-dependent Euler equations were solved for two separate meshes using H-Grids and O-Grids. For the verification of the Euler solver, the un-ducted configuration was first solved; the same methodology was then extended to ducted flows around the prop-fan. The results were compared with experimental data. Both the grids were shown to provide similar results however; the cowl leading edge region of the ducted prop-fan was better resolved with the C-Grid.

Stuermer & Yin (2009) have investigated the low-speed performance considering aerodynamic and aero-acoustic considerations of Contra-Rotating Open Rotors. General Electric GE36 UDF has been chosen as the nacelle configuration as results of flight tests from the Boeing-727 and McDonnell Douglas MD-80 exist in literature. The geometric model was created in CATIA and the CentaurSoft Centaur software was used for mesh generation for the nacelle. Structured meshes for the rotors are created in the ICEM CFD Software. Appropriate boundary layer resolution was determined for both the nacelle and the rotors. C and O Grids are used to mesh the rotors and their surroundings. CFD Analysis is carried out and a periodic change in the blade loading of the aft rotor is observed due to its interaction with the tip vortex of the front rotor. A good resolution of the mesh has provided a good resolution of wake visualization and interaction.

Nallasamy & Groeneweg (1991) have studied the aerodynamic characteristics of a propeller operating under an angle of attack by using the unsteady Euler three dimensional techniques. The blade subjected on an inflow angle of air was tested at two different Mach Numbers of 0.2 and 0.5. The computational results were in good agreement with the Wind Tunnel results at Mach 0.5 however, the pressure distributions at the lower Mach of 0.2 did not match the Wind Tunnel results. Leading edge vortex formation was observed at Mach 0.2 which has a qualitative agreement with the numerical data. Non-linear response was measured at the suction surface of the blade. A further investigation is required as the current inviscid analysis fails to predict it.

Brocklehurst & Barakos (2013) have reviewed the rotor tip technologies that are in use already or that may have been suggested for use. Vibrations, acoustics and performance are heavily influenced by the design of the rotor tip. The forward and retreating parts of the rotor disc are subjected to cyclic variations in the Mach and Reynolds Numbers. The tip of the advancing rotor of a helicopter in forward flight may experience sonic conditions as the velocity of the aircraft is added to it. The tail-rotor is subject to high-blade loadings and therefore and requires a tip design such that the drag due to flow separation resulting from high angles of attack is mitigated. Acoustic considerations are also important as the aircraft may be subjected to blade-vortex interaction in certain flight conditions. CFD has presented a better opportunity compared to old methodologies for the design of the helicopter rotor tips.

3. PROPELLER AERODYNAMICS

3.1. Momentum Theory

3.1.1. Introduction

Propeller in order to provide a thrust must give motion to a mass of air in a direction opposite to thrust. Simple Momentum Theory was developed by Rankine and R.E. Froude and is based on the consideration of the momentum and kinetic energy imparted to the mass of air. Froude Theory considers the propeller disc as a whole whereas Rankine divides it into elementary annular rings and deals with one ring at a time and summing up the effects later to capture the combined effect of the rings as a whole.

3.1.2. Mathematical formulation

Propeller is assumed to be an advancing disc producing a uniform thrust T , air pressure being different in the front and back of the disc by a constant amount over its area. This hypothetical disc is also referred to as the actuator disc and can be imagined as a propeller having an infinite number of blades. Flow of air is streamline and continuous on either side of the propeller so that the axial velocity is the same immediately in the front of and behind the disc. No torque acts on the disc and no rotation is imparted to the air flowing through the disc. Air is a perfect fluid having no viscosity and is incompressible.

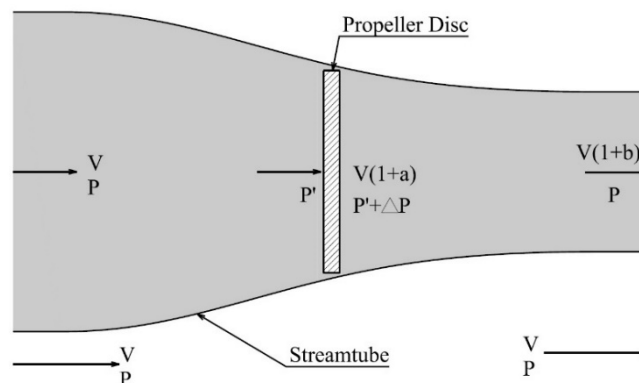


Figure 3.1. General Conception of Flow Around a Propeller Blade

As shown in Figure 3.1, air stream has a velocity V and pressure P in the far field away from the influence of the propeller. In front of the disc, the pressure is reduced to P' and after passing through the disc, it receives an increment ΔP . Upon approaching the disc, the airstream velocity is given an increment aV and as it passes through the disc it has a constant value $V + aV$. A further increase of $V + bV$ is given to the airstream velocity in the slipstream or wake. The added velocity in the slipstream is bV and the pressure has fallen to its original value P .

Flow is being regarded as potential except in passing through the actuator disc. We may apply Bernoulli's Equation to the air in front of and behind the disc. Bernoulli's Equation states that along a stream tube, the total head of the fluid:

$$H = P + \frac{1}{2} \rho V^2 = \text{constant} \quad (3.1)$$

Total head in front of the disc:

$$H = P + \frac{1}{2} \rho V^2 = P' + \frac{1}{2} \rho V^2 (1+a)^2 \quad (3.2)$$

Total head at the back of the disc is:

$$H_1 = P' + \Delta P + \frac{1}{2} \rho V^2 (1+a)^2 = P + \frac{1}{2} \rho V^2 (1+b)^2 \quad (3.3)$$

The difference in pressure between the front and the back of the disc is therefore:

$$\Delta p = H_1 - H = \left[P + \frac{1}{2} \rho V^2 (1+b)^2 \right] - \left[P + \frac{1}{2} \rho V^2 \right] = \rho V^2 b \left(1 + \frac{b}{2} \right) \quad (3.4)$$

Also, thrust equals rate of change of angular momentum in unit time,

$$T = \text{mass per unit time} \times \text{velocity change}$$

$$T = AV(1+a)\rho bV = AV^2\rho b(1+a) \quad (3.5)$$

Equating both the expressions for thrust, we get:

$$a = \frac{b}{2} \quad (3.6)$$

Based on the Momentum Theory, it may be stated that half of the velocity imparted to the slipstream occurs in front of the propeller disc and half of it behind.

3.1.3. Ideal efficiency

The work done on the fluid per unit time is the same as the rate of increase of the Kinetic Energy of the fluid.

$$\text{Energy} = \frac{1}{2} \rho AV(1+a)[V^2(1+b)^2 - V^2] = \rho AbV^3(1+a)^2 \quad (3.7)$$

In order to find the useful work done by the thrust, it is convenient to go back to the state in which the propeller is advancing with velocity V , through the fluid at rest, the thrust and velocity being in the same relation to each other as before. Efficiency becomes:

$$\eta = \frac{TV}{\rho AbV^3(1+a)^2} = \frac{\rho AbV^3(1+a)}{\rho AbV^3(1+a)^2} = \frac{1}{1+a} \quad (3.8)$$

The above equation represents the ideal efficiency it is always less than 1 because of additional losses.

1. Due to torque, there is an energy of rotation of the slipstream.
2. Energy is lost due to frictional effects.
3. Thrust distribution along the blade span is not constant.
4. The number of blades is finite.

3.2. Blade Element Theory

3.2.1. Introduction

William Froude came up with the idea of analyzing forces on elementary strips of propeller blades in 1878. While Momentum Theory provides a useful relation for the ideal efficiency, it does not take the effect of torque into consideration. The Blade Element Theory deals with the forces on the propeller blades in comparison with the Momentum Theory which considers the flow of air only.

3.2.2. Mathematical formulation

The propeller blade is considered having a section with a tip and chord distribution that varies along the span of the blade. The propeller blade is assumed to be made up of small elements and the aerodynamic forces on each element are calculated.

Airflow around each element is considered to be $2D$. Air passes through the propeller with no radial flow (i.e., no contraction of slipstream in passing through the disc) and that there is no blade interference. Consider an infinitesimal element located at a radius r with infinitesimal width dr and width b (Figure 3.2). Motion of this element in flight may be visualized as having a helical path determined by the forward velocity V and tangential velocity $2\pi r n$ of the element in the plane of the propeller disc where n represents the revolutions per unit time.

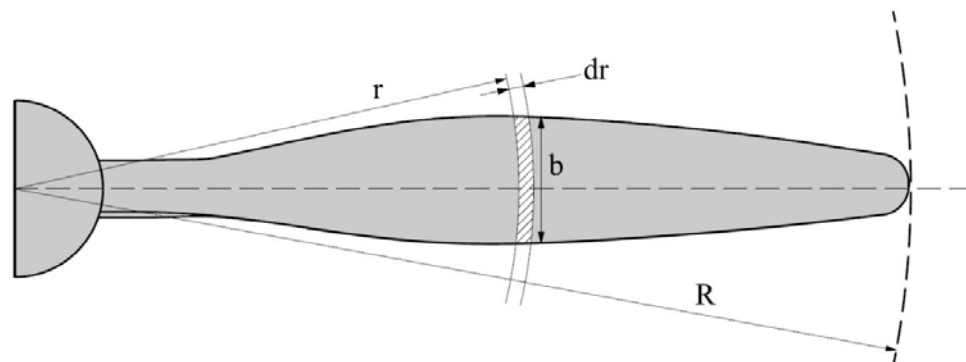


Figure 3.2. Blade Element of infinitesimal length on a Propeller Blade

The velocity of the element with respect to air is V_r . This velocity is the resultant of the forward and tangential velocities of the element. The angle between the direction of motion of the element and the plane of rotation is denoted by ϕ and the blade angle by β .

Angle of attack relative to air is:

$$\alpha = \beta - \phi \quad (3.9)$$

Applying the airfoil coefficients, the lift force on the element is:

$$dL = \frac{1}{2} \rho V_r^2 C_L b dr \quad (3.10)$$

Assuming γ to be the angle between the lift component and the resultant force, we have (Figure 3.3):

$$\gamma = \tan^{-1}\left(\frac{D}{L}\right) \quad (3.11)$$

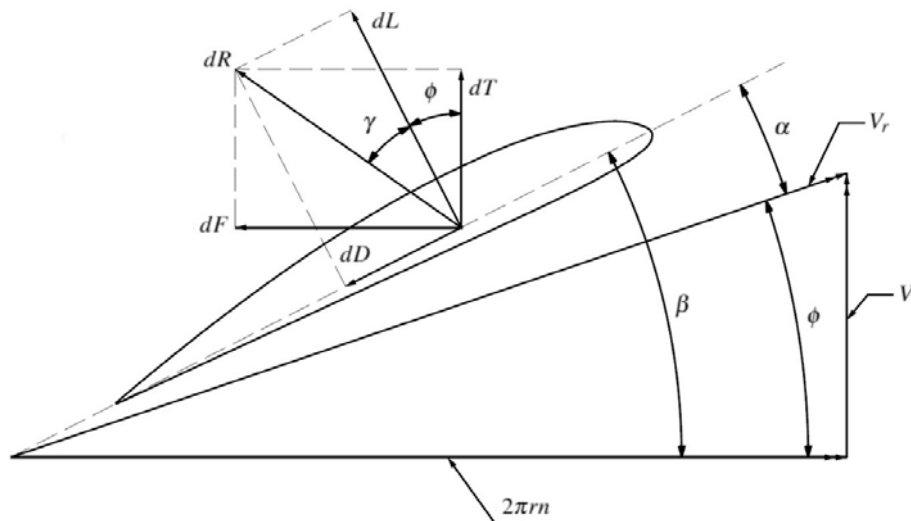


Figure 3.3. Velocities of the Blade Element and Aerodynamic Forces

Total resultant aerodynamic force on the element is:

$$dT = dR \cos(\phi + \gamma) = \frac{\frac{1}{2} \rho V_r^2 C_L b dr \cos(\phi + \gamma)}{\cos \gamma} \quad (3.12)$$

Similarly, the thrust on the element becomes:

$$dT = dR \cos(\phi + \gamma) = \frac{\frac{1}{2} \rho V_r^2 C_L b dr \cos(\phi + \gamma)}{\cos \gamma} \quad (3.13)$$

Since,

$$V_r = \frac{V}{\sin \phi} \quad (3.14)$$

Substituting this value in the previous equation we have,

$$dT = \frac{\frac{1}{2} \rho V^2 C_L b dr \cos(\phi + \gamma)}{\sin^2 \phi \cos \gamma} \quad (3.15)$$

For convenience, let

$$K = \frac{C_L b}{\sin^2 \phi \cos \gamma} \quad (3.16)$$

$$T_c = K \cos(\phi + \gamma) \quad (3.17)$$

then,

$$dT = \frac{1}{2} \rho V^2 T_c dr \quad (3.18)$$

The total thrust of the propeller with B blades becomes:

$$T = \frac{1}{2} \rho V^2 B \int_0^R T_c dr \quad (3.19)$$

Tangential or Torque Force is:

$$dF = dR \sin(\phi + \gamma) \quad (3.20)$$

Correspondingly, Torque on the element is:

$$dQ = rdR \sin(\phi + \gamma) \quad (3.21)$$

If,

$$Q_c = Kr \sin(\phi + \gamma) \quad (3.22)$$

Then it may be stated that:

$$dQ = \frac{1}{2} \rho V^2 Q_c dr \quad (3.23)$$

The expression for the torque on the whole blade becomes:

$$Q = \frac{1}{2} \rho V^2 B \int_0^R Q_c dr \quad (3.24)$$

The horsepower absorbed by the propeller is:

$$\text{QHP} = \frac{2\pi nQ}{550} \quad (3.25)$$

The efficiency is:

$$\eta = \frac{\text{THP}}{\text{QHP}} = \frac{TV}{2\pi nQ} \quad (3.26)$$

3.2.3. Efficiency of a blade element

It is not possible to obtain simple expressions for the thrust, torque and efficiency of the propeller blades in general due to the variation of the blade width, angle and airfoil section along the blade. The element at $0.75R$ is a fair representation of the whole blade.

$$\eta = \frac{dTV}{dQ2\pi n} \quad (3.27)$$

$$\eta = \frac{dR \cos(\phi + \gamma)V}{dR \sin(\phi + \gamma)2\pi nr} \quad (3.28)$$

$$\eta = \frac{\tan \phi}{\tan(\phi + \gamma)} \quad (3.29)$$

3.2.4. Disadvantages of the simple (BEMT)

Some of the disadvantages of the Simple Blade Element Momentum Theory are:

1. Interference effects between blades are not considered.
2. Tip Losses not taken into account. Thrust and Torque as computed by this theory are thus greater near the tip.

3.3. Goldstein Theory

The Basic Momentum Theory considers velocity losses in the axial direction only whereas in reality, losses exist in the tangential and radial directions too. Moreover, the axial

velocity is not constant across the disc. For actual propellers, a more extensive theory is therefore required to find the induced losses.

Knowing the induced efficiency requires finding out the induced velocity at every blade station on the propeller and the induced losses. For application of 2D airfoil data, knowing the 2D flow conditions at a particular blade station is required. The induced and profile efficiencies and consequently, the total blade efficiency may then easily be found.

For a calculation of the induced velocity at a given load distribution, it is necessary to assume the position of the vortices in the final wake, calculate the induced velocity at the propeller, find a new vortex wake. This is an iterative process.

Goldstein, using the concept of rigid vortex sheets, developed the first practical solution for calculating the induced velocity for a propeller with a finite blade number operating in incompressible flow using a vortex theory similar to wing theory. He assumed that the circulation at the root and tip is zero; the blade is represented by a lifting line with strength $\delta\Gamma / \delta r$ equal to the change in circulation between stations. These vortex lines form helical vortex sheets that extend from the blade to infinity.

For minimum power, it has been shown by Betz that the vortex sheets behind the propeller will be rigid. The vortex sheets are assumed to be rigid behind the propeller and the induced velocity may now be found.

The vortex sheets were placed in a potential stream by Goldstein for calculating conditions at the propeller. Helical pitch angle is equal to:

$$\phi = \tan^{-1} \frac{V}{\pi n D} \quad (3.30)$$

Induced velocity may be neglected is very small compared to the free-stream velocity. Light loading and zero slip have been assumed. Using Bessel functions, Goldstein solved the potential flow problem with Bessel function and generated coefficients that could be used to find the induced velocity as a function of advance ratio.

The strength of the circulation was related to the velocity of the screw surface w by the relationship shown in the equation below:

$$\kappa(x) = \frac{B\Gamma \omega}{2\pi V_w} \quad (3.31)$$

Thus, the potential solution developed by Goldstein was a major step development of the theory of propellers, as it provided the data required for the application of 2D airfoil data.

3.4. Theodorsen's Theory

Theodorsen extended the vortex theory developed by Goldstein to the heavy loading case. The same basic concepts of the rigid helical surface, zero circulation at the tip and root, a circulation whose strength is equal to $\delta\Gamma / \delta r$ at a given blade station are also used by Theodorsen. The main difference between the Goldstein and Theodorsen theories is the handling of the potential flow solution.

The wake of the helical screw surface is dependent on the advance ratio and the displacement velocity, w . The displacement velocity w is defined as the velocity of the screw surface in the direction of its axis. The helix angle is:

$$\phi_w = \tan^{-1} \frac{V + w}{\pi n D} \quad (3.32)$$

The use of the helical angle in the final wake based on its actual pitch leads to a new definition of the term $\kappa(x)$. Theodorsen uses:

$$\kappa(x) = \frac{B\Gamma_w}{2\pi(V + w)w} \quad (3.33)$$

Theodorsen's theory thus provides a better alternate for finding the flow conditions at the propeller in the slipstream, the induced efficiency and the detailed design as

Goldstein's theory introduces an error in the displacement and induced velocities. Using the electrical analogy technique with the actual models of helical vortices, Theodorsen found values of $\kappa(x)$ for single- and dual-rotation propellers at the blade stations from hub to tip.

The mass coefficient k for dual rotation propellers is:

$$k = \frac{1}{\pi} \int_0^{2\pi} \int_0^1 \kappa(x, \Theta) d\Theta x dx \quad (3.34)$$

and for single-rotation propeller, the expression assumes the form:

$$k = 2 \int_0^1 \kappa(x) x dx \quad (3.35)$$

The term k defined in the vortex theories of Goldstein and Theodorsen is the mass coefficient. It is used as a modifier for the application of the Momentum Theory to the 3D case. The mass-coefficient is particularly useful for calculating the performance of dual-rotation propellers.

4. PROPELLER STRIP THEORY

4.1. Single Rotation Propellers

4.1.1. Introduction

To use data from the vortex theory of propellers, Propeller Strip Theory has been developed for the determination of the induced efficiency and the induced velocity for the application of 2D airfoil data for the calculation the profile efficiency. The Strip Theory is used to find the performance of the propeller blade as it makes possible a complete analysis of all the details required. The effects of detailed changes of any sections of the blade can be determined and investigated. From the design perspective, this is an ideal scenario where the necessary changes to profile data may be applied until an optimum is achieved.

2D airfoil data may be applied by the determination of the induced velocity using the vortex theory. An assumption using the vortex theory when calculating the induced velocity at the propeller disc at any station, is that the blade is operating at the optimum load distribution. Near peak efficiency, this assumption introduces a very small error as the loading approaches an optimum.

The procedure involves finding the performance of a particular section from 2D airfoil data. Next, the lift and drag of the section are resolved in the thrust and torque directions for each blade station. Lastly, the differential thrust and torque may readily be integrated to find the total thrust and torque produced by the propeller. With the thrust and torque known, the efficiency and power absorbed may easily be found.

As the name implies, 2D airfoil data is obtained from Wind Tunnel Tests and is not representative of the 3D flow conditions at a propeller station. In the Wind Tunnel, the aerodynamic forces are measured and the angle of attack is determined. The true or equivalent velocity at any given section on the blade must be found by eliminating the three-dimensional effects from the vector diagram. This is done using the vortex theory for

calculating the induced velocity produced as a result of tip effect changes in loading on the blade.

4.1.2. Mathematical formulation

Consider a blade section at a radius r from the axis of rotation. The velocity and force diagram of the blade element is shown in Figure 4.1. The equations necessary to find the thrust and torque by strip analysis are developed as follows:

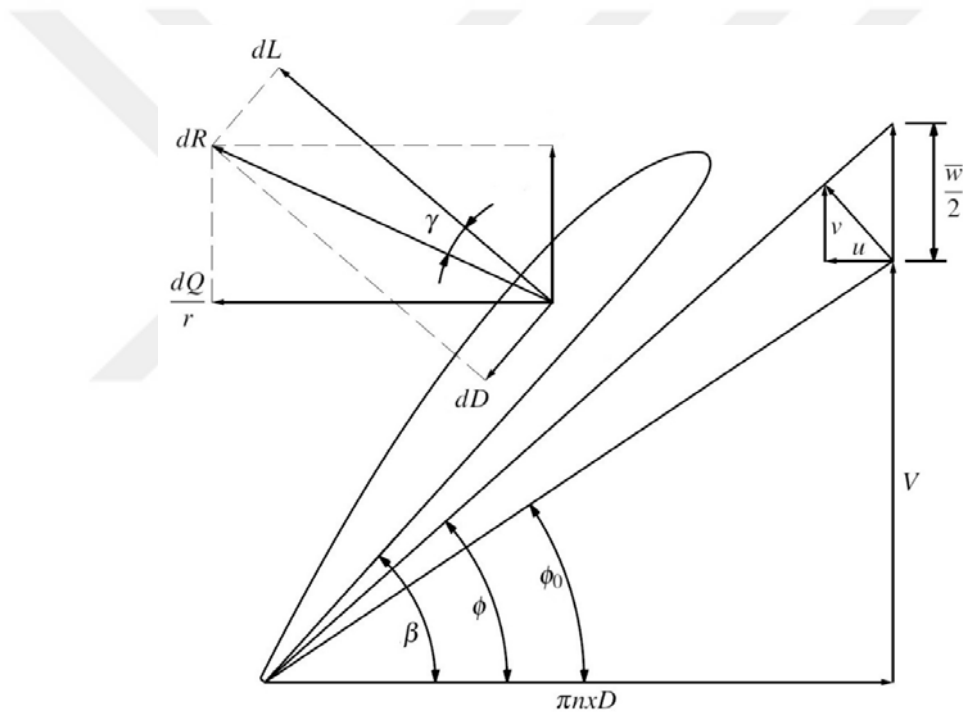


Figure 4.1. Propeller Velocity and Force Diagram - Single Rotation Propellers (Borst, 1973).

$$\frac{dQ}{r} = BdR \sin(\phi + \gamma) = B \frac{dL}{\cos \gamma} (\sin(\phi + \gamma)) \quad (4.1)$$

Since,

$$dL = \frac{1}{2} \rho C_L W^2 b dr \quad (4.2)$$

$$x = \frac{r}{R} \quad (4.3)$$

$$\sigma = \frac{dB}{\pi x D} \quad (4.4)$$

and,

$$dC_Q = \frac{dQ}{\rho n^2 D^5} \quad (4.5)$$

The above equation becomes:

$$\frac{dC_Q}{dx} = \sigma C_L \frac{x^2}{8} \left(\frac{W}{nD} \right)^2 (\sin \phi + \tan \gamma \cos \phi) \quad (4.6)$$

From the figure we have,

$$\frac{W}{nD} = \frac{\frac{V+W/2}{\sin \phi} - \frac{W}{2} \sin \phi}{nD} \quad (4.7)$$

and by definition, we have:

$$\bar{w} = \frac{w}{V} \quad (4.8)$$

$$J = \frac{V}{nD} \quad (4.9)$$

Combining the equations, we have:

$$\frac{dC_Q}{dx} = \frac{\pi x^2}{8} J^2 \left[\frac{1 + \frac{\bar{w}}{2} (1 - \sin^2 \phi)}{\sin \phi} \right]^2 \sigma C_L \sin \phi \left(1 + \frac{\tan \gamma}{\tan \phi} \right) \quad (4.10)$$

For convenience, let the quantity

$$\frac{\pi x^2}{8} J^2 \left[\frac{1 + \frac{\bar{w}}{2} (1 - \sin^2 \phi)}{\sin \phi} \right]^2 \sin \phi = z \quad (4.11)$$

The equation then becomes;

$$\frac{dC_Q}{dx} = \sigma C_L z \left(1 + \frac{\tan \gamma}{\tan \phi} \right) \quad (4.12)$$

Also, from the figure, we have:

$$dT = BdR \cos(\phi + \gamma) \quad (4.13)$$

Now, making the substitutions for dL , x and z as before, the equation for thrust becomes:

$$\frac{dC_T}{dx} = \frac{\pi x}{4} J^2 \left[\frac{1 + \frac{\bar{w}}{2} (1 - \sin^2 \phi)}{\sin \phi} \right]^2 \sigma C_L \sin \phi (\cot \phi - \tan \gamma) \quad (4.14)$$

Using the z term to simplify the above equation, we get:

$$\frac{dC_T}{dx} = \sigma C_L \frac{2z}{x} (\cot \phi - \tan \gamma) \quad (4.15)$$

The section AoA must be determined before the simplified equations for Torque and Thrust can be solved. The lift and drag coefficients can be found from 2D airfoil data.

$$\alpha = \beta - \phi \quad (4.16)$$

ϕ is found from the following expression:

$$\phi = \tan^{-1} \frac{J}{x} \left(1 + \frac{\bar{w}}{2}\right) \quad (4.17)$$

From the Kutta-Joukowski Theory:

$$\frac{dL}{dr} = \rho W \Gamma = \frac{1}{2} C_L \rho W^2 b \quad (4.18)$$

From the Vortex Theory of Theodorsen, we have:

$$\Gamma = \frac{(V + w)w}{Bn} \kappa(x) \quad (4.19)$$

Substituting for Γ and recalling by definition the Factor of Merit, we have:

$$C_L = \frac{2(V + w)w}{xDnW} \kappa(x) \quad (4.20)$$

From the figure it may be noted that:

$$W = \frac{V + w/2}{\sin \phi} - \frac{w}{2} \sin \phi \quad (4.21)$$

which becomes:

$$W = \frac{V}{\sin \phi} \left(1 - \frac{w}{2} \cos \phi\right) \quad (4.22)$$

Substituting the expression for W in the above equation, we have:

$$\alpha C_L = \frac{2(1 + \bar{w})\bar{w}\kappa(x)\sin^2\phi}{(1 + \bar{w}/2)(1 + \bar{w}\cos^2\phi/2)\cos\phi} \quad (4.23)$$

Since \bar{w} is dependent on C_L which is in turn dependent on α and \bar{w} it is necessary to solve the above equation in terms of the airfoil characteristic to find the operating C_L for each blade section, after which the differential thrust and torque components can be calculated. To determine the total thrust and torque coefficients, the differential values are integrated along the blade span. The following equations are obtained:

$$C_Q = \sum_{n=0}^{n=1} \alpha C_L z \left(1 + \frac{\tan\phi}{\tan\gamma}\right) \Delta x \quad (4.24)$$

$$C_T = \sum_{n=0}^{n=1} \alpha C_L \frac{2z}{x} (\cot\phi - \tan\gamma) \quad (4.25)$$

The expression for propeller efficiency thus becomes:

$$\eta = \frac{C_T}{2\pi C_Q} J = \frac{C_T}{C_P} J \quad (4.26)$$

4.2. Dual-Rotation Propellers

4.2.1. Introduction

The same technique for the performance of dual-rotation propellers may be used as was used for single-rotation. However, because of the interaction between the front and aft rotors, modifications to the differential thrust and torque equations as well as the equations for finding the true wind angle ϕ and the resultant velocity are necessary. These qualities are dependent on $\kappa(x, \Theta)$ and k . The same technique as for single rotation may be applied for finding the values of $\kappa(x, \Theta)$ and k . For complex flows around dual-rotating propellers, the electrical analogy technique used by Theodorsen for this purpose is especially effective.

In the case of dual-rotation propellers, the $\kappa(x, \Theta)$ is used rather than $\kappa(x)$ (used for the single-rotation case) as $\kappa(x, \Theta)$ is a function of not only x but also Θ . The angle Θ varies from 0° to 360° and at 0° , $\kappa(x, \Theta)$ is on the blade vortex for which the conditions are being calculated. An assumption is made that Θ equals 0° and at normal blade loadings, the error is small.

4.2.2. Mathematical formulation

Based on the theory of dual-rotation propellers developed by Theodorsen, the velocity and vector diagrams for the dual-rotation unit are shown in Figure 4.2. When calculating the flow vectors based on the Theodorsen data and theory, the following assumptions are made:

1. The front and rear sections are operating in the same plane.
2. Optimum loading condition exists for both propellers.
3. Both propellers absorb an equal amount of torque.

The resultant sectional velocity on the front and rear units may be calculated from the following equations:

$$W_1 = \frac{V}{\sin \phi_o} \left(1 + \frac{1}{4} k \bar{w} \sin^2 \phi_o \right) \quad (4.27)$$

$$W_2 = \frac{V}{\sin \phi_o} \left(1 + \frac{3}{4} k \bar{w} \sin^2 \phi_o \right) \quad (4.28)$$

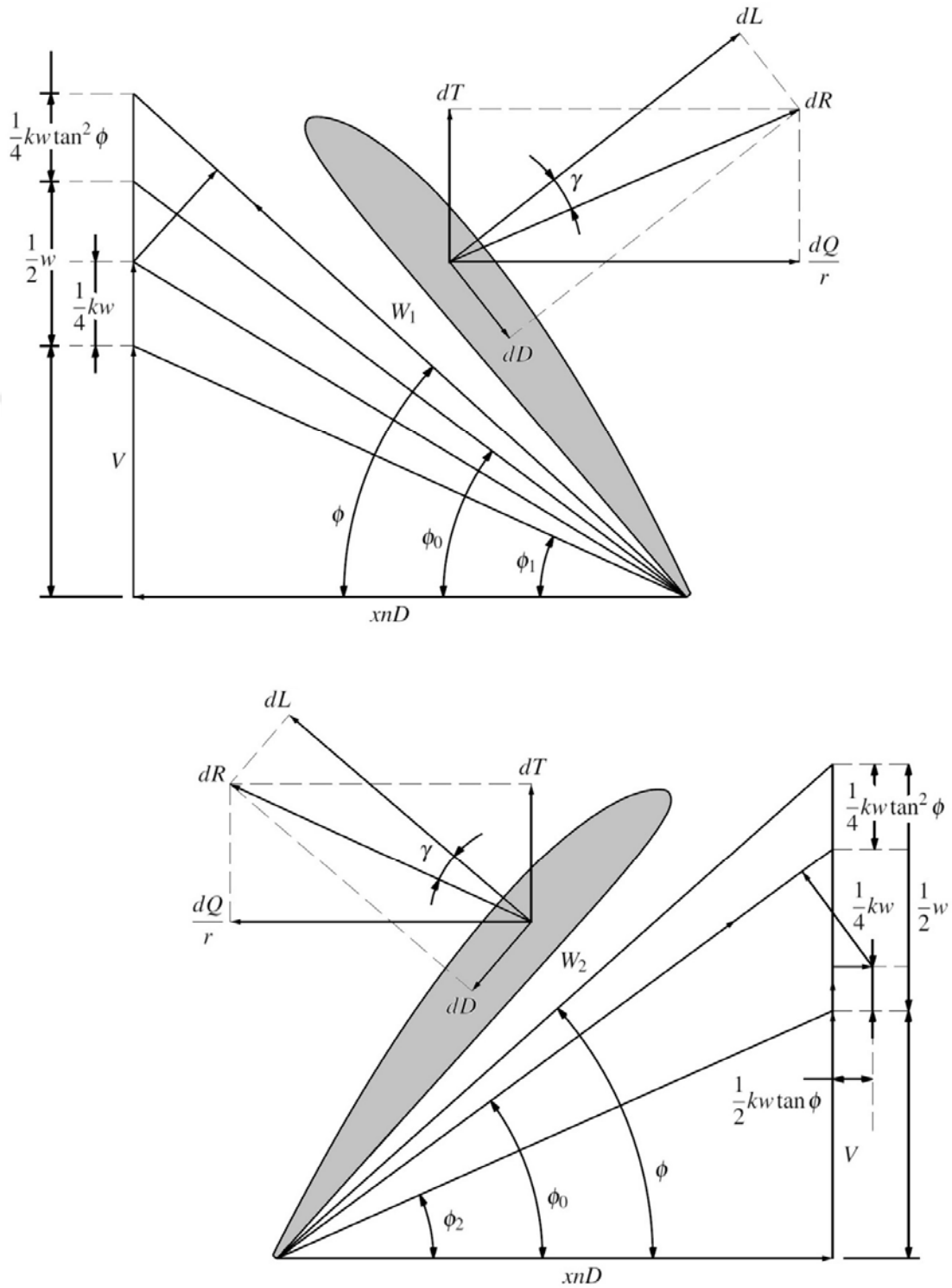


Figure 4.2. Propeller Velocity and Force Diagram - Dual-Rotation Propellers (Borst, 1973).

The differential thrust and torque coefficient for the front unit of a dual-rotation may be derived in the same manner as for single-rotation propellers. Thus,

$$\frac{dC_Q}{dx} = \frac{\pi x^2}{8} J \left(\frac{V}{\sin \phi_o} \right)^2 \left[1 + \frac{1}{4} k \bar{w} \sin^2 \phi_o \right]^2 \alpha C_L (\sin \phi + \tan \gamma \cos \phi) \quad (4.29)$$

$$\frac{dC_T}{dx} = \frac{\pi x}{4} J^2 \left(\frac{V}{\sin \phi_o} \right)^2 \left[1 + \frac{1}{4} k \bar{w} \sin^2 \phi_o \right]^2 \alpha C_L (\cos \phi + \tan \gamma \sin \phi) \quad (4.30)$$

For the rear unit of the dual-rotation, we have:

$$\frac{dC_Q}{dx} = \frac{\pi x^2}{8} J \left(\frac{V}{\sin \phi_o} \right)^2 \left[1 + \frac{3}{4} k \bar{w} \sin^2 \phi_o \right]^2 \alpha C_L (\sin \phi + \tan \gamma \cos \phi) \quad (4.31)$$

$$\frac{dC_T}{dx} = \frac{\pi x}{4} J^2 \left(\frac{V}{\sin \phi_o} \right)^2 \left[1 + \frac{3}{4} k \bar{w} \sin^2 \phi_o \right]^2 \alpha C_L (\cos \phi + \tan \gamma \sin \phi) \quad (4.32)$$

Before the above equations can be solved at each blade station, the operating lift coefficients for the front and rear propellers are found in the same manner as single-rotation propellers by using the proper values of W_1 and W_2 .

$$\alpha C_{L1} = \frac{V \bar{w} (1 + \bar{w}) \sin \phi_o}{Dx \left(1 + \frac{1}{4} \bar{w} \sin^2 \phi_o \right)} \kappa(x, \Theta) \quad (4.33)$$

$$\alpha C_{L2} = \frac{V \bar{w} (1 + \bar{w}) \sin \phi_o}{Dx \left(1 + \frac{3}{4} \bar{w} \sin^2 \phi_o \right)} \kappa(x, \Theta) \quad (4.34)$$

The section angle of attack used to find the lift coefficient from the 2D airfoil data is found from the equations:

$$\alpha_1 = \beta_1 - \phi_1 \quad (4.35)$$

$$\alpha_2 = \beta_2 - \phi_2 \quad (4.36)$$

The true wind angle for the front and rear propellers may be found using the following expressions based on the results given by Theodorsen:

$$\phi_1 = \tan^{-1} \frac{J}{\pi x} \left[1 + \frac{\bar{w}}{2} \left(1 + \frac{1}{2} k \tan^2 \phi \right) \right] \quad (4.37)$$

$$\phi_2 = \tan^{-1} \frac{J}{\pi x} \left[1 + \frac{\bar{w}}{2} \left(1 - \frac{1}{2} k \tan^2 \phi \right) \right] \quad (4.38)$$

where,

$$\phi = \tan^{-1} \frac{J}{\pi x} \left(1 + \frac{\bar{w}}{2} \right) \quad (4.39)$$

The efficiency of the propeller may be determined from the following expression:

$$\eta = \frac{C_T}{2\pi C_Q} J \quad (4.40)$$

4.3. Calculus of Variations Approach to Maximum Efficiency

The quantity which is to be minimized is the total power loss for both propellers.

$$\int_0^R \left(\frac{dP_1}{dr} + \frac{dP_2}{dr} \right) dr \quad (4.41)$$

The quantities which are held constant are the power absorbed for both propellers.

$$\int_0^R \Omega \frac{dQ_1}{dr} dr \text{ and } \int_0^R \Omega \frac{dQ_2}{dr} dr \quad (4.42)$$

The latter two are not summed, they are held constant individually, but it is not stated at this point what these constants are. The chords and hence σ , are not yet assumed to be the same front and back.

$$K' = \left(\frac{dP_1}{dr} + \frac{dP_2}{dr} \right) + k_1 \Omega \frac{dQ_1}{dr} + k_2 \frac{dQ_2}{dr} \quad (4.43)$$

Then for Euler's Equation:

$$\frac{\delta K'}{\delta \sigma} - \frac{d}{dt} \frac{\delta K'}{\delta \sigma_r} = 0 \quad (4.44)$$

Since there is no σ_r in this problem, the equation above becomes:

$$\frac{\delta K'}{\delta \sigma} = 0 \quad (4.45)$$

Since there are two σ 's in this problem, the above equation may be written separately for the front and back propellers.

$$\frac{\delta K'}{\delta \sigma_1} = 0 \quad (4.46)$$

$$\frac{\delta K'}{\delta \sigma_2} = 0 \quad (4.47)$$

Now, the sum of power losses depends on both σ_1 and σ_2 but the power absorbed by the front propeller does not depend upon σ_2 and vice versa. The two Euler Equations are:

$$\frac{\delta}{\delta \sigma_1} \left(\frac{dP_1}{dr} + \frac{dP_2}{dr} \right) + k_1 \Omega \frac{\delta}{\delta \sigma_1} \left(\frac{dQ_1}{dr} \right) = 0 \quad (4.48)$$

$$\frac{\delta}{\delta\sigma_2} \left(\frac{dP_1}{dr} + \frac{dP_2}{dr} \right) + k_2\Omega \frac{\delta}{\delta\sigma_2} \left(\frac{dQ_2}{dr} \right) = 0 \quad (4.49)$$

The above equations are two relations defining σ_1 and σ_2 as functions of r . When σ is the same front and back, the two equations become one (Q_1 & Q_2 are the same when $\sigma_1 = \sigma_2$).

The two equations thus become:

$$\frac{\delta}{\delta\sigma} \left(\frac{dP_1}{dr} + \frac{dP_2}{dr} \right) + k_2\Omega \frac{\delta}{\delta\sigma} \left(\frac{dQ}{dr} \right) = 0 \quad (4.50)$$

5. STANDARD DUAL-ROTATING PROPELLER

5.1. Introduction

A need for full-scale wind-tunnel tests for propellers was observed in the 1940s. Dual-Rotating Propellers, based on their improved efficiency and engine torque reduction over Single-Rotating ones deemed the full-scale testing of propellers necessary. Consequently, wind-tunnel tests of 10-foot eight-blade single-rotating and dual-rotating propellers were conducted by NACA at the Propeller Research Tunnel (Biermann & Gray, 1941). The propellers were mounted at the front end of a streamline body comprising of spinners for the hub portions as shown in Figure 5.1 for six-bladed propeller. The blade angles investigated varied from 20° to 65° . This Wind Tunnel Test was used as a benchmark to investigate the performance of a Dual Rotating Propeller combination and carry out a detailed CFD Analysis to gain insight into the complex aerodynamics surrounding the contra-rotating propeller combination.

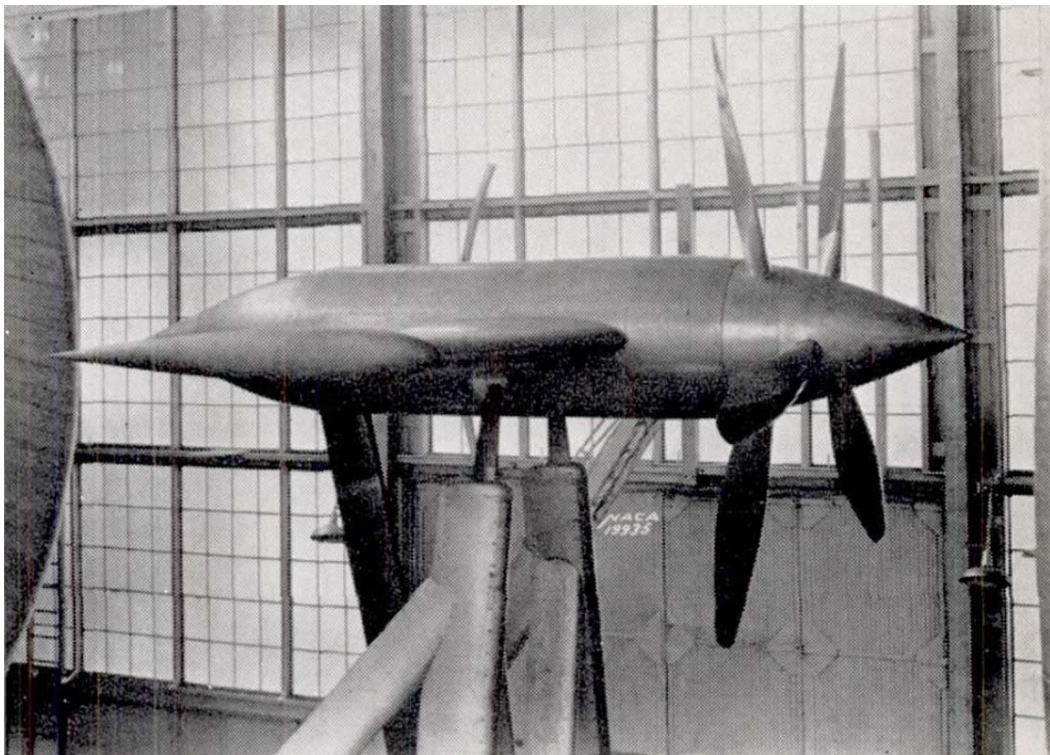


Figure 5.1. Six-blade single-rotating propeller with wing in place (Biermann & Gray, 1941).

5.2. Propeller Geometry

The propellers, namely the Hamilton Standard 3155-6 and 3156-6 propellers, incorporate the Clark Y section and are approximately 10 ft in diameter. Biermann & Gray (1941) have plotted the plan-form curves for both propellers, the spinners and the streamline body. The geometry of the blades is presented in Table 5.1, Table 5.2 and Table 5.3.

Table 5.1. Blade Angle Distribution for Hamilton Standard 3155-5 and 3156-6 Blades (Biermann & Gray, 1941)

r/R	p/D	β (Radians)	β (Degrees)
0.2	3.209	1.377	78.921
0.3	2.879	1.254	71.870
0.4	2.752	1.142	65.457
0.5	2.732	1.049	60.102
0.6	2.748	0.969	55.545
0.7	2.790	0.903	51.747
0.75	2.806	0.872	49.978
0.8	2.840	0.846	48.493
0.9	2.918	0.801	45.898

Table 5.2. Chord Distribution for Hamilton Standard 3155-5 and 3156-6 Blades (Biermann & Gray, 1941)

r/R	b/D	b (ft)	b (inches)	Section Chord, b (mm)
0.3	0.050	0.498	5.977	151.803
0.4	0.062	0.624	7.488	190.194
0.5	0.074	0.737	8.848	224.731
0.6	0.079	0.789	9.470	240.548
0.7	0.076	0.758	9.096	231.044
0.75	0.072	0.716	8.595	218.310
0.8	0.065	0.655	7.855	199.516
0.9	0.050	0.504	6.050	153.675
0.95	0.041	0.408	4.899	124.425

Table 5.3. Section Thickness Distribution for Hamilton Standard 3155-5 and 3156-6 Blades (Biermann & Gray, 1941)

r/R	h/b	h (ft)	h (inches)	Section Thickness, h (mm)
0.3	0.431	0.215	2.577	65.448
0.4	0.219	0.137	1.642	41.701
0.5	0.130	0.096	1.152	29.259
0.6	0.094	0.074	0.889	22.582
0.7	0.078	0.059	0.708	17.973
0.75	0.073	0.053	0.631	16.015
0.8	0.071	0.047	0.558	14.185
0.9	0.067	0.034	0.407	10.341
0.95	0.066	0.027	0.322	8.181

5.3. Geometric Modelling

The geometric model created in CATIA V5 and an isometric view is shown in Figure 5.2.

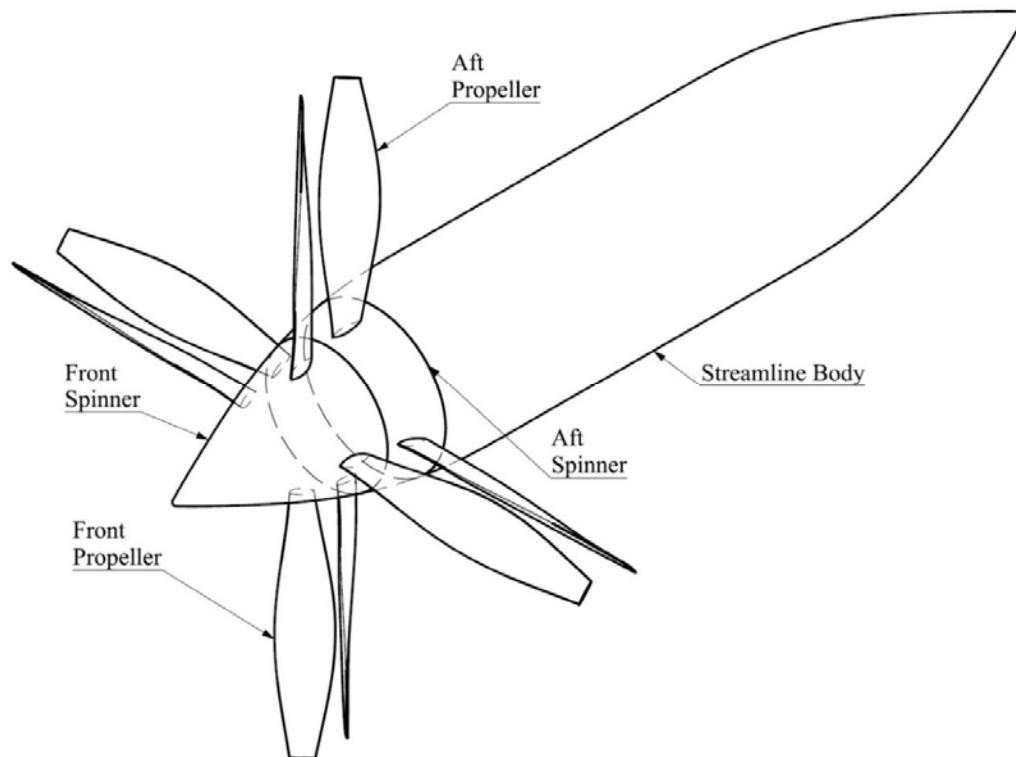


Figure 5.2. Isometric View of Eight Blade Dual-Rotating Propeller Geometric Model.

Box stations created for Hexa Meshing are shown in Figure 5.3.

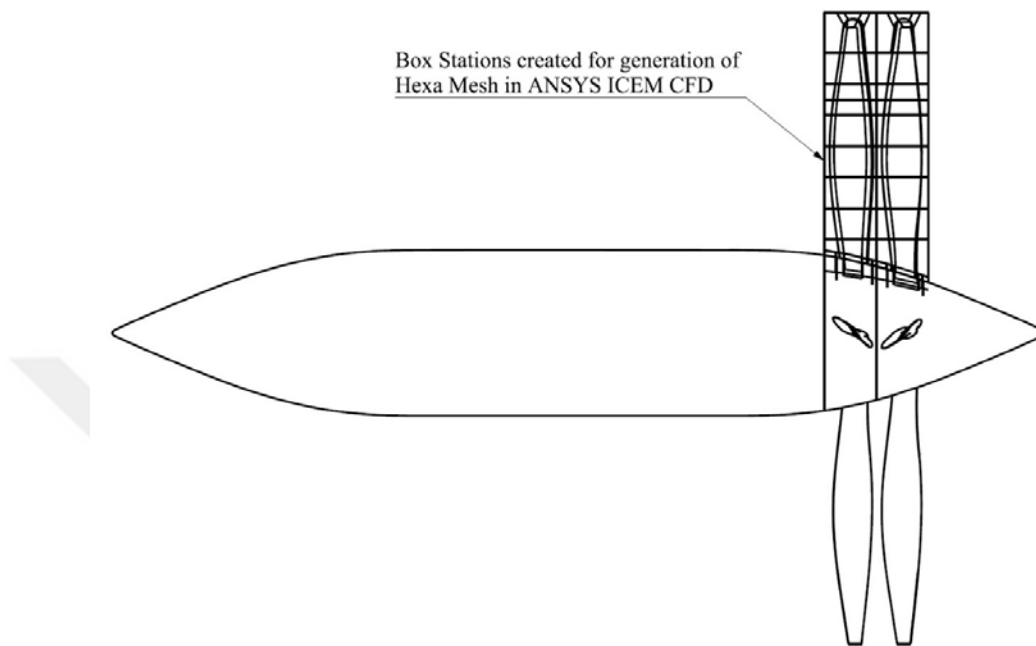


Figure 5.3. Side View comprising of station wise 'boxes' created for Hexahedral Meshing.

A section view showing the box geometry is shown in Figure 5.4.

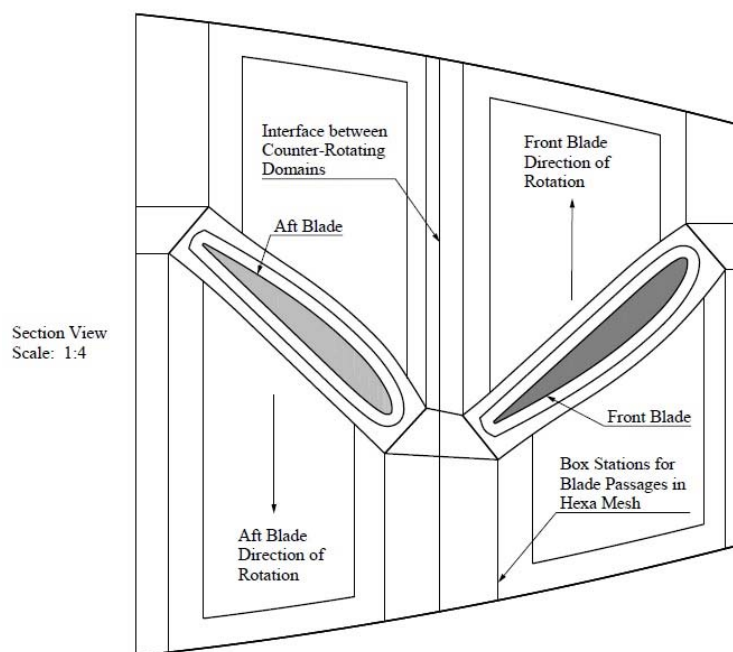


Figure 5.4. Section View of propeller blades inside the 'box geometry'.

5.4. Propeller Wind Tunnel Tests: Tunnel Description, Conditions and Results

Biermann & Gray (1941) conducted wind-tunnel tests at the Propeller Research Wind Tunnel of NACA. The tunnel was of the open-throat closed test chamber, return passage type (Weick & Wood, 1929). Air is drawn across the test chamber into the exit cone by a propeller fan. Full scale tests of eight-blade single and dual rotating propellers were conducted as an extension of the tests made on four- and six-blade dual rotating propellers. The test section measured around about 50 by 60 by 55 ft. The same dimensions were used to create a geometry and mesh to simulate the Wind-Tunnel test.

Wind speeds in the tunnel ranged from zero to 110 m.p.h. Maximum propeller speed recorded was 550 rpm which corresponds to a tip speed of 287 ft/s. In case of the dual-rotating propeller, the rear propeller blades were adjusted to provide the same torque at peak efficiency as the front propeller. For the candidate front propeller pitch at $0.75 r/R$ chosen, the difference in the aft propeller pitch was 1.3° .

The results obtained from the wind tunnel tests were non-dimensionalized into respective coefficients of thrust, power and propulsive efficiency and have been plotted in graphical form against advance ratio in Figure 5.5, Figure 5.6 and Figure 5.7.

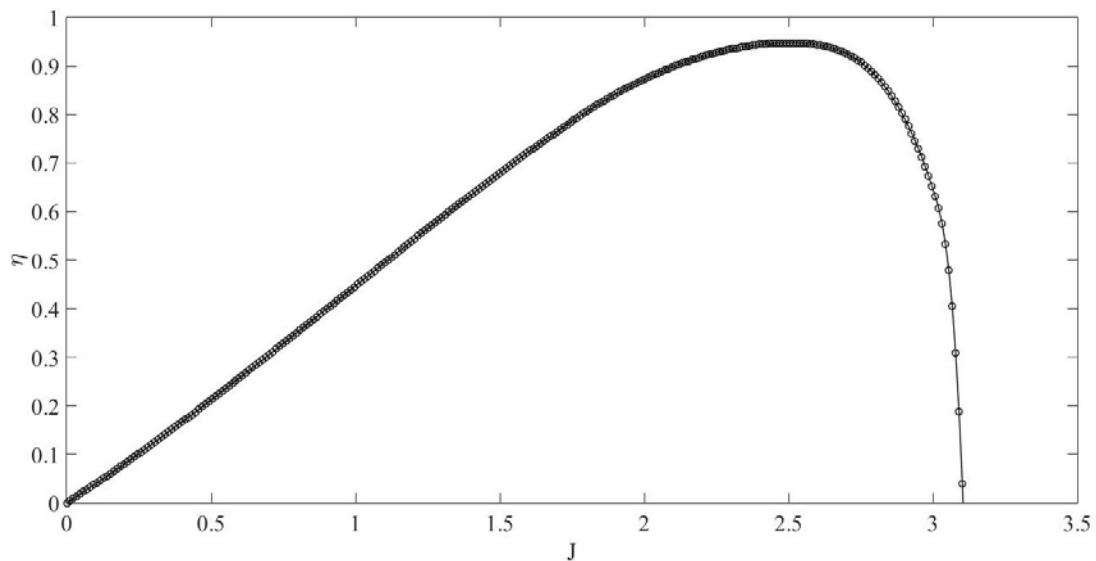


Figure 5.5. Efficiency Curves for 8-blade dual rotation (Biermann & Gray, 1941).

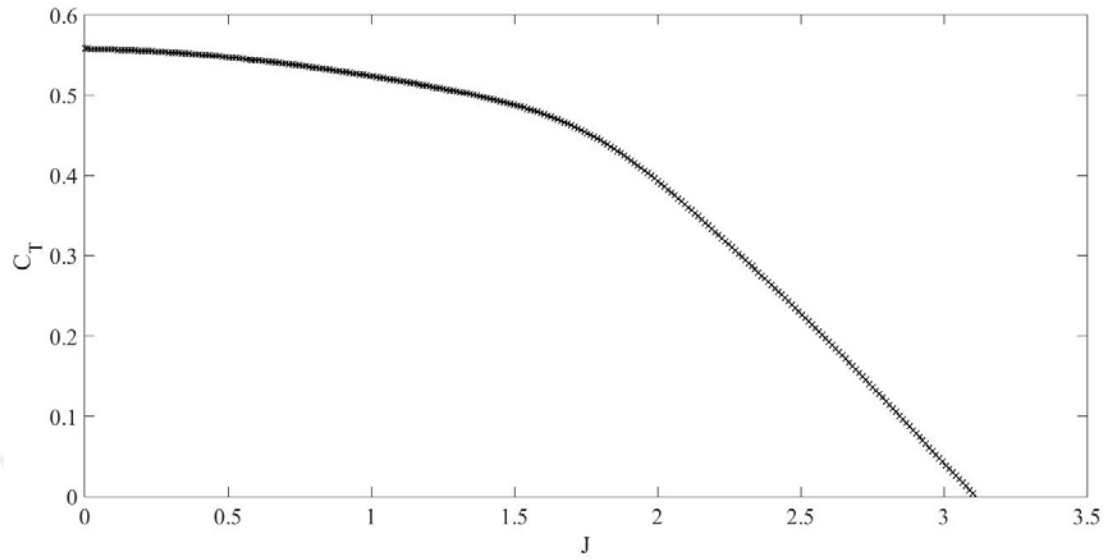


Figure 5.6. Thrust Coefficient Curves for 8-blade dual rotation (Biermann & Gray, 1941).

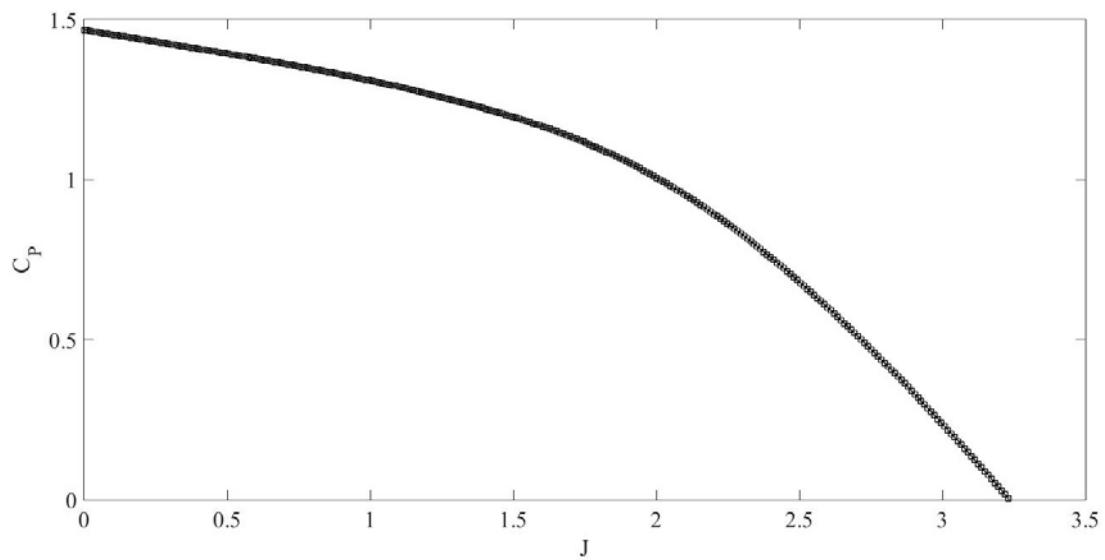


Figure 5.7. Power Coefficient Curves for 8-blade dual rotation (Biermann & Gray, 1941).

6. PROPELLER PERFORMANCE CALCULATIONS

6.1. Introduction

Naiman (1944) developed a method to calculate the performance characteristics of a dual-rotating propeller using variables from section characteristics. The results obtained from using this method are suitable as a benchmark for comparison with the wind-tunnel test results obtained by Biermann & Gray (1941) and CFD Analysis results of the dual-rotating propeller system. Lock (1941) made an attempt to replace the periodic velocity field by a steady one, the equations however are cumbersome and the current method provides a better alternative with faster computation.

6.2. Assumptions

The underlying assumption of strip-theory calculations is that the performance of a radial element is independent of other sections. The velocity distribution is non-uniform along the span of the blade. Moreover, in the dual-rotating propeller system, each propeller is operating in the non-uniform velocity field of the other propeller. The following assumptions are note-worthy:

1. The periodic velocity field may be replaced by a steady one.
2. Mean value of the induced velocity is F times the value induced at the vortex sheet.
3. Self-induced velocities may be determined in the same fashion as that for single-rotating propellers.
4. No change occurs in the axial velocity as the propellers are close together.

6.3. Expressions for Differential Thrust and Torque

From the force diagrams of the blade elements, the differential thrust and differential torque are given as:

$$dT = BXdr \quad (6.1)$$

$$dQ = BYrdr \quad (6.2)$$

Furthermore,

$$X = L \cos \phi - D \sin \phi \quad (6.3)$$

$$Y = L \sin \phi + D \cos \phi \quad (6.4)$$

The expressions for the differential thrust and torque may be stated as:

$$\frac{dC_{T1}}{dx} = \pi^3 x^3 \frac{F_1 \tan \epsilon_1 (\cot \phi_1 - \tan \gamma_1)}{(\cot \phi_1 + \tan \epsilon_1)^2} \quad (6.5)$$

$$\frac{dC_{T2}}{dx} = \pi^3 x^3 \frac{F_2 \tan \epsilon_2 (\cot \phi_2 - \tan \gamma_2)}{[(\cot \phi_2 + \tan \epsilon_2) / (1 + 2A)]^2} \quad (6.6)$$

$$\frac{dC_{Q1}}{dx} = \frac{\pi^3 x^4}{2} \frac{F_1 \tan \epsilon_1 (1 + \cot \phi_1 \tan \gamma_1)}{(\cot \phi_1 + \tan \epsilon_1)^2} \quad (6.7)$$

$$\frac{dC_{Q2}}{dx} = \frac{\pi^3 x^4}{2} \frac{F_2 \tan \epsilon_2 (1 + \cot \phi_2 \tan \gamma_2)}{[(\cot \phi_2 + \tan \epsilon_2) / (1 + 2A)]^2} \quad (6.8)$$

6.4. Application of Method

The method developed by Naiman (1944) has been applied to determine the section-wise performance characteristics of the eight-blade dual-rotating propeller. Three sheets are necessary for the complete calculation.

- Sheet 1 is used to calculate the inflow angles for both blades, the lift coefficients and the advance ratio.

- Sheet 2 is a trial sheet necessary for the determination of the lift coefficient of the aft propeller.
- Sheet 3 is used in the end for determination of the thrust and torque coefficients for both propellers.
- The results from the calculations of the sheets may be referred to in the Appendix-A for Blade Stations $x = 0.3$, $x = 0.45$, $x = 0.6$, $x = 0.7$, $x = 0.8$, $x = 0.9$ and $x = 0.95$

6.4.1. Sheet 1 calculation

The method for tabulation in Sheet 1 is briefly described as follows:

1. Select arbitrary values of C_L and determine the value of α using Figure 6.1.

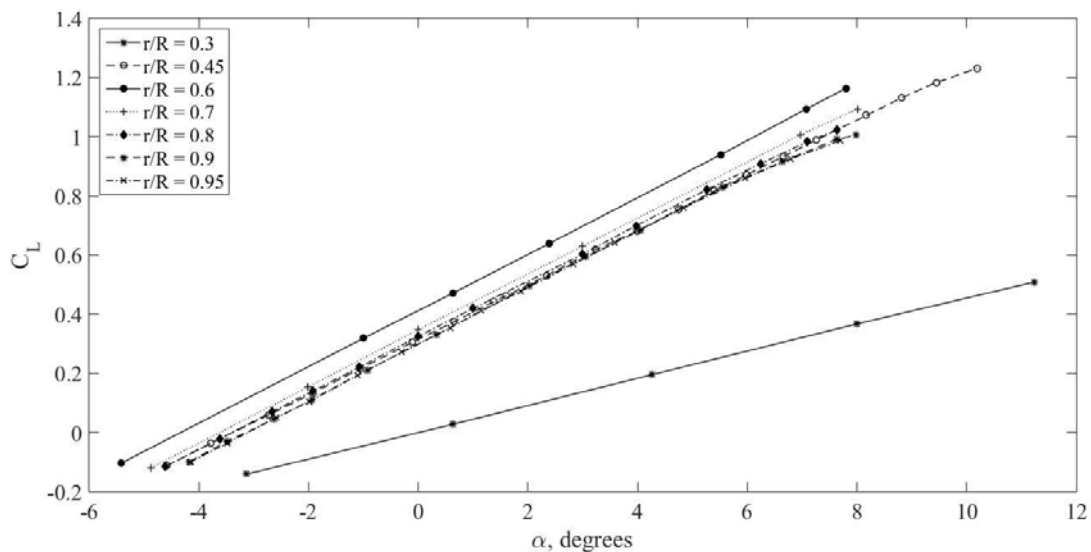


Figure 6.1. Lift Curves of the Clark-Y Sections with infinite aspect ratio (Crigler & Talkin, 1942).

2. Determine the value of F from the chart obtained from Lock & Yeatman (1934).
3. Determine the values of $\tan \epsilon_1$, A and G proceed to Sheet 2.

6.4.2. Sheet 2 calculation

The method for tabulation of Sheet 2 is briefly described as follows:

1. The value of C_L at which the corresponding station of the aft propeller rotates must now be determined based on the assumed value of C_L of the front propeller.
2. Two values of $\theta_2 - \phi_2$ are determined based on the assumed values from the front propeller.
3. The assumed values are plotted directly on the Lift Curve of Clark-Y section and an intersection point is obtained between the line connecting these two points and the lift curve.
4. F is determined in a similar way as for the front propeller using Figure 6.2.
5. Sheet 2 is completed and the remaining portion of Sheet 1 is calculated until a value of advance ratio, J is achieved.

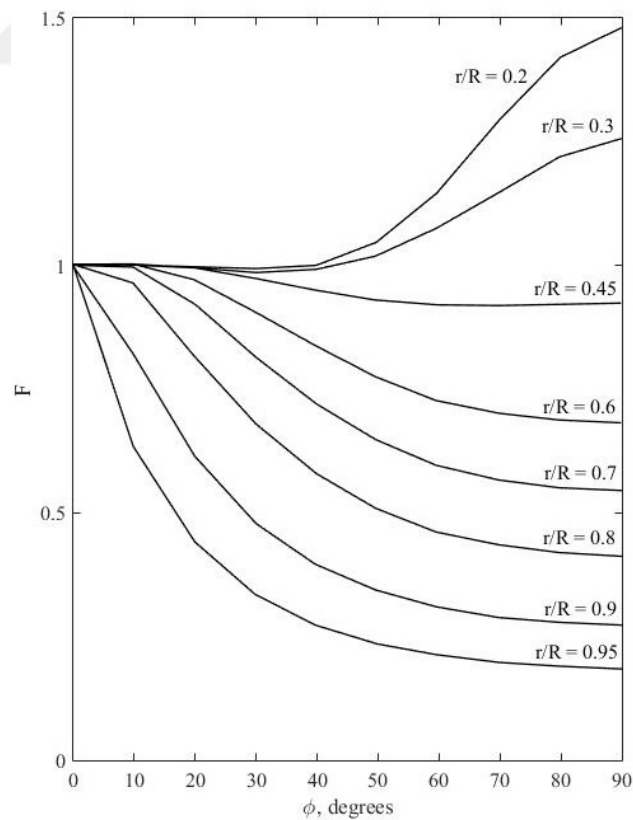


Figure 6.2. F-Curves for a Four-Blade Propeller (Crigler & Talkin, 1942)

6.4.3. Sheet 3 calculation

All necessary variables involved in the calculation of differential thrust and torque have been determined in Sheets 1 and 2. The lift-drag ratio of the Clark-Y section is used to determine the value of γ using Figure 6.3. Tabulated results for the Sheets 1,2 and 3 are listed in the Appendix-A They are used to compute the thrust and torque for the blades.

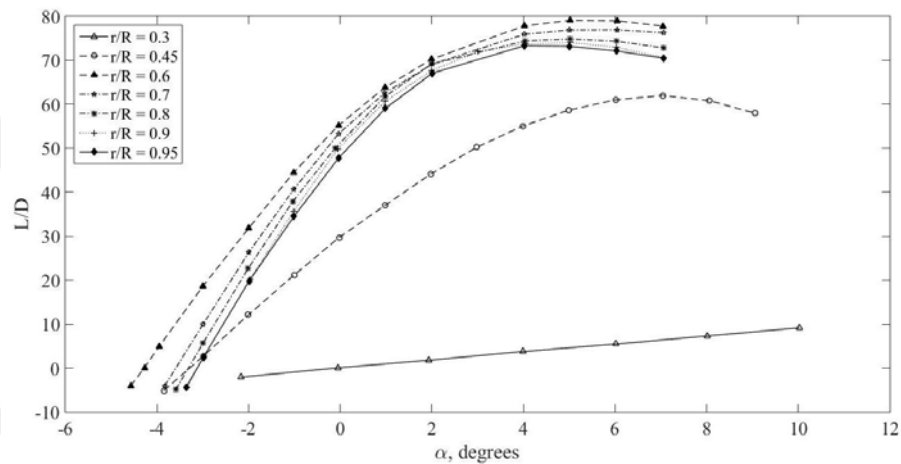


Figure 6.3. Lift Drag Curves of the Clark-Y Sections with infinite aspect ratio (Crigler & Talkin, 1942)

Figure 6.4 shows the variation of the power absorbed by the fore and aft propellers as a function of the advance ratio.

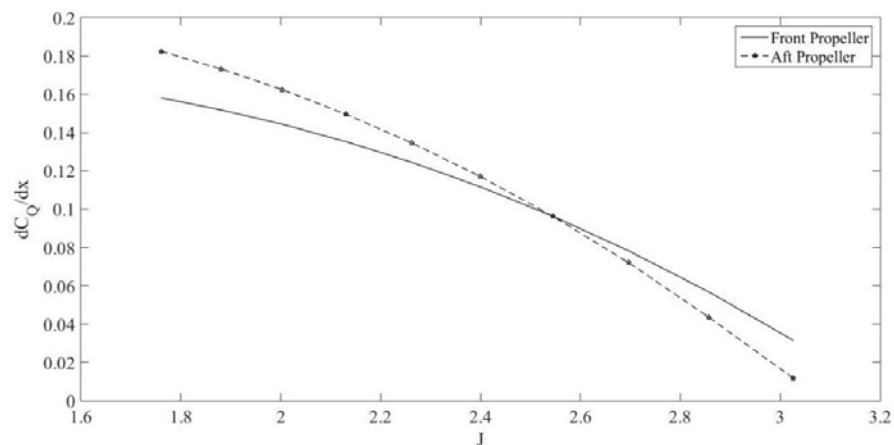


Figure 6.4. Individual differential-torque curves for eight-blade dual-rotating propeller at $x = 0.7$, $\theta_1 = 50^\circ$, $\theta_2 = 48.7^\circ$.

7. MESHING AND CFD ANALYSIS

7.1. Introduction

The performance calculations of Naiman (1944) provide a computationally inexpensive alternative to measuring the performance of a dual-rotation propeller arrangement however, to closely investigate the complex flow around contra-rotating blades, a CFD analysis is required. This analysis provides a benchmark for the evaluation of propeller performance as well as a foundation upon which further design modifications on the propeller may be carried out or the installed effects on the aircraft or the wing may be implemented (Stokkermans et al., 2019).

The flow field has been modelled by RANS (Reynolds Averaged Navier-Stokes) equations closed by one of the turbulence models was employed. Numerical simulations have been performed in ANSYS Fluent 14.0 where governing equations for incompressible, viscous fluid are solved by the finite-volume method.

7.2. Domain Description

An attempt has been made to simulate the experimental test environment as closely as possible. The full geometry of the rotor blades and streamline body has been modelled. Although test results for the wing attached to the streamline body were also available, for this benchmark investigation, the model without the wing was deemed suitable.

Blade geometry corresponds to the original blade in the span of 20–100%, root segment has been slightly cut to avoid a sharp edge. The sharp edge of the streamline body has not been modified, although it has presented a substantial meshing challenge, however, the original geometry of the streamline body has been used for analysis. It was kept in mind that although the streamline body has little to no contribution to the overall thrust and torque, any modification to the shape may influence the incoming flow to the front propeller. Weick & Wood (1929) have presented the dimensions of the Propeller Research Tunnel of NACA.

Both propellers have been enclosed in cylindrical domains whereas the stationary domain is rectangular. Since the hub of the front propeller rotates with the blades, it has also been included as part of the rotary domain as shown in Figure 7.1.

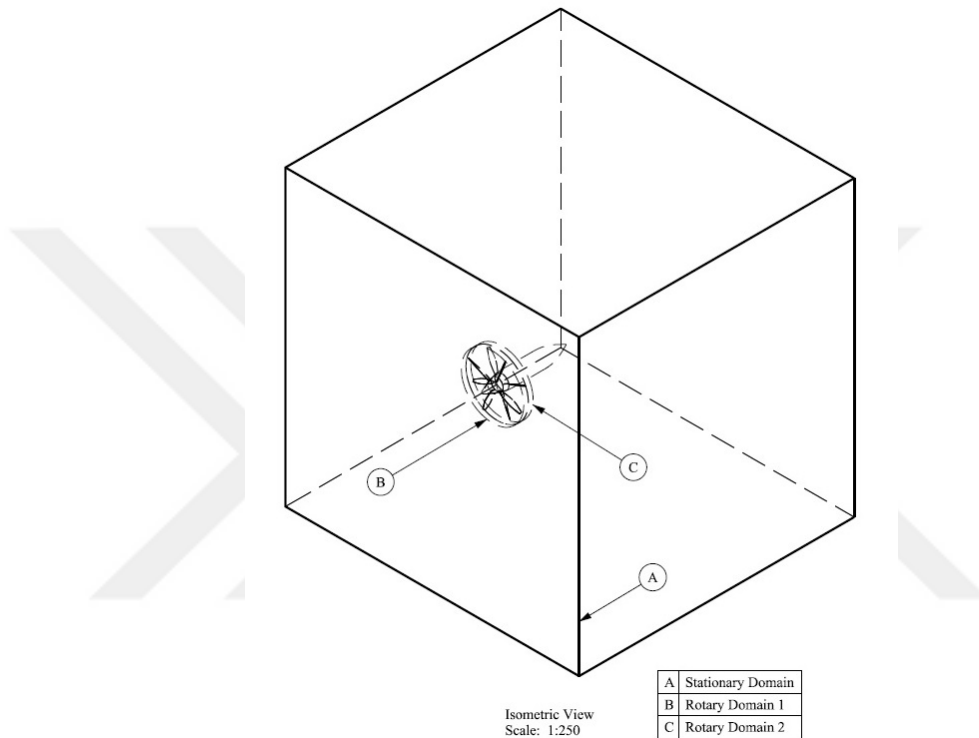


Figure 7.1. Rotary and Stationary Domains for CFD Analysis.

7.3. Grid Generation

Grid generation was one of the most challenging steps for the thesis. It was decided earlier on that a hexahedral structured mesh be made for this analysis. Although not a requirement, some of the reasons for this decision are that structured grids are identified by regular connectivity. They provide better and accurate results. Less cell (element) count saves CPU and RAM time. Since the lack of favorable computational resource was taken into account from the onset, it was deemed logical to create a hexahedral mesh for this problem.

The geometry of the blades presented a considerable challenge while meshing. The fact that the pair of contra-rotating blades are in close proximity to each other presented a

lot of problems as well. Additionally, it was intended to create a mesh that would be suitable for all steady and unsteady analyses of the blades.

The mesh was created in ANSYS ICEM CFD 14.0. Although the software itself presents a steep learning curve, however, this has been overcome after a fair amount of hit and miss. The mesh was constantly modified, based on the solution strategy being adopted. Some challenges faced were as follows:

1. The conical section of the streamline body presented a challenge. Different blocking strategies were adopted that finally resulted in good quality elements around the cone.
2. Several blocking strategies were implemented to get a good quality mesh. The finalized blocking strategy is shown in Figure 7.2. Particular consideration was given to all the quality metrics such as aspect ratio, volume change, skewness, determinant etc.

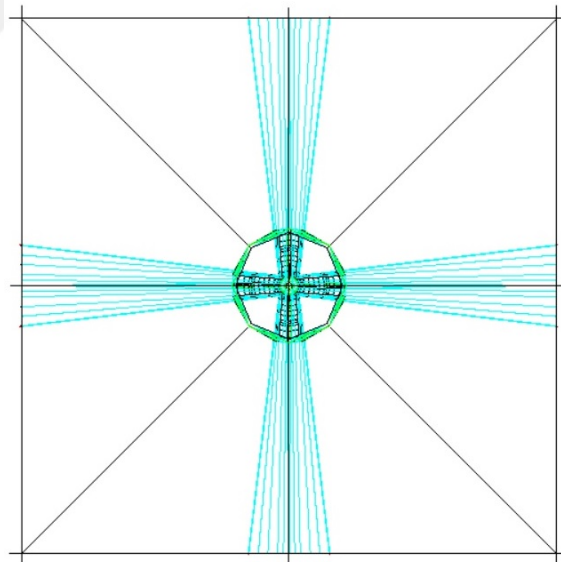


Figure 7.2. Blocking strategy for Hexa Meshing in ICEM CFD.

3. The proximity between the blades was another geometric constraint. An attempt was made to create a stationary fluid domain in between the blades and this resulted in bad, high aspect ratio elements in the domain. This approach was not adopted.

4. Creation of O-Grids around the blades for solving the boundary layer was also difficult due to the twist distribution of the blade. To get good quality elements, the geometry for these blocks was modelled separately.
5. Creating an O-Grid for the rotational domain was necessary as it would otherwise lead to bad quality elements at the circumference.

The isometric view of the surface mesh is shown in Figure 7.3 and a sectional view of the mesh including the rotary and stationary domains is shown in Figure 7.4.

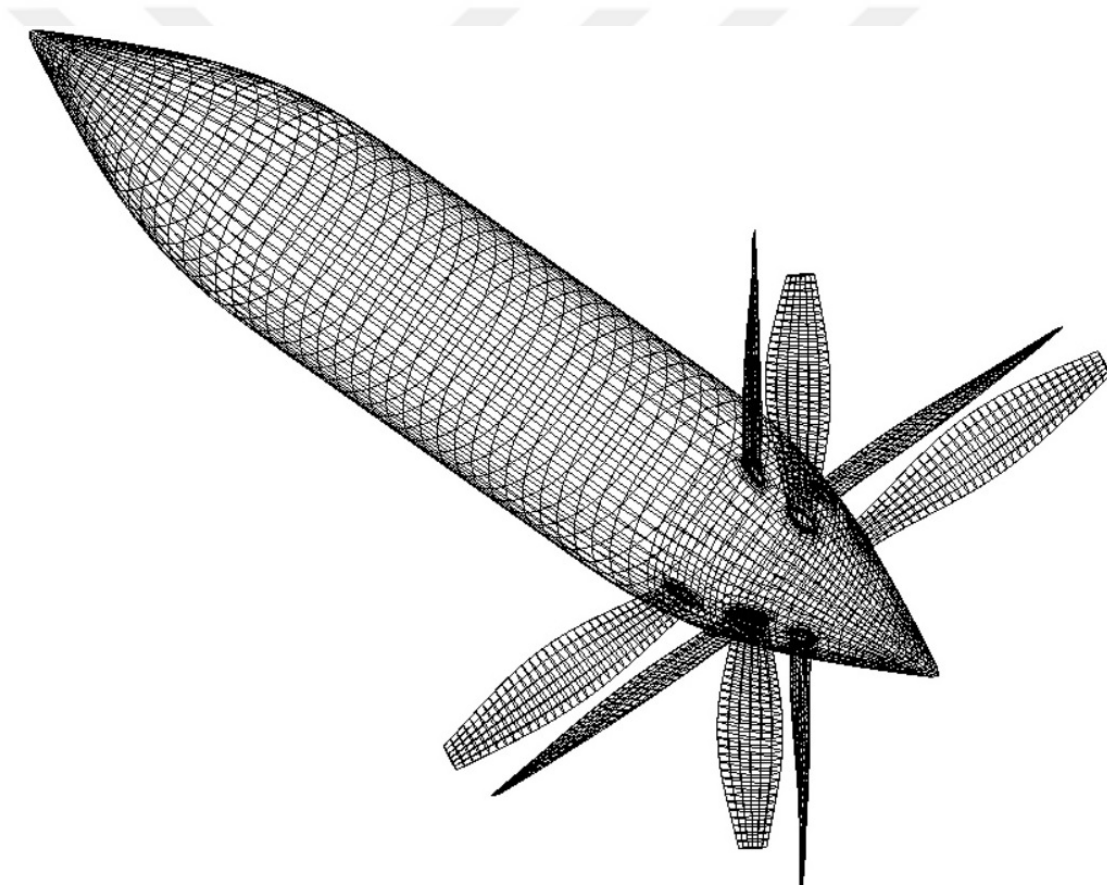


Figure 7.3. Isometric View of Mesh on Blade and Streamline Body Surfaces.

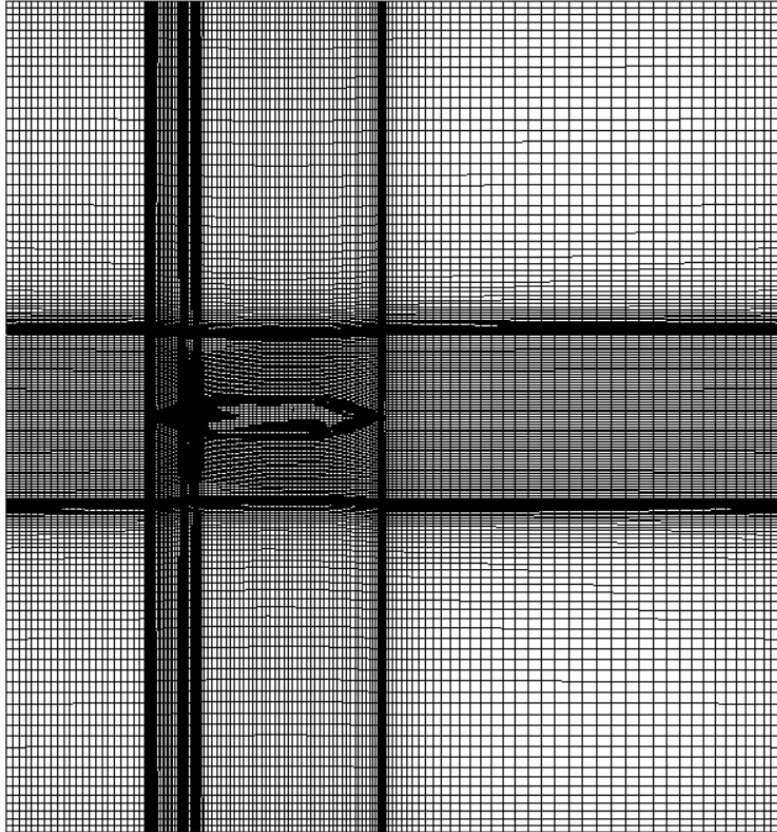


Figure 7.4. Sectional View of Mesh showing entire domain.

7.4. Boundary Conditions and Methodology

7.4.1. Boundary conditions

A grid convergence study has been done before the adoption of the computational mesh. The mesh size is around 3.70 Million cells. Steady or Unsteady RANS equations were closed using the $k-\epsilon$ turbulence model. It is pertinent to note here that the equations for the propeller problem may also have been closed by using a $k-\omega$ SST turbulence model which is a combination of $k-\omega$ near the walls and $k-\epsilon$ in the outer layer. Fluid, air, was considered as an incompressible fluid of constant dynamic viscosity. No-slip boundary condition has been applied on the blade surfaces and streamline body, specified shear has been specified on the Wind Tunnel walls.

The domain comprises of two contra-rotating cell zones adjacent to each other as shown in Figure 7.5. Three interfaces have been created for the transformation of vector quantities at the interfaces. There are two approaches available for the transformation of vector quantities namely the mixing-plane and the sliding mesh (Huo et al., 2019). Since the flow at the rotor-rotor interface zones is not radially uniform, the sliding mesh method is generally used.

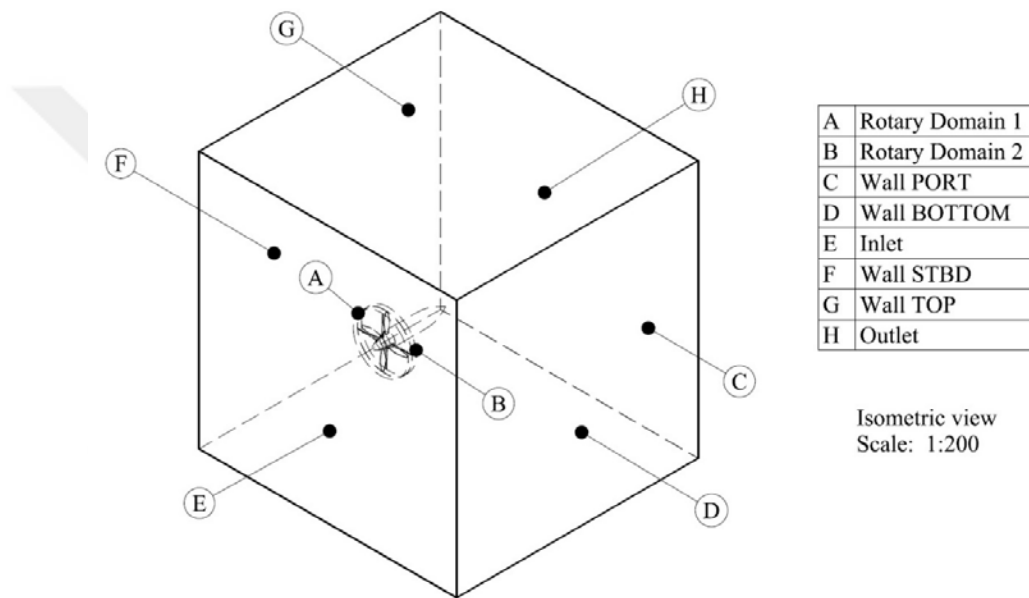


Figure 7.5. Boundary Conditions

7.4.2. Methodology of 3D computation

Initially the flow around the blades was modelled as a steady flow using the Multiple Reference Frames approach in ANSYS Fluent. This was necessary to serve as an initial condition for the unsteady transient analysis.

Real-time load distributions on the blades were of interest as an insight into the effect on interference velocities while the blades rotate and the corresponding effect on the load distributions was needed. The periodic unsteadiness in the thrust and torque produced by both the rotors was particularly of interest as the experimental work presented results for a time-averaged mean value of the thrust and torque of the blades. A final time-periodic

solution requires the data to be time-averaged during one period for the steady performance analysis of the system. Figure 7.6 shows the angular displacement of the blades.

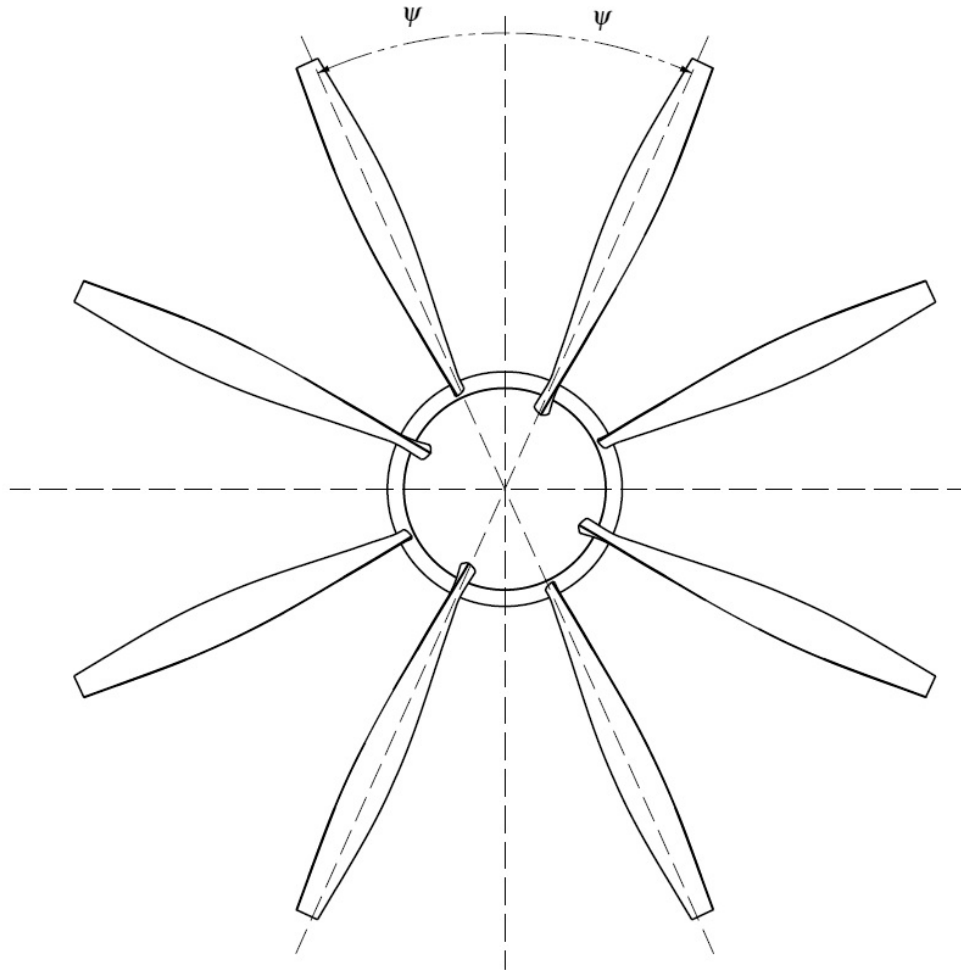


Figure 7.6. Angle of rotation of the Contra-Rotating propeller blades, ψ° .

7.4.3. Determination of boundary conditions

Due to the fact that the results from the Wind Tunnel experiments carried out by Biermann & Gray (1941) have been presented in a non-dimensional format, the investigation of the appropriate boundary conditions presented itself as a more involved task. A series of runs were conducted for inviscid and viscous flows with various inlet velocities and propeller rotation speeds keeping J constant. It was concluded that the configuration with an inlet velocity of 110 m.p.h. represents the closest scenario at which the tests were conducted and

gives a closer match to the calculated thrust and power available from the results. A brief summary of the inviscid runs with varying advance ratios is tabulated in Table 7.1.

Table 7.1. CFD Cases run for determination of Boundary Conditions.

	J	Thrust_1 (N)	Thrust_2 (N)	Torque_1 (Nm)	Torque_2 (Nm)
Case 1	2.57	261.21	352.33	520	-563
Case 2	2.58	265.68	330.48	513	-549
Case 3	2.59	248.17	331	505	-536
Case 4	2.60	241.71	320.21	498	-522
Case 5	2.61	235.33	310.07	490	-509
Case 6	2.70	181.62	224.21	427	-398

7.5. The SIMPLE Algorithm

Pressure based SIMPLE scheme has been employed for solving the flow equations for the analysis. Barton (1998) has carried out an investigation on various pressure-based algorithms based on the SIMPLE and PISO algorithms. Accuracy, robustness, turbulence modelling, computational cost, convergence and accuracy are some of the factors to be considered when selecting a method. Based on severe computational limitations, the SIMPLE Method was selected and a brief literature review is presented here.

7.5.1. Introduction

The SIMPLE algorithm has been used to solve the incompressible Navier-Stokes Equations. It is one method used to solve the Navier-Stokes Equations numerically and is quite popular in CFD. The SIMPLE algorithm is computationally much quicker and allows more iterations, faster than PISO/Coupled Pressure-Velocity coupling methods. The continuity and Navier-Stokes Equations are:

$$\nabla \cdot \mathbf{U} = 0 \quad (7.1)$$

$$\mathbf{U} \cdot \nabla \mathbf{U} - \nabla \cdot (\nu \cdot \nabla \mathbf{U}) = -\nabla p \quad (7.2)$$

It can be readily seen that there are four equations and four unknowns (U_x , U_y , U_z and p). p is the kinematic pressure and ν is the kinematic viscosity. The computed velocity fields from the momentum equations must satisfy the continuity condition. The convection terms in the momentum equation are non-linear. This is what makes solving the equations difficult. An equation of state may not be available to solve for pressure.

7.5.2. Mathematical formulation

The working principle of the SIMPLE algorithm is the derivation of an equation of pressure from the momentum and continuity equations followed by the derivation of a corrector for the velocity field so that it satisfies the continuity equation. In general matrix form, the Momentum Equations can be written as:

$$MU = -\nabla p \quad (7.3)$$

M is a matrix of coefficients that are calculated by discretizing the terms in the equation. These coefficients are all known. As an example, consider the x-component of the Momentum Equation:

$$\begin{pmatrix} M_{1,1} & M_{1,2} & \cdots & M_{1,n} \\ M_{2,1} & M_{2,2} & \cdots & M_{2,n} \\ \vdots & \vdots & \ddots & \vdots \\ M_{n,1} & M_{n,2} & \cdots & M_{n,n} \end{pmatrix} \begin{pmatrix} U_1 \\ U_2 \\ \vdots \\ U_n \end{pmatrix} = \begin{pmatrix} (\delta p / \delta x)_1 \\ (\delta p / \delta x)_2 \\ \vdots \\ (\delta p / \delta x)_n \end{pmatrix} AU - H = -\nabla p \quad (7.4)$$

In the above semi-discretized equations, we have one equation for each cell centroid in our mesh. A inverted becomes:

$$A^{-1} = \begin{pmatrix} 1/A_{1,1} & 0 & \cdots & 0 \\ 0 & 1/A_{2,2} & \cdots & 0 \\ \vdots & \vdots & \ddots & \vdots \\ 0 & 0 & \cdots & 1/A_{n,n} \end{pmatrix} \quad (7.5)$$

The matrix H is evaluated explicitly from the off-diagonal terms and the velocity from the previous iteration. Hence, it is known:

$$H = AU - MU \quad (7.6)$$

We now have the decomposed form of the Momentum Equations as:

$$AU - H = -\nabla p \quad (7.7)$$

Rearranging the Momentum Equation in terms of velocity, we get:

$$U = A^{-1}H - A^{-1}\nabla p \quad (7.8)$$

Substituting into the Continuity Equation, we get:

$$\nabla \cdot [A^{-1}H - A^{-1}\nabla p] = 0 \quad (7.9)$$

Now we have a Poisson Equation for pressure:

$$\nabla \cdot (A^{-1}\nabla p) = \nabla \cdot (A^{-1}H) \quad (7.10)$$

We now have four equations and four unknowns. The solution method of the SIMPLE Algorithm is as follows:

1. Solve the velocity field from the semi-discretized form of the Momentum Equation:

$$MU = -\nabla p \quad (7.11)$$

2. Solve the Poisson Equation for the pressure field:

$$\nabla \cdot (A^{-1}\nabla p) = \nabla \cdot (A^{-1}H) \quad (7.12)$$

3. Use the pressure field to correct the velocity field so that it satisfies the Continuity Equation:

$$\mathbf{U} = A^{-1}H - A^{-1}\nabla p \quad (7.13)$$

4. The energy (E), turbulence scalar (k , ϵ , ω) and species transport equations are solved within the loop after the volume flux corrector.
5. The velocity field does not satisfy the Momentum Equation, repeat the cycle.

7.6. Numerical Setting

Pressure-based SIMPLE scheme is used for solving the flow equations. Gradients are obtained by the least squares cell-based method. Spatial discretization is of the second order. For the unsteady simulations of the blades, temporal discretization is of the first order with the time-step corresponding to a $1/360^\circ$ of the rotation period. Due to the extreme lack of computational resources, the residuals have been relaxed to the order of $1.0E-04$ and the blade has been rotated using the Sliding Mesh Method for two complete revolutions, with every time step corresponding to a rotation of 1° . Regular change in the periodic quantities like residuals and force was also monitored as shown in Figure 7.7 Figure 7.8 and Figure 7.9.

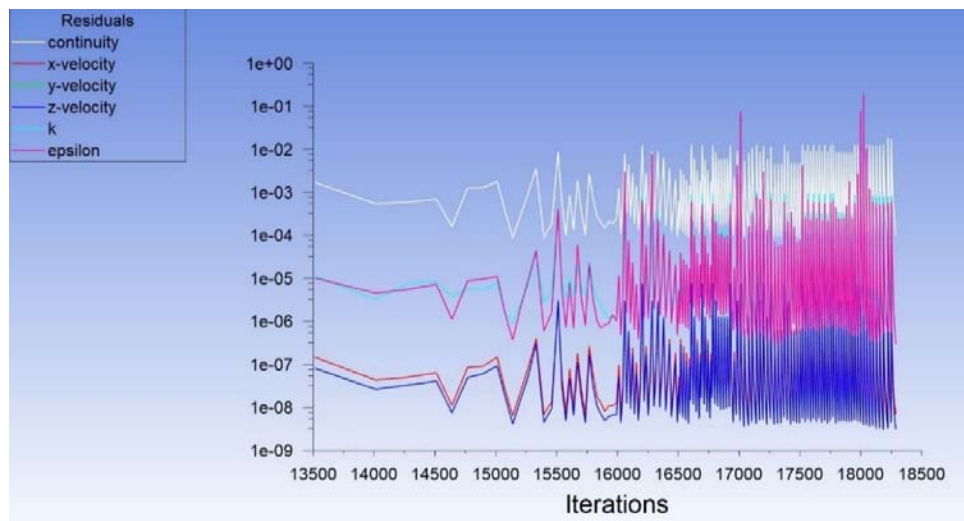


Figure 7.7. Plot of Scaled Residuals, $\psi = 720^\circ$.

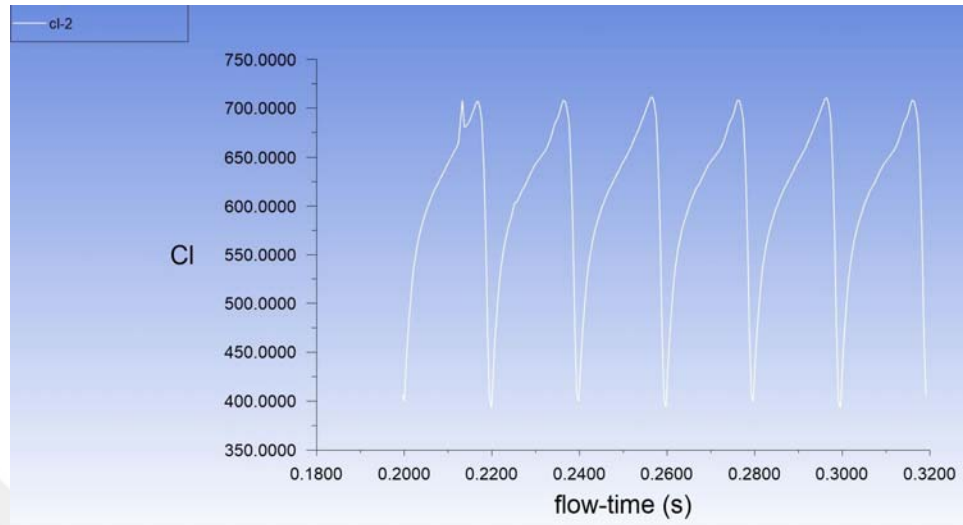


Figure 7.8. Plot of Lift Coefficient Monitor at Front Rotor at $\psi = 720^\circ$.

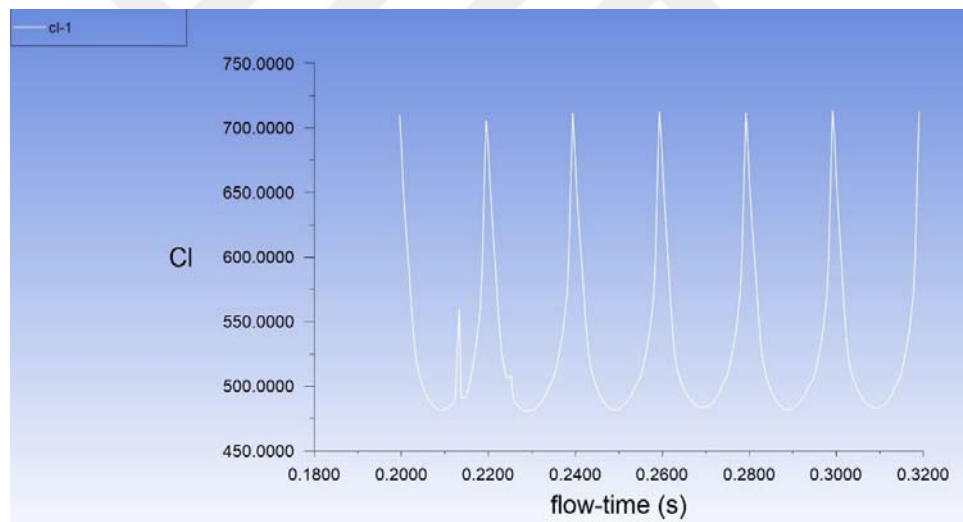


Figure 7.9. Plot of Lift Coefficient Monitor at Aft Rotor at $\psi = 720^\circ$.

7.7. Run-Time and Limitations

The simulations were run on a personal laptop with a quad-core processor, 8 GB RAM. The approximate run-time for two complete revolutions of the blade was 5 days (6 time-steps/hour). Non-availability of computational resources was a major hurdle in the completion of this thesis.

8. RESULTS AND DISCUSSION

The periodic variation of thrust for the front and aft propeller has been recorded using a macro in ANSYS Fluent at every time step and is plotted for one quadrant of the revolution in Figure 8.1 and Figure 8.2.

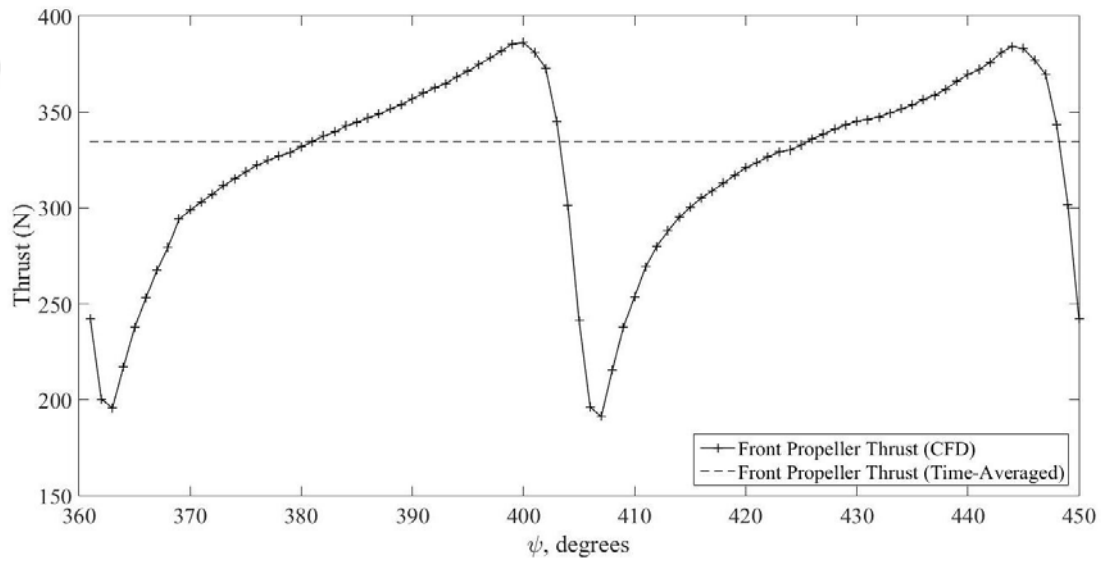


Figure 8.1. Periodic Variation of Front Propeller Thrust

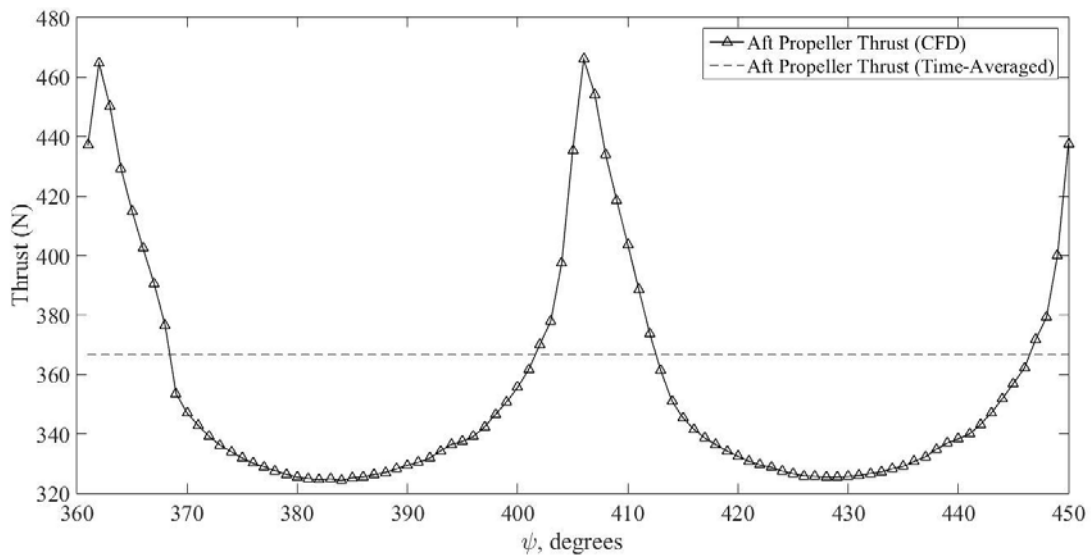


Figure 8.2. Periodic Variation of Aft Propeller Thrust

It can be readily deduced from the above plots that the thrust produced by the front propeller is most affected at periodic locations where the blades coincide with each other. Conversely, the opposite may be stated for the aft propeller and this may be attributed to the wake interaction from the front blade. The computed overall thrust of the propellers is underestimated; however, it is still in reasonable agreement with the experimental results. The sectional variation of Thrust and Torque on the blade is presented in Figure 8.3 and Figure 8.4.

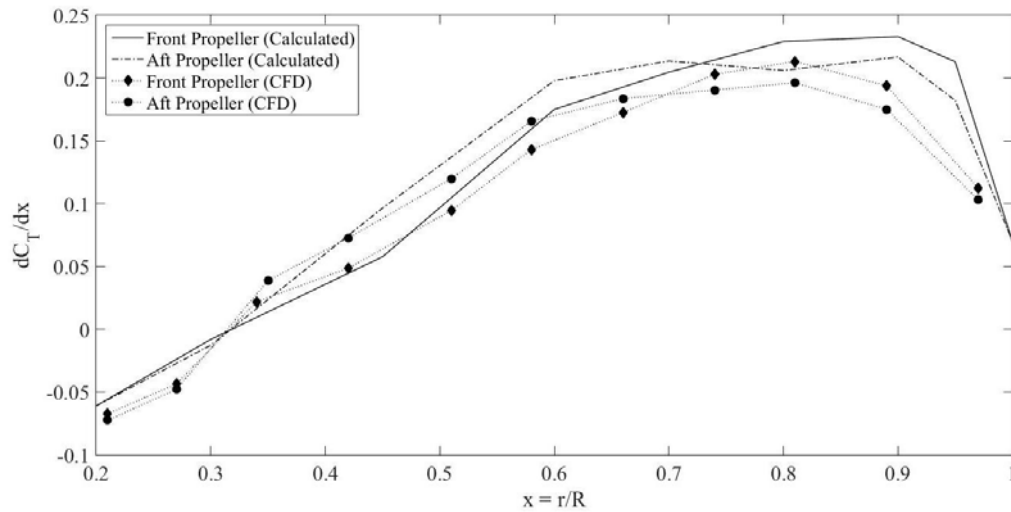


Figure 8.3. Differential Thrust Distribution at $J = 2.57$, $\beta_1 = 50^\circ$, $\beta_2 = 48.7^\circ$.

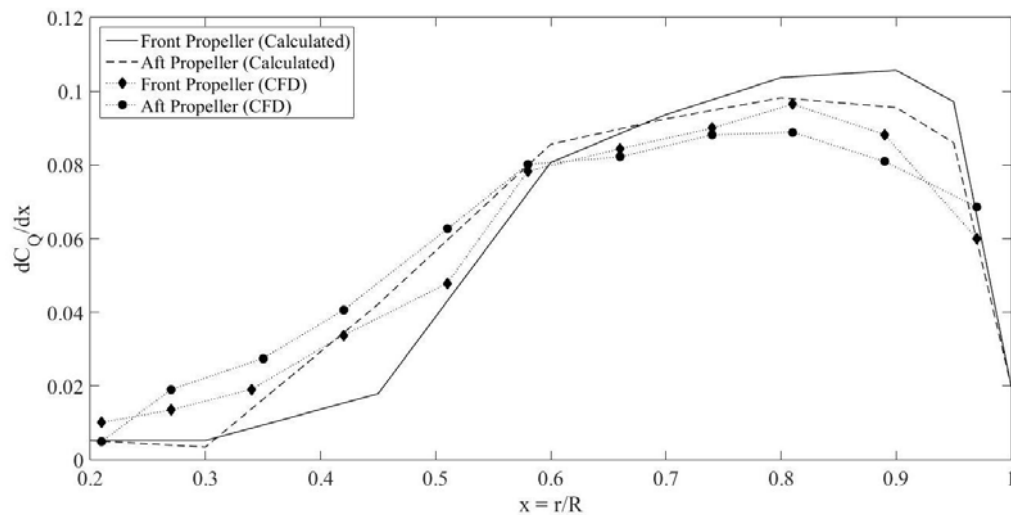


Figure 8.4. Differential Torque Distribution at $J = 2.57$, $\beta_1 = 50^\circ$, $\beta_2 = 48.7^\circ$.

Looking at the trends of sectional thrust and torque distribution, it may be concluded that although the trend is captured, however, the overall thrust and torque is underestimated. The maximum thrust and torque contribution by the outboard sections of the blade is captured by the calculated and CFD results. The torque distribution and the overall torque is in closer agreement as compared to the thrust distribution and overall thrust, however at $J = 2.57$, the CFD results indicate the aft propeller producing more thrust than the front propeller which is not the case in the Wind Tunnel Test.

A summary of the experimental, calculated and CFD results is presented in Table 8.1. Based on the numerical settings used in Fluent, the CFD results lie in agreement with the experimental results.

Table 8.1. Comparison of Experimental, Calculated and CFD Results at $J = 2.57$, $\psi = 720^\circ$.

	Experimental	Calculated	CFD
C_{TF}	*	0.0998	0.084
C_{TA}	*	0.1037	0.087
C_T	0.2	0.2035	0.171
Thrust (Front), N	*	409.151	344.376
Thrust (Aft), N	*	425.140	356.675
Thrust (Net), N	819.9	834.29201	701.051
C_{QF}	0.0505	0.0467	0.045
C_{QA}	0.044	0.0488	0.0467
C_Q	0.097	0.0955	0.0917
Torque (Front), Nm	631	583.559	562.316
Torque (Aft), Nm	552	609.801	583.559
Thrust (Total), Nm	1223	1193.361	1145.876
C_{PF}	0.32	0.295	0.285
C_{PA}	0.28	0.309	0.296
C_P	0.6	0.604	0.581
Power (Front), kW	24.9	23.016	22.178
Power (Aft), kW	21.8	24.051	23.016
Power (Total), kW	48.2	47.066	45.193
Efficiency	85.7	86.5	75.7

Velocity variation along the span of the blades gives rise to a pressure gradient on the blade surfaces. This difference between the pressure and suction surfaces generates a tip vortex. While the tip vortex remains a source of aerodynamic loss, it is also one of the sources of aerodynamic noise. A visual of the flow slipstream is shown in Figure 8.5. As can be clearly seen, the tip vortices and wake structure emanating from the front propeller is cut by the contra-rotating aft propeller wake and tip vortices. This gives rise to the net-structured woven vortex structure as can be seen in Figure 8.5.

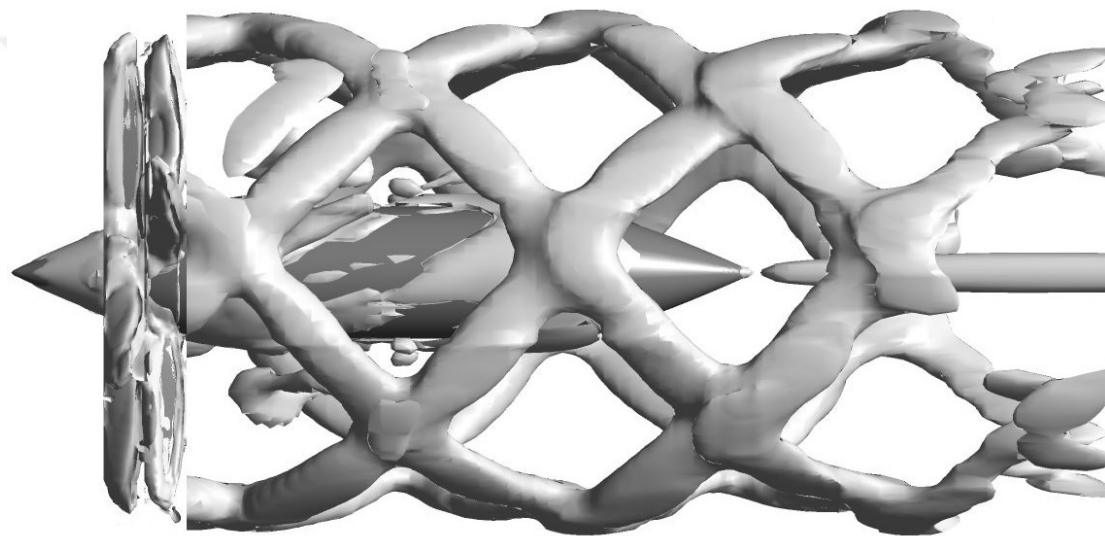


Figure 8.5. Vortex Core Region using the Lambda-2 Criterion, $\psi = 720^\circ$.

A detailed understanding of various turbulence models and their treatment of boundary layers and flow separation is paramount in analyzing the performance of the dual-rotating propeller system as wall shear stresses, surface pressures and pressure gradients are adequately determined. In CFD practice, it is recommended to either resolve the viscous sub-layer by creating a mesh with $y^+ \sim 1$ or to use the wall function approach by having the first element in the log region ($y^+ > 30$) and avoid having a y^+ between those values. Resolution of the viscous sub-layer a value of $y^+ \sim 1$ is required and this requires significant more mesh elements and computational time. Although, a good quality mesh with an estimate of first cell height for $y^+ \sim 1$ was created, however due to the unavailability of computational resources to run a $y^+ \sim 1$ for this simulation, Realizable $k-\epsilon$ model with scalable wall functions has been used in the numerical setup.

Two-dimensional turbulent boundary layer velocity profile can be seen in Figure 8.6 and the y^+ contours obtained at the blade surfaces are shown in Figure 8.7.

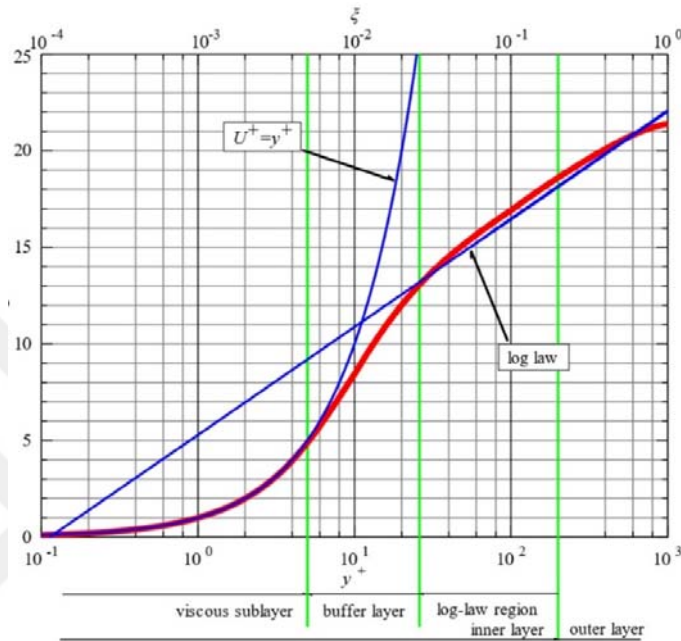


Figure 8.6. Two-dimensional turbulent boundary layer velocity profile showing various layers (ANSYS, 2006).

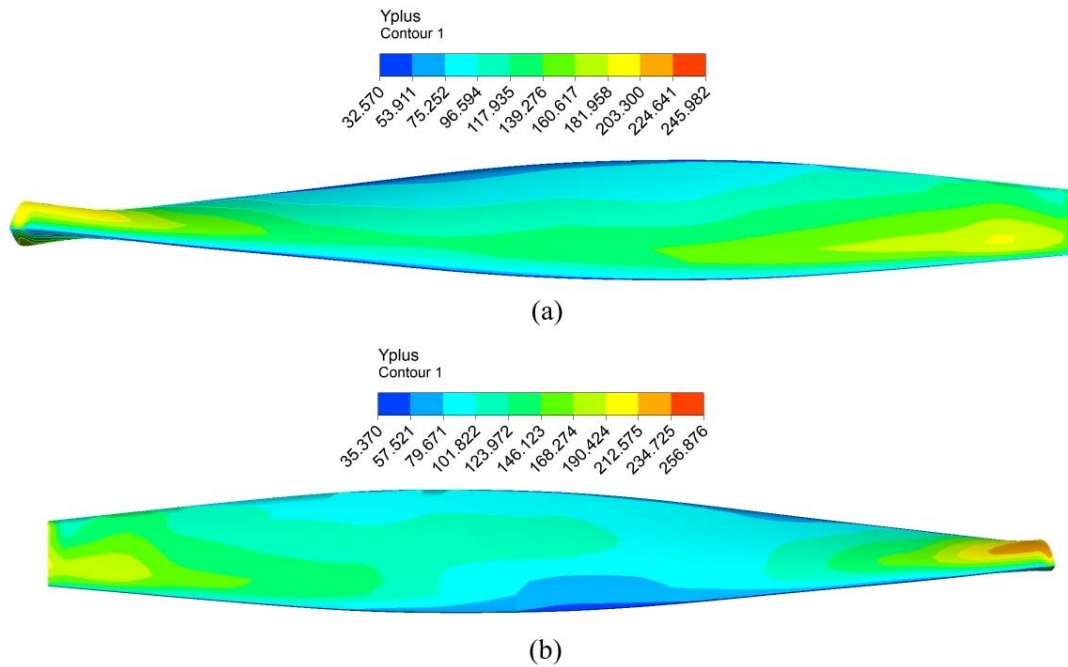


Figure 8.7. Contours of y^+ on blade surfaces (a) Front Propeller (b) Aft Propeller.

The distributions of pressure on the pressure and suction sides of the blades have been shown in Figure 8.8 and Figure 8.9.

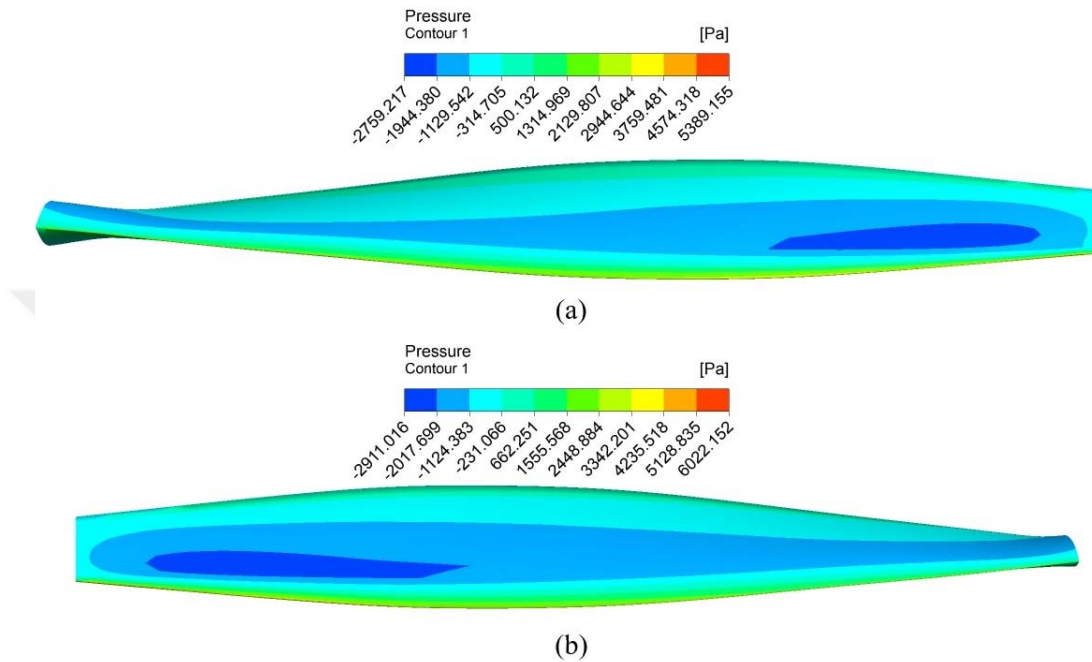


Figure 8.8. Pressure Contours on Pressure Side (a) Front Propeller (b) Aft Propeller.

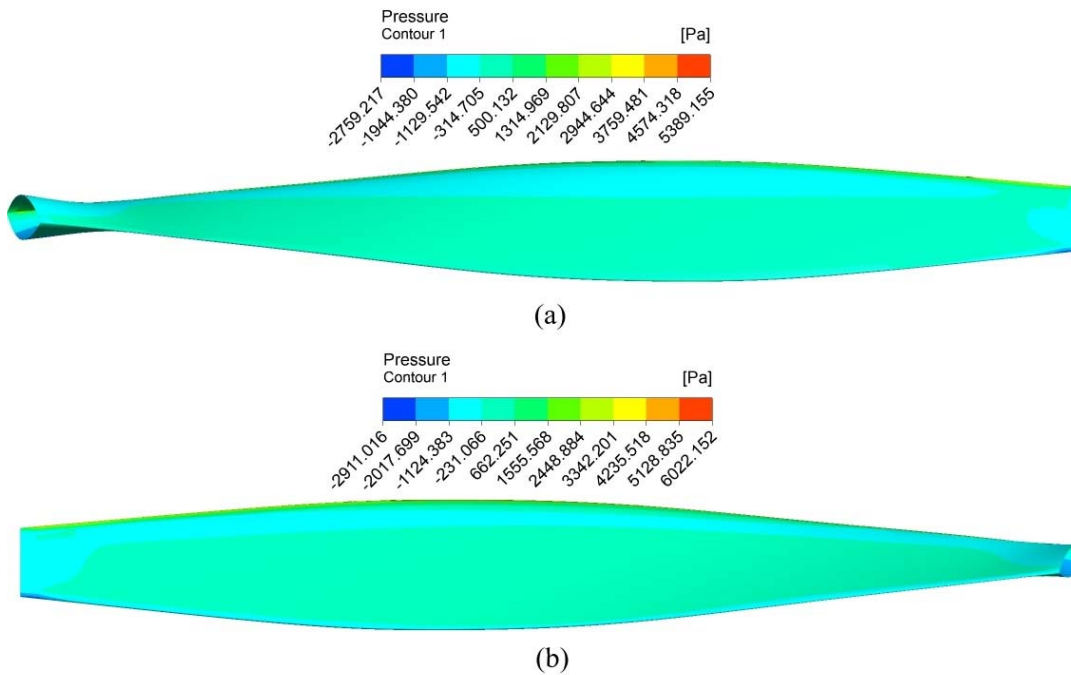


Figure 8.9. Pressure Contours on Suction Side (a) Front Propeller (b) Aft Propeller.

Section wise Mach Number contours of the blade have been shown in Figure 8.10. The maximum Mach Number attained is around 0.2.

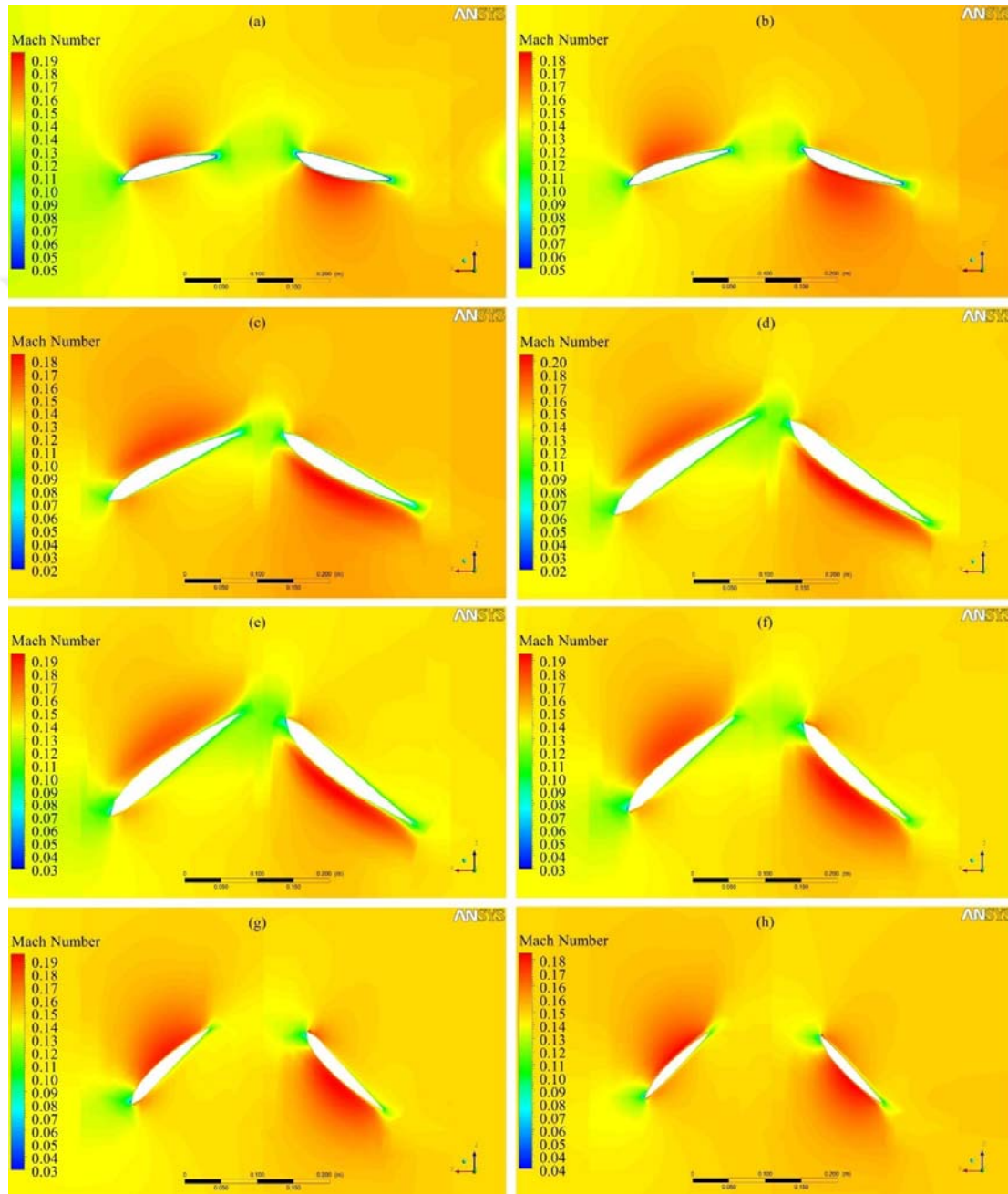


Figure 8.10. Mach Number Contours in Stationary Frame at various blade sections at $\psi = 72^\circ$ (a) $x=0.26$ (b) $x=0.3$ (c) $x=0.45$ (d) $x=0.6$ (e) $x=0.7$ (f) $x=0.8$ (g) $x=0.9$ (h) $x=0.95$.

9. CONCLUSION AND SUGGESTIONS

A detailed study was conducted into the design of contra-rotating propellers followed by calculations of performance of dual-rotating propellers using section data and full-model RANS steady and unsteady numerical computations. The main conclusions are presented as follows:

1. Several different numerical methods and techniques have been used and compared for the computation of dual-rotating propeller performance. Literature review has provided an insight into the aerodynamics and design of such a set of propellers. The CFD results are in agreement with the experimental and calculated results.
2. The accuracy of the CFD results may further be improved by closing the steady or unsteady RANS equations using other turbulence models such as the two-equation $k-\omega$ SST, a combination of standard $k-\omega$ model near the walls and $k-\epsilon$ the outer layer, or a four-equation $\gamma-Re_\theta$ turbulence model specially developed for transitional flows. It is highly recommended that such a comparative study may be carried out in the future using a finer mesh.
3. Iso-Contours of the vorticity magnitude characterize the development of vortices in the slip-stream flow-field. It is evident that there is a complex interaction between the front propeller wakes and the tip vortices of the aft propeller.
4. The mutual interactions between the two propellers results in unsteady periodic blade loading oscillations during one full rotation. A quantitative analysis of the effects of any design modifications to the blade on the load distributions is desirable.
5. Despite superior performance as compared with single propellers, the contra-rotating propeller system is a source of aerodynamic noise which must be mitigated. A detailed aero-acoustic analysis with comparison of experimental and calculated results is highly recommended in this regard.

REFERENCES

- Anonim, 2008, *Gannet: History in Photos | Fleet Air Arm Association of Australia*, <https://www.faaaa.asn.au/gannet-images-media/>, date accessed: 20.10.2020.
- ANSYS, 2006, Modeling of Turbulent Flows, In *Fluent User Guide* (p. 49).
- Asnaghi, A, Svennberg, U, Gustafsson, R, Bensow, R., 2019, Propeller Tip Vortex Cavitation Mitigation using Roughness, *International Conference on Computational Methods in Marine Engineering*, 383–392.
- Barton, I. E., 1998, Comparison of simple- and piso-type algorithms for transient flows, *International Journal for Numerical Methods in Fluids*, 26,4, 459–483.
- Biermann, D., & Gray, W. H., 1941, *Wind Tunnel Tests of Eight Blade Single and Dual Rotating Propellers in the Tractor Position* (Issue November 1941).
- Borst, H., 1973, *Summary of Propeller Design Procedures and Data: Vol. I* (Issue November 1973).
- Brocklehurst, A., & Barakos, G. N., 2013, A review of helicopter rotor blade tip shapes, *Progress in Aerospace Sciences*, 56, July, 35–74.
- Crigler, J., & Talkin, H., 1942, *Propeller Selection from Aerodynamic Considerations*.
- de Oliveira, L. F. Q., Cerón-Muñoz, H. D., & Catalano, F. M., 2012, Aerodynamic Analysis Of High Rotation And Low Reynolds Number Propeller, *48th AIAA/ASME/SAE/ASEE Joint Propulsion Conference and Exhibit 2012, July*.
- Hall, E. J., Delaney, R. A., & James L. Bettner, 1990, Investigation of Advanced Counterrotation Blade Configuration Concepts for High Speed Turboprop Systems Task 1 - Ducted Propfan Analysis, *NASA Contractor Report 185217*, 7, 1–155.
- Huo, C., Lv, P., & Sun, A., 2019, Computational study on the aerodynamics of a long-shrouded contra-rotating rotor in hover, *International Journal of Micro Air Vehicles*, 11,.
- Inukai, Y., 2011, Development of Contra-Rotating Propeller with Tip-Raked Fins, *Second International Symposium on Marine Propulsors, SMP'11, Hamburg, Germany, June*.
- Lock, C. N., 1941, Interference Velocity for a Close Pair of Contra-rotating Airscrews, *Aeronautical Research Council Reports And Memoranda*, 2084.
- Lock, C. N. H., & Yeatman, D., 1934, Tables for Use in an Improved Method of Airscrew Strip Theory Calculation, *Aeronautical Research Committee Reports and Memoranda*, No,1674-T3601.

REFERENCES (continued)

- Luan, H., Weng, L., Liu, R., Li, D., & Wang, M., 2019, Axial spacing effects on rotor-rotor interaction noise and vibration in a contra-rotating fan, *International Journal of Aerospace Engineering*.
- Marinus, B. G., 2012, Comparative study of the effects of sweep and humps on high-speed propeller blades, *18th AIAA/CEAS Aeroacoustics Conference (33rd AIAA Aeroacoustics Conference)*, January 2012.
- Naiman, I., 1944, *Method of Calculating Performance of Dual-Rotating Propellers from Airfoil Characteristics*.
- Nallasamy, M., & Groeneweg, J. F., 1991, Unsteady blade-surface pressures on a large-scale advanced propeller- prediction and data, *Journal of Propulsion and Power*, 7,6, 866–872.
- Pankhurst, R. C. ., Veasy, B. A., Greening, B. S. ., & Love, E. M., 1948, *Tests of Contra-rotating Propellers of 2 7/8 -ft . Diameter at Negative Pitch on a " Typhoon " Aircraft Model, 2218*, 16.
- Siddappaji, K., & Turner, M. G., 2015, Counter Rotating Propeller Design Using Blade Element Momentum Theory, *22nd Interational Symposium on Air Breathing Engines (ISABE)*, October, 1–13.
- Sinnige, T., Stokkermans, T. C. A., Ragni, D., Eitelberg, G., & Veldhuis, L. L. M., 2018, Aerodynamic and aeroacoustic performance of a propeller propulsion system with swirl-recovery vanes, *Journal of Propulsion and Power*, 34,6, 1376–1390.
- Stokkermans, T. C., Nootebos, S., & Veldhuis, L. L., 2019, June 17, *Analysis and Design of a Small-Scale Wingtip-Mounted Pusher Propeller*.
- Stuermer, A., & Yin, J., 2009, Low-speed aerodynamics and aeroacoustics of CROR propulsion systems, *15th AIAA/CEAS Aeroacoustics Conference (30th AIAA Aeroacoustics Conference)*.
- Vanderver, J. S., & Visser, K. D., 2000, Analysis of a Contra-Rotating Propeller Driven Transport Aircraft, *AIAA*, 13699–5725, 1–11.
- Villar, G. M., Lindblad, D., & Andersson, N., 2019, Effect of airfoil parametrization on the optimization of counter rotating open rotors, *AIAA Scitech 2019 Forum*.
- Wang, Y., Li, Q., Eitelberg, G., Veldhuis, L. L. M., & Kotsonis, M., 2014, Design and numerical investigation of swirl recovery vanes for the Fokker 29 propeller, *Chinese Journal of Aeronautics*, 27,5, 1128–1136.
- Weick, F. E., & Wood, D. H., 1929, *The Twenty-Foot Propeller Research Tunnel of the National Advisory Committee for Aeronautics*, Langley Memorial Aeronautical Lab.

APPENDIX-A

Table A.1. Sheet 1 for $r/R = 0.3$.

C_{L1}	0.2	0.3	0.4	0.5	0.6	0.7	0.8
α_1 (degrees)	4.422	6.644	8.867	11.089	13.311	15.533	17.756
ϕ_1 (degrees)	67.448	65.226	63.003	60.781	58.559	56.337	54.114
$\sin \phi_1$	0.924	0.908	0.891	0.873	0.853	0.832	0.81
$\cot \phi_1$	0.415	0.462	0.509	0.559	0.611	0.666	0.723
z	0.342	0.171	0	-0.171	-0.342	-0.513	-0.684
F_1	1.132	1.116	1.1	1.085	1.07	1.056	1.043
$\sigma / 4F_1$	0.047	0.047	0.048	0.049	0.049	0.05	0.051
$\tan \epsilon_1$	0.01	0.016	0.022	0.028	0.035	0.042	0.05
ϵ_1 (degrees)	0.579	0.896	1.235	1.599	1.989	2.41	2.864
$\cot \phi_1 + \tan \epsilon_1$	0.425	0.477	0.531	0.587	0.646	0.708	0.774
A	0.027	0.037	0.045	0.052	0.058	0.063	0.067
$1 + 2A$	1.054	1.073	1.089	1.103	1.115	1.126	1.135
$A \cot \phi_1$	0.011	0.017	0.023	0.029	0.035	0.042	0.049
$\tan(\phi_1 - \epsilon_1)$	2.341	2.081	1.863	1.676	1.515	1.373	1.246
G	2.232	1.954	1.731	1.546	1.39	1.257	1.141
C_{L2}	0.193	0.314	0.434	0.552	0.669	0.785	0.899
α_2 (degrees)	4.256	6.948	9.614	12.25	14.854	17.423	19.955
ϕ_2 (degrees)	66.314	63.622	60.956	58.32	55.716	53.147	50.615
$\sin \phi_2$	0.916	0.896	0.874	0.851	0.826	0.8	0.773
$\cot \phi_2$	0.439	0.496	0.555	0.617	0.682	0.75	0.821
z	0.255	0.048	-0.157	-0.36	-0.56	-0.758	-0.953
F_2	1.124	1.104	1.086	1.068	1.052	1.038	1.025
$\sigma / 4F_2$	0.047	0.048	0.049	0.049	0.05	0.051	0.052
$\tan \epsilon_2$	0.01	0.017	0.024	0.032	0.041	0.05	0.06
ϵ_2 (degrees)	0.566	0.96	1.383	1.838	2.33	2.86	3.431
$\cot \phi_1 + \tan \epsilon_1$	2.22	1.934	1.703	1.51	1.346	1.204	1.079
$\tan(\phi_2 - \epsilon_2)$	2.328	2.059	1.832	1.637	1.465	1.313	1.176
J	2.194	1.941	1.727	1.542	1.381	1.238	1.108

Table A.2. Sheet 2 for $r/R = 0.3$.

C_{L1}	0.2	0.3	0.4	0.5	0.6	0.7	0.8
$\theta_2 - \phi_2$ (degrees)	4.411	6.633	8.856	11.078	13.3	15.522	17.744
ϕ_2 (degrees)	66.159	63.937	61.714	59.492	57.27	55.048	52.826
$\sin \phi_2$	0.915	0.898	0.881	0.862	0.841	0.82	0.797
$\tan \phi_2$	2.263	2.045	1.858	1.697	1.556	1.431	1.319
z	0.243	0.072	-0.099	-0.27	-0.441	-0.612	-0.783
F_2	1.123	1.107	1.091	1.076	1.062	1.048	1.036
$\sigma / 4F_2$	0.047	0.048	0.048	0.049	0.05	0.05	0.051
$\tan \phi_2 - G$	0.031	0.09	0.128	0.151	0.166	0.174	0.178
$G \tan \phi_2 + 1 - F_2$	4.928	3.889	3.125	2.548	2.101	1.75	1.469
$\tan \epsilon_2$	0.006	0.023	0.041	0.059	0.079	0.099	0.121
C_{L2}	0.122	0.436	0.743	1.042	1.333	1.616	1.891
C_{L1}	0.2	0.3	0.4	0.5	0.6	0.7	0.8
$\theta_2 - \phi_2$ (degrees)	4.433	6.656	8.878	11.1	13.322	15.544	17.767
ϕ_2 (degrees)	66.137	63.914	61.692	59.47	57.248	55.026	52.803
$\sin \phi_2$	0.915	0.898	0.88	0.861	0.841	0.819	0.797
$\tan \phi_2$	2.261	2.043	1.857	1.696	1.555	1.43	1.318
z	0.241	0.07	-0.101	-0.272	-0.442	-0.613	-0.784
F_2	1.123	1.107	1.091	1.076	1.062	1.048	1.036
$\sigma / 4F_2$	0.047	0.048	0.048	0.049	0.05	0.05	0.051
$\tan \phi_2 - G$	0.028	0.088	0.126	0.15	0.164	0.173	0.177
$G \tan \phi_2 + 1 - F_2$	4.923	3.885	3.122	2.545	2.099	1.748	1.467
$\tan \epsilon_2$	0.006	0.023	0.04	0.059	0.078	0.099	0.12
C_{L2}	0.112	0.427	0.733	1.032	1.323	1.606	1.881

Table A.3. Sheet 3 for $r/R = 0.3$.

J	2.196	1.943	1.729	1.545	1.384	1.241	1.112
C_{L1}	0.2	0.3	0.4	0.5	0.6	0.7	0.8
$\tan \epsilon_1$	0.01	0.016	0.022	0.028	0.035	0.042	0.05
$\cot \phi_1$	0.415	0.462	0.509	0.559	0.611	0.666	0.723
α_1 (degrees)	4.422	6.644	8.867	11.089	13.311	15.533	17.756
z	0.096	0.601	1.106	1.611	2.116	2.621	3.126
L/D	3.984	6.004	8.024	10.044	12.065	14.085	16.105
$\tan \gamma_1$	0.251	0.167	0.125	0.1	0.083	0.071	0.062
$1 + \cot \phi_1 \tan \gamma_1$	1.104	1.077	1.063	1.056	1.051	1.047	1.045
F_1	1.132	1.116	1.1	1.085	1.07	1.056	1.043
$1/2\pi^3 x^4 F_1$	0.142	0.14	0.138	0.136	0.134	0.133	0.131
$(\cot \phi_1 + \tan \gamma_1)^2$	0.181	0.228	0.282	0.345	0.417	0.501	0.598
dC_{Q1}/dx	0.009	0.01	0.011	0.012	0.012	0.012	0.011
$\cot \phi_1 - \tan \gamma_1$	0.164	0.295	0.385	0.46	0.529	0.595	0.661
$\pi^3 x^3 F_1$	0.948	0.935	0.921	0.908	0.896	0.884	0.873
dC_{T1}/dx	0.009	0.019	0.027	0.034	0.039	0.044	0.048
C_{L2}	0.192	0.313	0.432	0.55	0.667	0.782	0.896
$\tan \epsilon_2$	0.01	0.017	0.024	0.032	0.041	0.05	0.06
$\cot \phi_2$	0.438	0.495	0.555	0.616	0.68	0.748	0.819
α_2 (degrees)	4.243	6.926	9.582	12.21	14.805	17.366	19.892
z	0.055	0.665	1.269	1.866	2.456	3.038	3.612
L/D	3.821	6.26	8.675	11.063	13.423	15.751	18.047
$\tan \gamma_2$	0.262	0.16	0.115	0.09	0.075	0.063	0.055
$1 + \cot \phi_2 \tan \gamma_2$	1.115	1.079	1.064	1.056	1.051	1.047	1.045
F_2	1.124	1.105	1.086	1.068	1.052	1.038	1.025
$1/2\pi^3 x^4 F_2$	0.141	0.139	0.136	0.134	0.132	0.13	0.129
$\cot \phi_2 + \tan \gamma_2$	0.448	0.512	0.579	0.648	0.721	0.798	0.879
$1 + 2A$	1.054	1.073	1.089	1.103	1.115	1.126	1.135
$(\cot \phi_2 + \tan \gamma_2)^2$	0.181	0.228	0.282	0.345	0.418	0.502	0.6
dC_{Q2}/dx	0.009	0.011	0.012	0.013	0.013	0.014	0.013
$\cot \phi_2 - \tan \gamma_2$	0.177	0.336	0.439	0.526	0.606	0.685	0.764
$\pi^3 x^3 F_2$	0.941	0.925	0.91	0.895	0.881	0.869	0.859
dC_{T2}/dx	0.009	0.023	0.034	0.044	0.052	0.059	0.065

Table A.4. Sheet 1 for $r/R = 0.45$.

C_{L1}	0.2	0.3	0.4	0.5	0.6	0.7	0.8
α_1 (degrees)	-1.196	-0.109	0.978	2.065	3.152	4.239	5.326
ϕ_1 (degrees)	63.901	62.814	61.727	60.64	59.553	58.466	57.379
$\sin \phi_1$	0.898	0.89	0.881	0.872	0.862	0.852	0.842
$\cot \phi_1$	0.49	0.514	0.538	0.563	0.588	0.614	0.64
z	0.908	0.818	0.727	0.637	0.546	0.455	0.365
F_1	0.922	0.923	0.923	0.924	0.924	0.925	0.926
$\sigma / 4F_1$	0.052	0.052	0.052	0.052	0.052	0.052	0.052
$\tan \epsilon_1$	0.012	0.018	0.024	0.03	0.036	0.043	0.049
ϵ_1 (degrees)	0.665	1.007	1.356	1.711	2.074	2.446	2.825
$\cot \phi_1 + \tan \epsilon_1$	0.501	0.531	0.562	0.592	0.624	0.656	0.689
A	0.021	0.031	0.039	0.047	0.054	0.06	0.066
$1 + 2A$	1.043	1.061	1.078	1.093	1.107	1.12	1.133
$A \cot \phi_1$	0.01	0.016	0.021	0.026	0.032	0.037	0.042
$\tan(\phi_1 - \epsilon_1)$	1.983	1.865	1.758	1.66	1.568	1.484	1.405
G	1.912	1.773	1.651	1.542	1.445	1.357	1.278
C_{L2}	0.176	0.31	0.443	0.575	0.706	0.836	0.964
α_2 (degrees)	-1.455	0.004	1.451	2.885	4.306	5.714	7.109
ϕ_2 (degrees)	62.86	61.401	59.954	58.52	57.099	55.691	54.296
$\sin \phi_2$	0.89	0.878	0.866	0.853	0.84	0.826	0.812
$\cot \phi_2$	0.513	0.545	0.578	0.612	0.647	0.682	0.719
z	0.822	0.7	0.58	0.46	0.342	0.224	0.108
F_2	0.923	0.923	0.924	0.925	0.926	0.927	0.929
$\sigma / 4F_2$	0.052	0.052	0.052	0.052	0.052	0.052	0.052
$\tan \epsilon_2$	0.01	0.018	0.027	0.035	0.044	0.052	0.061
ϵ_2 (degrees)	0.591	1.055	1.528	2.009	2.501	3.004	3.519
$\cot \phi_1 + \tan \epsilon_1$	1.902	1.756	1.627	1.511	1.407	1.312	1.225
$\tan(\phi_2 - \epsilon_2)$	1.973	1.848	1.733	1.626	1.526	1.433	1.345
J	2.789	2.613	2.45	2.299	2.158	2.026	1.902

Table A.5. Sheet 2 for $r/R = 0.45$.

C_{L1}	0.2	0.3	0.4	0.5	0.6	0.7	0.8
$\theta_2 - \phi_2$ (degrees)	-1.304	-0.217	0.87	1.957	3.043	4.13	5.217
ϕ_2 (degrees)	62.709	61.622	60.535	59.448	58.362	57.275	56.188
$\sin \phi_2$	0.889	0.88	0.871	0.861	0.851	0.841	0.831
$\tan \phi_2$	1.938	1.851	1.77	1.694	1.623	1.556	1.493
z	0.809	0.719	0.628	0.537	0.447	0.356	0.266
F_2	0.923	0.923	0.924	0.924	0.925	0.926	0.927
$\sigma / 4F_2$	0.052	0.052	0.052	0.052	0.052	0.052	0.052
$\tan \phi_2 - G$	0.027	0.078	0.119	0.152	0.178	0.199	0.215
$G \tan \phi_2 + 1 - F_2$	3.782	3.359	2.998	2.688	2.42	2.186	1.981
$\tan \epsilon_2$	0.007	0.023	0.04	0.057	0.074	0.091	0.109
C_{L2}	0.121	0.394	0.665	0.936	1.205	1.473	1.74
C_{L1}	0.2	0.3	0.4	0.5	0.6	0.7	0.8
$\theta_2 - \phi_2$ (degrees)	-1.087	0	1.087	2.174	3.261	4.348	5.435
ϕ_2 (degrees)	62.492	61.405	60.318	59.231	58.144	57.057	55.97
$\sin \phi_2$	0.887	0.878	0.869	0.859	0.849	0.839	0.829
$\tan \phi_2$	1.92	1.835	1.754	1.68	1.609	1.543	1.481
z	0.791	0.7	0.61	0.519	0.429	0.338	0.248
F_2	0.923	0.923	0.924	0.924	0.925	0.926	0.927
$\sigma / 4F_2$	0.052	0.052	0.052	0.052	0.052	0.052	0.052
$\tan \phi_2 - G$	0.009	0.062	0.104	0.137	0.164	0.186	0.203
$G \tan \phi_2 + 1 - F_2$	3.748	3.329	2.972	2.666	2.4	2.169	1.965
$\tan \epsilon_2$	0.002	0.019	0.035	0.052	0.069	0.086	0.103
C_{L2}	0.04	0.312	0.582	0.851	1.119	1.386	1.65

Table A.6. Sheet 3 for $r/R = 0.45$.

J	2.789	2.613	2.45	2.299	2.158	2.026	1.902
C_{L1}	0.2	0.3	0.4	0.5	0.6	0.7	0.8
$\tan \epsilon_1$	0.012	0.018	0.024	0.03	0.036	0.043	0.049
$\cot \phi_1$	0.744	0.774	0.804	0.835	0.868	0.901	0.935
α_1 (degrees)	-1.196	-0.109	0.978	2.065	3.152	4.239	5.326
z	-0.88	-0.621	-0.362	-0.104	0.155	0.414	0.673
L/D	19.193	28.408	36.841	44.317	50.659	55.688	59.23
$\tan \gamma_1$	0.052	0.035	0.027	0.023	0.02	0.018	0.017
$1 + \cot \phi_1 \tan \gamma_1$	1.039	1.027	1.022	1.019	1.017	1.016	1.016
F_1	0.922	0.923	0.923	0.924	0.924	0.925	0.926
$1/2\pi^3 x^4 F_1$	0.587	0.587	0.587	0.587	0.588	0.588	0.589
$(\cot \phi_1 + \tan \gamma_1)^2$	0.571	0.626	0.685	0.749	0.817	0.89	0.97
dC_{Q1}/dx	0.012	0.017	0.021	0.024	0.027	0.029	0.03
$\cot \phi_1 - \tan \gamma_1$	0.692	0.739	0.777	0.813	0.848	0.883	0.919
$\pi^3 x^3 F_1$	2.607	2.608	2.609	2.61	2.612	2.614	2.616
dC_{T1}/dx	0.037	0.054	0.07	0.085	0.098	0.111	0.122
C_{L2}	0.176	0.31	0.443	0.575	0.706	0.836	0.964
$\tan \epsilon_2$	0.01	0.018	0.027	0.035	0.044	0.052	0.061
$\cot \phi_2$	0.513	0.545	0.578	0.612	0.647	0.682	0.719
α_2 (degrees)	-1.455	0.004	1.451	2.885	4.306	5.714	7.109
z	-0.942	-0.594	-0.25	0.092	0.43	0.765	1.097
L/D	16.902	29.32	40.218	49.213	55.951	60.1	61.353
$\tan \gamma_2$	0.059	0.034	0.025	0.02	0.018	0.017	0.016
$1 + \cot \phi_2 \tan \gamma_2$	1.03	1.019	1.014	1.012	1.012	1.011	1.012
F_2	0.923	0.923	0.924	0.925	0.926	0.927	0.929
$1/2\pi^3 x^4 F_2$	0.587	0.587	0.588	0.588	0.589	0.59	0.591
$\cot \phi_2 + \tan \gamma_2$	0.523	0.564	0.605	0.647	0.691	0.735	0.78
$1 + 2A$	1.043	1.061	1.078	1.093	1.107	1.12	1.133
$(\cot \phi_2 + \tan \gamma_2)^2$	0.252	0.282	0.315	0.351	0.389	0.43	0.475
dC_{Q2}/dx	0.025	0.039	0.05	0.06	0.067	0.073	0.077
$\cot \phi_2 - \tan \gamma_2$	0.453	0.511	0.554	0.592	0.629	0.666	0.702
$\pi^3 x^3 F_2$	2.608	2.609	2.611	2.614	2.617	2.621	2.625
dC_{T2}/dx	0.049	0.087	0.122	0.155	0.185	0.213	0.239

Table A.7. Sheet 1 for $r/R = 0.6$.

C_{L1}	0.2	0.3	0.4	0.5	0.6	0.7	0.8
α_1 (degrees)	-2.188	-1.146	-0.104	0.938	1.979	3.021	4.063
ϕ_1 (degrees)	57.733	56.691	55.649	54.608	53.566	52.524	51.483
$\sin \phi_1$	0.846	0.836	0.826	0.815	0.805	0.794	0.782
$\cot \phi_1$	0.631	0.657	0.683	0.71	0.738	0.767	0.796
z	0.288	0.178	0.068	-0.041	-0.151	-0.261	-0.37
F_1	0.738	0.742	0.747	0.752	0.757	0.762	0.767
$\sigma / 4F_1$	0.056	0.056	0.056	0.055	0.055	0.054	0.054
$\tan \epsilon_1$	0.013	0.02	0.027	0.034	0.041	0.048	0.055
ϵ_1 (degrees)	0.762	1.15	1.543	1.94	2.343	2.752	3.167
$\cot \phi_1 + \tan \epsilon_1$	0.645	0.677	0.71	0.744	0.779	0.815	0.851
A	0.015	0.022	0.028	0.034	0.04	0.045	0.05
$1 + 2A$	1.03	1.044	1.057	1.068	1.08	1.09	1.1
$A \cot \phi_1$	0.01	0.014	0.019	0.024	0.029	0.034	0.04
$\tan(\phi_1 - \epsilon_1)$	1.538	1.457	1.382	1.311	1.245	1.182	1.123
G	1.502	1.41	1.326	1.25	1.18	1.116	1.057
C_{L2}	0.162	0.29	0.417	0.543	0.668	0.793	0.916
α_2 (degrees)	-2.581	-1.248	0.074	1.388	2.691	3.985	5.268
ϕ_2 (degrees)	56.826	55.494	54.171	52.857	51.554	50.26	48.977
$\sin \phi_2$	0.837	0.824	0.811	0.797	0.783	0.769	0.754
$\cot \phi_2$	0.654	0.687	0.722	0.757	0.794	0.831	0.87
z	0.192	0.052	-0.087	-0.226	-0.363	-0.499	-0.634
F_2	0.742	0.748	0.754	0.76	0.767	0.774	0.781
$\sigma / 4F_2$	0.056	0.056	0.055	0.055	0.054	0.054	0.053
$\tan \epsilon_2$	0.011	0.02	0.028	0.037	0.046	0.055	0.065
ϵ_2 (degrees)	0.622	1.12	1.623	2.132	2.645	3.165	3.691
$\cot \phi_1 + \tan \epsilon_1$	1.494	1.395	1.305	1.223	1.147	1.076	1.01
$\tan(\phi_2 - \epsilon_2)$	1.53	1.442	1.36	1.282	1.208	1.138	1.071
J	2.884	2.719	2.564	2.417	2.278	2.146	2.019

Table A.8. Sheet 2 for $r/R = 0.6$.

C_{L1}	0.2	0.3	0.4	0.5	0.6	0.7	0.8
$\theta_2 - \phi_2$ (degrees)	-2.292	-1.25	-0.208	0.833	1.875	2.917	3.958
ϕ_2 (degrees)	56.537	55.495	54.453	53.412	52.37	51.328	50.287
$\sin \phi_2$	0.834	0.824	0.814	0.803	0.792	0.781	0.769
$\tan \phi_2$	1.513	1.455	1.4	1.347	1.297	1.249	1.204
z	0.162	0.052	-0.058	-0.167	-0.277	-0.386	-0.496
F_2	0.743	0.748	0.753	0.758	0.763	0.768	0.774
$\sigma / 4F_2$	0.056	0.056	0.055	0.055	0.054	0.054	0.054
$\tan \phi_2 - G$	0.011	0.045	0.074	0.097	0.117	0.133	0.147
$G \tan \phi_2 + 1 - F_2$	2.529	2.303	2.103	1.926	1.768	1.626	1.499
$\tan \epsilon_2$	0.004	0.02	0.035	0.05	0.066	0.082	0.098
C_{L2}	0.065	0.291	0.515	0.739	0.962	1.183	1.403
C_{L1}	0.2	0.3	0.4	0.5	0.6	0.7	0.8
$\theta_2 - \phi_2$ (degrees)	-2.083	-1.042	0	1.042	2.083	3.125	4.167
ϕ_2 (degrees)	56.328	55.287	54.245	53.203	52.162	51.12	50.078
$\sin \phi_2$	0.832	0.822	0.812	0.801	0.79	0.778	0.767
$\tan \phi_2$	1.501	1.443	1.389	1.337	1.287	1.24	1.195
z	0.14	0.03	-0.079	-0.189	-0.299	-0.408	-0.518
F_2	0.744	0.749	0.754	0.759	0.764	0.769	0.775
$\sigma / 4F_2$	0.056	0.055	0.055	0.055	0.054	0.054	0.054
$\tan \phi_2 - G$	-0.001	0.034	0.063	0.087	0.107	0.124	0.138
$G \tan \phi_2 + 1 - F_2$	2.51	2.286	2.088	1.912	1.756	1.615	1.488
$\tan \epsilon_2$	0	0.015	0.03	0.045	0.061	0.077	0.093
C_{L2}	-0.005	0.219	0.443	0.665	0.887	1.107	1.326

Table A.9. Sheet 3 for $r/R = 0.6$.

J	2.884	2.719	2.564	2.417	2.278	2.146	2.019
C_{L1}	0.2	0.3	0.4	0.5	0.6	0.7	0.8
$\tan \epsilon_1$	0.013	0.02	0.027	0.034	0.041	0.048	0.055
$\cot \phi_1$	0.631	0.657	0.683	0.71	0.738	0.767	0.796
α_1 (degrees)	-2.188	-1.146	-0.104	0.938	1.979	3.021	4.063
z	-0.651	-0.397	-0.142	0.112	0.366	0.62	0.874
L/D	30.064	43.182	54.531	63.804	70.844	75.645	78.35
$\tan \gamma_1$	0.033	0.023	0.018	0.016	0.014	0.013	0.013
$1 + \cot \phi_1 \tan \gamma_1$	1.021	1.015	1.013	1.011	1.01	1.01	1.01
F_1	0.738	0.742	0.747	0.752	0.757	0.762	0.767
$1/2\pi^3 x^4 F_1$	1.483	1.492	1.502	1.511	1.521	1.532	1.543
$(\cot \phi_1 + \tan \gamma_1)^2$	0.416	0.459	0.505	0.554	0.607	0.664	0.725
dC_{Q1}/dx	0.049	0.066	0.081	0.093	0.104	0.112	0.119
$\cot \phi_1 - \tan \gamma_1$	0.598	0.634	0.665	0.695	0.724	0.753	0.783
$\pi^3 x^3 F_1$	4.945	4.974	5.005	5.037	5.071	5.106	5.142
dC_{T1}/dx	0.095	0.138	0.178	0.214	0.248	0.279	0.307
C_{L2}	0.162	0.29	0.417	0.543	0.668	0.793	0.916
$\tan \epsilon_2$	0.011	0.02	0.028	0.037	0.046	0.055	0.065
$\cot \phi_2$	0.654	0.687	0.722	0.757	0.794	0.831	0.87
α_2 (degrees)	-2.581	-1.248	0.074	1.388	2.691	3.985	5.268
z	-0.747	-0.422	-0.099	0.221	0.539	0.855	1.168
L/D	24.742	41.962	56.274	67.124	74.362	78.215	79.258
$\tan \gamma_2$	0.04	0.024	0.018	0.015	0.013	0.013	0.013
$1 + \cot \phi_2 \tan \gamma_2$	1.026	1.016	1.013	1.011	1.011	1.011	1.011
F_2	0.742	0.748	0.754	0.76	0.767	0.774	0.781
$1/2\pi^3 x^4 F_2$	1.491	1.503	1.515	1.528	1.542	1.556	1.57
$\cot \phi_2 + \tan \gamma_2$	0.665	0.707	0.75	0.795	0.84	0.887	0.935
$1 + 2A$	1.03	1.044	1.057	1.068	1.08	1.09	1.1
$(\cot \phi_2 + \tan \gamma_2)^2$	0.416	0.459	0.504	0.553	0.606	0.662	0.722
dC_{Q2}/dx	0.04	0.065	0.086	0.104	0.119	0.131	0.142
$\cot \phi_2 - \tan \gamma_2$	0.613	0.664	0.704	0.743	0.78	0.819	0.857
$\pi^3 x^3 F_2$	4.97	5.01	5.051	5.094	5.139	5.186	5.235
dC_{T2}/dx	0.08	0.142	0.2	0.255	0.306	0.355	0.401

Table A.10. Sheet 1 for $r/R = 0.7$.

C_{L1}	0.2	0.3	0.4	0.5	0.6	0.7	0.8
α_1 (degrees)	-1.595	-0.523	0.548	1.62	2.692	3.764	4.836
ϕ_1 (degrees)	53.342	52.27	51.198	50.126	49.055	47.983	46.911
$\sin \phi_1$	0.802	0.791	0.779	0.767	0.755	0.743	0.73
$\cot \phi_1$	0.744	0.774	0.804	0.835	0.868	0.901	0.935
z	0.764	0.635	0.506	0.377	0.248	0.118	-0.011
F_1	0.62	0.626	0.632	0.639	0.646	0.653	0.661
$\sigma / 4F_1$	0.056	0.055	0.055	0.054	0.053	0.053	0.052
$\tan \epsilon_1$	0.014	0.021	0.028	0.035	0.042	0.05	0.057
ϵ_1 (degrees)	0.794	1.197	1.603	2.013	2.427	2.846	3.271
$\cot \phi_1 + \tan \epsilon_1$	0.758	0.795	0.832	0.87	0.91	0.951	0.993
A	0.011	0.016	0.021	0.026	0.03	0.034	0.038
$1 + 2A$	1.023	1.033	1.043	1.052	1.06	1.068	1.076
$A \cot \phi_1$	0.008	0.013	0.017	0.022	0.026	0.031	0.036
$\tan(\phi_1 - \epsilon_1)$	1.305	1.238	1.175	1.115	1.058	1.005	0.954
G	1.285	1.211	1.143	1.081	1.023	0.969	0.919
C_{L2}	0.151	0.272	0.393	0.512	0.631	0.749	0.866
α_2 (degrees)	-2.118	-0.821	0.469	1.749	3.021	4.284	5.538
ϕ_2 (degrees)	52.565	51.267	49.978	48.697	47.425	46.162	44.908
$\sin \phi_2$	0.794	0.78	0.766	0.751	0.736	0.721	0.706
$\cot \phi_2$	0.766	0.802	0.84	0.879	0.919	0.96	1.003
z	0.67	0.514	0.359	0.204	0.051	-0.101	-0.252
F_2	0.624	0.632	0.64	0.648	0.657	0.666	0.675
$\sigma / 4F_2$	0.055	0.055	0.054	0.053	0.052	0.052	0.051
$\tan \epsilon_2$	0.011	0.019	0.028	0.036	0.045	0.054	0.063
ϵ_2 (degrees)	0.602	1.091	1.582	2.075	2.573	3.074	3.58
$\cot \phi_1 + \tan \epsilon_1$	1.278	1.199	1.126	1.058	0.995	0.935	0.879
$\tan(\phi_2 - \epsilon_2)$	1.299	1.226	1.157	1.091	1.029	0.969	0.911
J	2.856	2.696	2.544	2.4	2.262	2.13	2.003

Table A.11. Sheet 2 for $r/R = 0.7$.

C_{L1}	0.2	0.3	0.4	0.5	0.6	0.7	0.8
$\theta_2 - \phi_2$ (degrees)	-1.608	-0.536	0.536	1.608	2.68	3.751	4.823
ϕ_2 (degrees)	52.054	50.983	49.911	48.839	47.767	46.695	45.623
$\sin \phi_2$	0.789	0.777	0.765	0.753	0.74	0.728	0.715
$\tan \phi_2$	1.282	1.234	1.188	1.144	1.102	1.061	1.022
z	0.609	0.48	0.351	0.222	0.092	-0.037	-0.166
F_2	0.627	0.634	0.64	0.647	0.655	0.662	0.67
$\sigma / 4F_2$	0.055	0.054	0.054	0.053	0.053	0.052	0.051
$\tan \phi_2 - G$	-0.002	0.023	0.045	0.063	0.079	0.092	0.103
$G \tan \phi_2 + 1 - F_2$	2.021	1.861	1.718	1.589	1.472	1.366	1.27
$\tan \epsilon_2$	-0.001	0.012	0.026	0.04	0.053	0.067	0.081
C_{L2}	-0.017	0.177	0.37	0.561	0.75	0.938	1.124
C_{L1}	0.2	0.3	0.4	0.5	0.6	0.7	0.8
$\theta_2 - \phi_2$ (degrees)	-1.501	-0.429	0.643	1.715	2.787	3.859	4.93
ϕ_2 (degrees)	51.947	50.875	49.804	48.732	47.66	46.588	45.516
$\sin \phi_2$	0.787	0.776	0.764	0.752	0.739	0.726	0.713
$\tan \phi_2$	1.278	1.229	1.183	1.14	1.097	1.057	1.018
z	0.596	0.467	0.338	0.209	0.08	-0.05	-0.179
F_2	0.628	0.634	0.641	0.648	0.655	0.663	0.671
$\sigma / 4F_2$	0.055	0.054	0.054	0.053	0.053	0.052	0.051
$\tan \phi_2 - G$	-0.007	0.018	0.04	0.059	0.074	0.088	0.099
$G \tan \phi_2 + 1 - F_2$	2.014	1.855	1.712	1.584	1.467	1.362	1.265
$\tan \epsilon_2$	-0.004	0.01	0.023	0.037	0.051	0.064	0.078
C_{L2}	-0.052	0.142	0.334	0.524	0.713	0.9	1.086

Table A.12. Sheet 3 for $r/R = 0.7$.

J	2.856	2.696	2.544	2.4	2.262	2.13	2.003
C_{L1}	0.2	0.3	0.4	0.5	0.6	0.7	0.8
$\tan \epsilon_1$	0.014	0.021	0.028	0.035	0.042	0.05	0.057
$\cot \phi_1$	0.744	0.774	0.804	0.835	0.868	0.901	0.935
α_1 (degrees)	-1.595	-0.523	0.548	1.62	2.692	3.764	4.836
z	-0.702	-0.377	-0.052	0.273	0.598	0.922	1.247
L/D	32.82	47.588	59.399	68.072	73.692	76.612	77.451
$\tan \gamma_1$	0.03	0.021	0.017	0.015	0.014	0.013	0.013
$1 + \cot \phi_1 \tan \gamma_1$	1.023	1.016	1.014	1.012	1.012	1.012	1.012
F_1	0.62	0.626	0.632	0.639	0.646	0.653	0.661
$1/2\pi^3 x^4 F_1$	2.308	2.33	2.354	2.379	2.405	2.432	2.46
$(\cot \phi_1 + \tan \gamma_1)^2$	0.575	0.631	0.692	0.758	0.828	0.904	0.985
dC_{Q1}/dx	0.057	0.078	0.096	0.112	0.125	0.135	0.144
$\cot \phi_1 - \tan \gamma_1$	0.714	0.753	0.787	0.821	0.854	0.888	0.923
$\pi^3 x^3 F_1$	6.593	6.658	6.726	6.798	6.872	6.949	7.029
dC_{T1}/dx	0.114	0.166	0.214	0.259	0.3	0.339	0.376
C_{L2}	0.151	0.272	0.393	0.512	0.631	0.749	0.866
$\tan \epsilon_2$	0.011	0.019	0.028	0.036	0.045	0.054	0.063
$\cot \phi_2$	0.766	0.802	0.84	0.879	0.919	0.96	1.003
α_2 (degrees)	-2.118	-0.821	0.469	1.749	3.021	4.284	5.538
z	-0.86	-0.467	-0.076	0.312	0.697	1.08	1.46
L/D	24.663	43.774	58.627	68.907	74.853	77.231	77.286
$\tan \gamma_2$	0.041	0.023	0.017	0.015	0.013	0.013	0.013
$1 + \cot \phi_2 \tan \gamma_2$	1.031	1.018	1.014	1.013	1.012	1.012	1.013
F_2	0.624	0.632	0.64	0.648	0.657	0.666	0.675
$1/2\pi^3 x^4 F_2$	2.324	2.353	2.383	2.414	2.446	2.48	2.515
$\cot \phi_2 + \tan \gamma_2$	0.776	0.821	0.867	0.915	0.964	1.014	1.066
$1 + 2A$	1.023	1.033	1.043	1.052	1.06	1.068	1.076
$(\cot \phi_2 + \tan \gamma_2)^2$	0.576	0.632	0.692	0.757	0.826	0.901	0.981
dC_{Q2}/dx	0.044	0.072	0.096	0.117	0.135	0.15	0.162
$\cot \phi_2 - \tan \gamma_2$	0.725	0.779	0.823	0.864	0.905	0.947	0.99
$\pi^3 x^3 F_2$	6.64	6.722	6.808	6.897	6.99	7.086	7.185
dC_{T2}/dx	0.088	0.158	0.223	0.285	0.344	0.4	0.454

Table A.13. Sheet 1 for $r/R = 0.8$.

C_{L1}	0.2	0.3	0.4	0.5	0.6	0.7	0.8
α_1 (degrees)	-1.277	-0.213	0.851	1.915	2.979	4.043	5.106
ϕ_1 (degrees)	49.77	48.706	47.642	46.578	45.515	44.451	43.387
$\sin \phi_1$	0.763	0.751	0.739	0.726	0.713	0.7	0.687
$\cot \phi_1$	0.846	0.878	0.912	0.946	0.982	1.019	1.058
z	0.454	0.326	0.198	0.07	-0.058	-0.187	-0.315
F_1	0.507	0.513	0.519	0.526	0.533	0.541	0.548
$\sigma / 4F_1$	0.051	0.051	0.05	0.049	0.049	0.048	0.048
$\tan \epsilon_1$	0.013	0.02	0.027	0.034	0.041	0.048	0.055
ϵ_1 (degrees)	0.772	1.161	1.555	1.951	2.352	2.757	3.167
$\cot \phi_1 + \tan \epsilon_1$	0.859	0.899	0.939	0.98	1.023	1.068	1.113
A	0.008	0.012	0.015	0.018	0.021	0.024	0.027
$1+2A$	1.016	1.023	1.03	1.037	1.043	1.049	1.054
$A \cot \phi_1$	0.007	0.01	0.014	0.017	0.021	0.025	0.029
$\tan(\phi_1 - \epsilon_1)$	1.15	1.093	1.039	0.987	0.938	0.891	0.846
G	1.139	1.078	1.022	0.969	0.919	0.873	0.829
C_{L2}	0.138	0.253	0.368	0.481	0.594	0.707	0.819
α_2 (degrees)	-1.937	-0.712	0.506	1.717	2.92	4.116	5.304
ϕ_2 (degrees)	49.13	47.905	46.687	45.477	44.273	43.078	41.89
$\sin \phi_2$	0.756	0.742	0.728	0.713	0.698	0.683	0.668
$\cot \phi_2$	0.865	0.903	0.943	0.983	1.026	1.069	1.115
z	0.377	0.23	0.083	-0.063	-0.208	-0.352	-0.495
F_2	0.51	0.518	0.525	0.533	0.542	0.55	0.559
$\sigma / 4F_2$	0.051	0.05	0.05	0.049	0.048	0.047	0.047
$\tan \epsilon_2$	0.009	0.017	0.025	0.033	0.041	0.049	0.057
ϵ_2 (degrees)	0.533	0.983	1.434	1.888	2.344	2.804	3.268
$\cot \phi_1 + \tan \epsilon_1$	1.134	1.069	1.009	0.952	0.898	0.847	0.799
$\tan(\phi_2 - \epsilon_2)$	1.145	1.084	1.025	0.969	0.916	0.864	0.814
J	2.879	2.724	2.577	2.436	2.301	2.171	2.045

Table A.14. Sheet 2 for $r/R = 0.8$.

C_{L1}	0.2	0.3	0.4	0.5	0.6	0.7	0.8
$\theta_2 - \phi_2$ (degrees)	-1.383	-0.319	0.745	1.809	2.872	3.936	5
ϕ_2 (degrees)	48.576	47.512	46.449	45.385	44.321	43.257	42.193
$\sin \phi_2$	0.75	0.737	0.725	0.712	0.699	0.685	0.672
$\tan \phi_2$	1.133	1.092	1.052	1.014	0.977	0.941	0.907
z	0.31	0.182	0.054	-0.074	-0.202	-0.33	-0.459
F_2	0.514	0.52	0.527	0.534	0.541	0.549	0.557
$\sigma / 4F_2$	0.051	0.05	0.049	0.049	0.048	0.047	0.047
$\tan \phi_2 - G$	-0.006	0.014	0.03	0.045	0.057	0.068	0.077
$G \tan \phi_2 + 1 - F_2$	1.777	1.657	1.548	1.448	1.357	1.272	1.195
$\tan \epsilon_2$	-0.003	0.008	0.019	0.031	0.042	0.053	0.065
C_{L2}	-0.047	0.121	0.286	0.45	0.611	0.771	0.928
C_{L1}	0.2	0.3	0.4	0.5	0.6	0.7	0.8
$\theta_2 - \phi_2$ (degrees)	-1.17	-0.106	0.957	2.021	3.085	4.149	5.213
ϕ_2 (degrees)	48.364	47.3	46.236	45.172	44.108	43.044	41.981
$\sin \phi_2$	0.747	0.735	0.722	0.709	0.696	0.683	0.669
$\tan \phi_2$	1.125	1.084	1.044	1.006	0.969	0.934	0.9
z	0.285	0.157	0.028	-0.1	-0.228	-0.356	-0.484
F_2	0.515	0.522	0.528	0.536	0.543	0.551	0.558
$\sigma / 4F_2$	0.051	0.05	0.049	0.049	0.048	0.047	0.047
$\tan \phi_2 - G$	-0.014	0.005	0.022	0.037	0.05	0.061	0.07
$G \tan \phi_2 + 1 - F_2$	1.766	1.647	1.538	1.439	1.348	1.265	1.188
$\tan \epsilon_2$	-0.008	0.003	0.015	0.026	0.037	0.048	0.059
C_{L2}	-0.118	0.049	0.213	0.376	0.536	0.695	0.851

Table A.15. Sheet 3 for $r/R = 0.8$.

J	2.879	2.724	2.577	2.436	2.301	2.171	2.045
C_{L1}	0.2	0.3	0.4	0.5	0.6	0.7	0.8
$\tan \epsilon_1$	0.013	0.02	0.027	0.034	0.041	0.048	0.055
$\cot \phi_1$	0.846	0.878	0.912	0.946	0.982	1.019	1.058
α_1 (degrees)	-1.277	-0.213	0.851	1.915	2.979	4.043	5.106
z	-0.723	-0.436	-0.148	0.139	0.427	0.714	1.002
L/D	33.756	48.782	60.382	68.492	73.213	74.808	73.706
$\tan \gamma_1$	0.03	0.02	0.017	0.015	0.014	0.013	0.014
$1 + \cot \phi_1 \tan \gamma_1$	1.025	1.018	1.015	1.014	1.013	1.014	1.014
F_1	0.507	0.513	0.519	0.526	0.533	0.541	0.548
$1/2\pi^3 x^4 F_1$	3.218	3.258	3.3	3.343	3.387	3.434	3.482
$(\cot \phi_1 + \tan \gamma_1)^2$	0.739	0.807	0.882	0.961	1.047	1.14	1.239
dC_{Q1}/dx	0.06	0.083	0.103	0.12	0.135	0.147	0.158
$\cot \phi_1 - \tan \gamma_1$	0.816	0.858	0.895	0.932	0.969	1.006	1.044
$\pi^3 x^3 F_1$	8.045	8.145	8.249	8.357	8.469	8.584	8.704
dC_{T1}/dx	0.12	0.175	0.227	0.276	0.322	0.365	0.406
C_{L2}	0.138	0.253	0.368	0.481	0.594	0.707	0.819
$\tan \epsilon_2$	0.009	0.017	0.025	0.033	0.041	0.049	0.057
$\cot \phi_2$	0.865	0.903	0.943	0.983	1.026	1.069	1.115
α_2 (degrees)	-1.937	-0.712	0.506	1.717	2.92	4.116	5.304
z	-0.902	-0.571	-0.242	0.086	0.411	0.734	1.055
L/D	22.806	42.15	57.002	67.243	73.037	74.813	73.251
$\tan \gamma_2$	0.044	0.024	0.018	0.015	0.014	0.013	0.014
$1 + \cot \phi_2 \tan \gamma_2$	1.038	1.021	1.017	1.015	1.014	1.014	1.015
F_2	0.51	0.518	0.525	0.533	0.542	0.55	0.559
$1/2\pi^3 x^4 F_2$	3.242	3.289	3.338	3.389	3.442	3.496	3.552
$\cot \phi_2 + \tan \gamma_2$	0.875	0.921	0.968	1.016	1.067	1.118	1.172
$1 + 2A$	1.016	1.023	1.03	1.037	1.043	1.049	1.054
$(\cot \phi_2 + \tan \gamma_2)^2$	0.741	0.81	0.883	0.962	1.046	1.137	1.235
dC_{Q2}/dx	0.042	0.071	0.096	0.118	0.137	0.153	0.167
$\cot \phi_2 - \tan \gamma_2$	0.821	0.88	0.925	0.969	1.012	1.056	1.101
$\pi^3 x^3 F_2$	8.105	8.223	8.346	8.473	8.604	8.74	8.88
dC_{T2}/dx	0.084	0.153	0.219	0.281	0.341	0.397	0.452

Table A.16. Sheet 1 for $r/R = 0.9$.

C_{L1}	0.2	0.3	0.4	0.5	0.6	0.7	0.8
α_1 (degrees)	-1.075	0	1.075	2.151	3.226	4.301	5.376
ϕ_1 (degrees)	46.973	45.898	44.823	43.747	42.672	41.597	40.522
$\sin \phi_1$	0.731	0.718	0.705	0.691	0.678	0.664	0.65
$\cot \phi_1$	0.933	0.969	1.006	1.045	1.085	1.126	1.17
z	0.106	-0.011	-0.128	-0.245	-0.362	-0.479	-0.595
F_1	0.355	0.361	0.366	0.372	0.378	0.384	0.39
$\sigma / 4F_1$	0.05	0.049	0.049	0.048	0.047	0.046	0.046
$\tan \epsilon_1$	0.014	0.021	0.028	0.035	0.042	0.049	0.056
ϵ_1 (degrees)	0.786	1.184	1.584	1.987	2.394	2.805	3.219
$\cot \phi_1 + \tan \epsilon_1$	0.947	0.99	1.034	1.079	1.127	1.175	1.226
A	0.005	0.008	0.01	0.012	0.014	0.016	0.018
$1 + 2A$	1.01	1.015	1.02	1.024	1.028	1.032	1.036
$A \cot \phi_1$	0.005	0.007	0.01	0.012	0.015	0.018	0.021
$\tan(\phi_1 - \epsilon_1)$	1.042	0.99	0.94	0.893	0.847	0.804	0.762
G	1.036	0.983	0.932	0.884	0.839	0.796	0.756
C_{L2}	0.128	0.238	0.347	0.456	0.564	0.671	0.778
α_2 (degrees)	-1.845	-0.666	0.506	1.673	2.835	3.991	5.141
ϕ_2 (degrees)	46.443	45.264	44.092	42.925	41.763	40.607	39.457
$\sin \phi_2$	0.725	0.71	0.696	0.681	0.666	0.651	0.636
$\cot \phi_2$	0.951	0.991	1.032	1.075	1.12	1.166	1.215
z	0.048	-0.08	-0.207	-0.334	-0.461	-0.586	-0.711
F_2	0.358	0.364	0.37	0.376	0.383	0.39	0.397
$\sigma / 4F_2$	0.05	0.049	0.048	0.047	0.047	0.046	0.045
$\tan \epsilon_2$	0.009	0.016	0.024	0.032	0.039	0.047	0.055
ϵ_2 (degrees)	0.506	0.941	1.378	1.817	2.257	2.701	3.147
$\cot \phi_1 + \tan \epsilon_1$	1.033	0.977	0.923	0.873	0.825	0.779	0.735
$\tan(\phi_2 - \epsilon_2)$	1.039	0.984	0.931	0.881	0.832	0.786	0.74
J	2.938	2.782	2.634	2.491	2.354	2.221	2.093

Table A.17. Sheet 2 for $r/R = 0.9$.

C_{L1}	0.2	0.3	0.4	0.5	0.6	0.7	0.8
$\theta_2 - \phi_2$ (degrees)	-1.183	-0.108	0.968	2.043	3.118	4.194	5.269
ϕ_2 (degrees)	45.781	44.706	43.63	42.555	41.48	40.404	39.329
$\sin \phi_2$	0.717	0.703	0.69	0.676	0.662	0.648	0.634
$\tan \phi_2$	1.028	0.99	0.953	0.918	0.884	0.851	0.819
z	-0.024	-0.141	-0.258	-0.374	-0.491	-0.608	-0.725
F_2	0.361	0.367	0.372	0.378	0.384	0.391	0.398
$\sigma / 4F_2$	0.049	0.049	0.048	0.047	0.046	0.046	0.045
$\tan \phi_2 - G$	-0.009	0.007	0.021	0.034	0.045	0.055	0.064
$G \tan \phi_2 + 1 - F_2$	1.704	1.606	1.516	1.434	1.357	1.287	1.221
$\tan \epsilon_2$	-0.005	0.004	0.014	0.024	0.033	0.043	0.052
C_{L2}	-0.075	0.065	0.203	0.339	0.473	0.606	0.737
C_{L1}	0.2	0.3	0.4	0.5	0.6	0.7	0.8
$\theta_2 - \phi_2$ (degrees)	-0.968	0.108	1.183	2.258	3.333	4.409	5.484
ϕ_2 (degrees)	45.566	44.49	43.415	42.34	41.265	40.189	39.114
$\sin \phi_2$	0.714	0.701	0.687	0.674	0.66	0.645	0.631
$\tan \phi_2$	1.02	0.982	0.946	0.911	0.877	0.845	0.813
z	-0.047	-0.164	-0.281	-0.398	-0.515	-0.632	-0.748
F_2	0.362	0.368	0.373	0.379	0.386	0.392	0.399
$\sigma / 4F_2$	0.049	0.048	0.048	0.047	0.046	0.045	0.045
$\tan \phi_2 - G$	-0.016	0	0.014	0.027	0.038	0.048	0.057
$G \tan \phi_2 + 1 - F_2$	1.695	1.598	1.508	1.426	1.351	1.28	1.215
$\tan \epsilon_2$	-0.01	0	0.009	0.019	0.028	0.038	0.047
C_{L2}	-0.141	-0.002	0.136	0.271	0.405	0.537	0.667

Table A.18. Sheet 3 for $r/R = 0.9$.

J	2.938	2.782	2.634	2.491	2.354	2.221	2.093
C_{L1}	0.2	0.3	0.4	0.5	0.6	0.7	0.8
$\tan \epsilon_1$	0.014	0.021	0.028	0.035	0.042	0.049	0.056
$\cot \phi_1$	0.933	0.969	1.006	1.045	1.085	1.126	1.17
α_1 (degrees)	-1.075	0	1.075	2.151	3.226	4.301	5.376
z	-0.764	-0.457	-0.15	0.157	0.465	0.772	1.079
L/D	34.161	49.126	60.673	68.624	73.144	74.74	74.258
$\tan \gamma_1$	0.029	0.02	0.016	0.015	0.014	0.013	0.013
$1 + \cot \phi_1 \tan \gamma_1$	1.027	1.02	1.017	1.015	1.015	1.015	1.016
F_1	0.355	0.361	0.366	0.372	0.378	0.384	0.39
$1/2\pi^3 x^4 F_1$	3.616	3.668	3.723	3.781	3.841	3.905	3.971
$(\cot \phi_1 + \tan \gamma_1)^2$	0.897	0.98	1.069	1.165	1.269	1.382	1.504
dC_{Q1}/dx	0.057	0.079	0.098	0.114	0.128	0.141	0.151
$\cot \phi_1 - \tan \gamma_1$	0.904	0.949	0.99	1.03	1.071	1.113	1.156
$\pi^3 x^3 F_1$	8.035	8.152	8.274	8.402	8.537	8.678	8.825
dC_{T1}/dx	0.111	0.163	0.212	0.258	0.301	0.342	0.382
C_{L2}	0.128	0.238	0.347	0.456	0.564	0.671	0.778
$\tan \epsilon_2$	0.009	0.016	0.024	0.032	0.039	0.047	0.055
$\cot \phi_2$	0.951	0.991	1.032	1.075	1.12	1.166	1.215
α_2 (degrees)	-1.845	-0.666	0.506	1.673	2.835	3.991	5.141
z	-0.984	-0.648	-0.313	0.021	0.353	0.683	1.012
L/D	21.633	40.228	55.006	65.537	71.874	74.536	74.486
$\tan \gamma_2$	0.046	0.025	0.018	0.015	0.014	0.013	0.013
$1 + \cot \phi_2 \tan \gamma_2$	1.044	1.025	1.019	1.016	1.016	1.016	1.016
F_2	0.358	0.364	0.37	0.376	0.383	0.39	0.397
$1/2\pi^3 x^4 F_2$	3.641	3.7	3.762	3.827	3.895	3.966	4.04
$\cot \phi_2 + \tan \gamma_2$	0.96	1.007	1.056	1.107	1.159	1.214	1.27
$1 + 2A$	1.01	1.015	1.02	1.024	1.028	1.032	1.036
$(\cot \phi_2 + \tan \gamma_2)^2$	0.902	0.985	1.073	1.169	1.272	1.383	1.503
dC_{Q2}/dx	0.037	0.063	0.086	0.106	0.123	0.137	0.15
$\cot \phi_2 - \tan \gamma_2$	0.905	0.966	1.014	1.06	1.106	1.153	1.202
$\pi^3 x^3 F_2$	8.092	8.223	8.361	8.505	8.655	8.813	8.978
dC_{T2}/dx	0.072	0.133	0.19	0.245	0.297	0.347	0.395

Table A.19. Sheet 1 for $r/R = 0.95$.

C_{L1}	0.2	0.3	0.4	0.5	0.6	0.7	0.8
α_1 (degrees)	-1.075	0	1.075	2.151	3.226	4.301	5.376
ϕ_1 (degrees)	45.835	44.76	43.685	42.609	41.534	40.459	39.384
$\sin \phi_1$	0.717	0.704	0.691	0.677	0.663	0.649	0.635
$\cot \phi_1$	0.971	1.008	1.047	1.087	1.129	1.173	1.218
z	0.184	0.076	-0.032	-0.139	-0.247	-0.354	-0.462
F_1	0.253	0.257	0.261	0.266	0.271	0.276	0.281
$\sigma / 4F_1$	0.054	0.053	0.052	0.051	0.051	0.05	0.049
$\tan \epsilon_1$	0.015	0.023	0.03	0.038	0.046	0.053	0.061
ϵ_1 (degrees)	0.864	1.299	1.736	2.175	2.617	3.06	3.507
$\cot \phi_1 + \tan \epsilon_1$	0.986	1.031	1.077	1.125	1.175	1.226	1.279
A	0.004	0.006	0.007	0.009	0.011	0.012	0.013
$1 + 2A$	1.008	1.011	1.015	1.018	1.021	1.024	1.027
$A \cot \phi_1$	0.004	0.006	0.008	0.01	0.012	0.014	0.016
$\tan(\phi_1 - \epsilon_1)$	0.999	0.948	0.899	0.852	0.807	0.765	0.723
G	0.995	0.943	0.893	0.847	0.802	0.76	0.72
C_{L2}	0.126	0.233	0.339	0.445	0.551	0.656	0.761
α_2 (degrees)	-1.872	-0.723	0.423	1.563	2.7	3.831	4.958
ϕ_2 (degrees)	45.332	44.183	43.037	41.897	40.76	39.629	38.502
$\sin \phi_2$	0.711	0.697	0.682	0.668	0.653	0.638	0.623
$\cot \phi_2$	0.988	1.029	1.071	1.115	1.16	1.208	1.257
z	0.133	0.018	-0.096	-0.21	-0.324	-0.437	-0.55
F_2	0.255	0.259	0.264	0.269	0.274	0.28	0.286
$\sigma / 4F_2$	0.054	0.053	0.052	0.051	0.05	0.049	0.048
$\tan \epsilon_2$	0.01	0.018	0.026	0.034	0.042	0.05	0.058
ϵ_2 (degrees)	0.545	1.01	1.475	1.941	2.408	2.876	3.345
$\cot \phi_1 + \tan \epsilon_1$	0.993	0.938	0.887	0.838	0.791	0.747	0.704
$\tan(\phi_2 - \epsilon_2)$	0.997	0.943	0.892	0.843	0.796	0.751	0.707
J	2.974	2.815	2.662	2.516	2.376	2.24	2.11

Table A.20. Sheet 2 for $r/R = 0.95$.

C_{L1}	0.2	0.3	0.4	0.5	0.6	0.7	0.8
$\theta_2 - \phi_2$ (degrees)	-1.183	-0.108	0.968	2.043	3.118	4.194	5.269
ϕ_2 (degrees)	44.643	43.568	42.492	41.417	40.342	39.266	38.191
$\sin \phi_2$	0.703	0.689	0.675	0.662	0.647	0.633	0.618
$\tan \phi_2$	0.988	0.951	0.916	0.882	0.849	0.818	0.787
z	0.064	-0.043	-0.151	-0.258	-0.366	-0.473	-0.581
F_2	0.257	0.262	0.266	0.271	0.277	0.282	0.288
$\sigma / 4F_2$	0.053	0.052	0.051	0.05	0.049	0.048	0.048
$\tan \phi_2 - G$	-0.007	0.008	0.023	0.035	0.047	0.057	0.066
$G \tan \phi_2 + 1 - F_2$	1.725	1.635	1.552	1.476	1.405	1.34	1.279
$\tan \epsilon_2$	-0.004	0.005	0.015	0.024	0.033	0.043	0.052
C_{L2}	-0.057	0.069	0.193	0.316	0.437	0.557	0.675
C_{L1}	0.2	0.3	0.4	0.5	0.6	0.7	0.8
$\theta_2 - \phi_2$ (degrees)	-0.968	0.108	1.183	2.258	3.333	4.409	5.484
ϕ_2 (degrees)	44.428	43.352	42.277	41.202	40.127	39.051	37.976
$\sin \phi_2$	0.7	0.686	0.673	0.659	0.644	0.63	0.615
$\tan \phi_2$	0.98	0.944	0.909	0.875	0.843	0.811	0.781
z	0.043	-0.065	-0.172	-0.28	-0.387	-0.495	-0.602
F_2	0.258	0.263	0.267	0.272	0.278	0.283	0.289
$\sigma / 4F_2$	0.053	0.052	0.051	0.05	0.049	0.048	0.047
$\tan \phi_2 - G$	-0.015	0.001	0.016	0.029	0.04	0.051	0.06
$G \tan \phi_2 + 1 - F_2$	1.717	1.627	1.545	1.469	1.399	1.334	1.273
$\tan \epsilon_2$	-0.009	0.001	0.01	0.02	0.029	0.038	0.047
C_{L2}	-0.114	0.011	0.135	0.258	0.379	0.498	0.616

Table A.21. Sheet 3 for $r/R = 0.95$.

J	2.974	2.815	2.662	2.516	2.376	2.24	2.11
C_{L1}	0.2	0.3	0.4	0.5	0.6	0.7	0.8
$\tan \epsilon_1$	0.015	0.023	0.03	0.038	0.046	0.053	0.061
$\cot \phi_1$	0.971	1.008	1.047	1.087	1.129	1.173	1.218
α_1 (degrees)	-1.075	0	1.075	2.151	3.226	4.301	5.376
z	-0.669	-0.378	-0.088	0.203	0.493	0.784	1.075
L/D	34.6	49.06	60.293	68.023	72.33	73.656	72.803
$\tan \gamma_1$	0.029	0.02	0.017	0.015	0.014	0.014	0.014
$1 + \cot \phi_1 \tan \gamma_1$	1.028	1.021	1.017	1.016	1.016	1.016	1.017
F_1	0.253	0.257	0.261	0.266	0.271	0.276	0.281
$1/2\pi^3 x^4 F_1$	3.194	3.246	3.301	3.359	3.421	3.486	3.554
$(\cot \phi_1 + \tan \gamma_1)^2$	0.973	1.063	1.161	1.266	1.38	1.503	1.637
dC_{Q1}/dx	0.051	0.071	0.088	0.102	0.115	0.126	0.135
$\cot \phi_1 - \tan \gamma_1$	0.942	0.988	1.03	1.072	1.115	1.159	1.204
$\pi^3 x^3 F_1$	6.724	6.833	6.949	7.072	7.202	7.339	7.483
dC_{T1}/dx	0.098	0.144	0.187	0.228	0.266	0.303	0.337
C_{L2}	0.126	0.233	0.339	0.445	0.551	0.656	0.761
$\tan \epsilon_2$	0.01	0.018	0.026	0.034	0.042	0.05	0.058
$\cot \phi_2$	0.988	1.029	1.071	1.115	1.16	1.208	1.257
α_2 (degrees)	-1.872	-0.723	0.423	1.563	2.7	3.831	4.958
z	-0.884	-0.574	-0.264	0.044	0.351	0.657	0.962
L/D	22.167	39.667	53.883	64.24	70.631	73.401	73.327
$\tan \gamma_2$	0.045	0.025	0.019	0.016	0.014	0.014	0.014
$1 + \cot \phi_2 \tan \gamma_2$	1.045	1.026	1.02	1.017	1.016	1.016	1.017
F_2	0.255	0.259	0.264	0.269	0.274	0.28	0.286
$1/2\pi^3 x^4 F_2$	3.218	3.275	3.336	3.4	3.467	3.539	3.614
$\cot \phi_2 + \tan \gamma_2$	0.998	1.047	1.097	1.149	1.202	1.258	1.316
$1 + 2A$	1.008	1.011	1.015	1.018	1.021	1.024	1.027
$(\cot \phi_2 + \tan \gamma_2)^2$	0.981	1.071	1.168	1.273	1.386	1.509	1.641
dC_{Q2}/dx	0.033	0.055	0.075	0.092	0.107	0.12	0.131
$\cot \phi_2 - \tan \gamma_2$	0.943	1.004	1.052	1.099	1.146	1.194	1.243
$\pi^3 x^3 F_2$	6.774	6.895	7.022	7.157	7.299	7.45	7.607
dC_{T2}/dx	0.062	0.114	0.163	0.209	0.254	0.296	0.337